UNIVERSITÀ
POLITECNICA
DELLE MARCHE

Facoltà di Ingegneria
Ph.D Course in Information Engineering

Aging modeling and analysis of electrical storage in e-mobility and smart grid applications

Candidate:
Enrico Marchegiani

Advisor:
Prof. Andrea Monteriù

Coadvisor:
Ing. Lucio Ciabattoni
Ing. Francesco Ferracuti

Academic Year 2018-2021

UNIVERSITÀ
POLITECNICA
DELLE MARCHE

Facoltà di Ingegneria
Ph.D Course in Information Engineering

Aging modeling and analysis of electrical storage in e-mobility and smart grid applications

Candidate:
Enrico Marchegiani

Advisor:
Prof. Andrea Monteriù

Coadvisor:
Ing. Lucio Ciabattoni
Ing. Francesco Ferracuti

Academic Year 2018-2021

Università Politecnica delle Marche
Facoltà di Ingegneria
Ph.D Course in Information Engineering
Via Brecce Bianche – 60131 Ancona (AN), Italy

A tutte le persone donate sulla Strada.
Alla vita, mai scontata.
A Nonno, Steve e Valeria.

Abstract

Nowadays future energy perspectives are extensively discussed worldwide to address climate crisis and reach a significant decarbonisation. A new green energy economy is rapidly emerging and electrical energy even more holds fundamental role in this context. In order to face climate change, economical issues and encourage green transitions policies, investing in energy system transformation represents one solution in the path to climate neutrality and social equity. Therefore, the inclusion of renewables in future energy scenarios will lead to an increasing integration in national grids of Battery Energy Storage System (BESS), due to their flexibility and regulation capacity, solving the problem of renewable energy intermittency. Thus, an extensive study regarding lithium ions BESS analysis, aging modeling and their application in innovative scenario is conducted in this thesis in order to improve aging dynamics modeling, develop methodologies for state of health estimation and improve control and management of BESS operating conditions and assist energy planning strategies involving batteries. Firstly, a sensitivity analysis is conducted to evaluate robustness of parametric aging models and an automatic algorithm based on data-driven techniques is developed for online SOH estimation without a prior knowledge of BESS usage modality. Then, a least-square support vector machine (LS-SVM) model is investigated and compared to several models presented in literature for future torque demand prediction in order to improve electric vehicles (EVs) efficiency and consequently reduce effect of aging dynamics. An optimised State of Health (SOH) management and reduced degradation are results of an improved EVs management systems. As last, a simulation software is developed to facilitate BESS integration in vehicle-to-grid V2G scenario and to assist energy planning management in demand side flexibility (DSF) scenario. The simulator allows to define EVs district and obtain usage profiles of the whole EV fleet. Moreover, simulator consider aging dynamics on entire EVs district.

Sommario

Le prospettive future nel settore energetico sono al centro di un dibattito internazione che cerca di risolvere la crisi legata al cambiamento climatico arrivando ad un significativo processo di decarbonizzazione. Una nuova "green economy" sta emergendo rapidamente e l'energia elettrica sempre più detiene un ruolo centrale in questo contesto. Al fine di affrontare il cambiamento climatico, i problemi economici e favorire la transizione verde, gli investimenti nella trasformazione del sistema energetico rappresentano l'unica soluzione sulla strada verso la neutralità climatica e l'equità energetica. Quindi, l'inclusione delle fonti rinnovabili all'interno di futuri scenari energetici porterà all'integrazione nelle reti elettriche nazionali di sistemi di accumulo energetici a batteria (battery energy storage system BESS) grazie alla loro capacità di regolazione e flessibilità, costituendo una soluzione al problema dell'intermittenza delle fonti rinnovabili. Quindi un'analisi dettagliata di BESS agli ioni di litio, comprendente la relativa modellazione delle dinamiche di invecchiamento e la loro possibile applicazione in scenari innovativi, è stata condotta in questa tesi con lo scopo di migliorare l'attuale conoscenza e modellazione delle dinamiche di invecchiamento, sviluppare metodologie per la stima dello stato di salute e migliorare la gestione e il controllo delle condizioni operative delle batterie e assistere strategie di pianificazione energetica che includano i BESS. In primo luogo, un'analisi di sensitività è stata condotta al fine di valutare la robustezza dei modelli parametrici di invecchiamento proposti in letteratura ed è stato sviluppato un algoritmo automatico basato su dati per la stima online dello stato di salute dei BESS senza una conoscenza a priori delle modalità di funzionamento. Un altro contributo legato all'invecchiamento dei veicoli elettrici (EVs) è stato lo sviluppo di un modello least-square support vector machine (LS-SVM) per la predizione della coppia richiesta dal guidatore e il confronto con altre tecniche proposte in letteratura. Una predizione più accurata della coppia richiesta dal guidatore consente infatti di ottimizzare il sistema di gestione energetica del veicolo riducendo la degradazione della batteria. Infine, un simulatore è stato sviluppato per favorire l'integrazione dei BESS in scenari vehicle-to-grid (V2G) per la gestione della flessibilità energetica del carico nelle reti di distribuzione elettrica. Il simulatore permette di definire una flotta di veicoli elettrici e di caratterizzarne i profili di utilizzo e il loro invecchiamento.

Contents

List of Figures

List of Tables

Chapter 1

Introduction

Nowadays, due to the recent soaring in energy prices worldwide [1] and due to climate change, which could be the future energy perspectives and feasible innovative scenarios are the focal points of one of the most discussed threads among the entire world. The climate crisis and the ongoing increase of climate change pace have oriented worldwide research labs and companies to investigate technologies in order to reach substantial decarbonisation and the consequent reduction of emissions. A new energy economy is indeed rapidly emerging, mainly driven by policy action and technology innovation. Furthermore, electricity even more plays a key role in consumers' lives and seems to guarantee to become the main energy source on which citizens will depend for all their daily needs: eating, mobility, lighting and achieving thermal comfort throughout the year. Thus, well-being and benefits of people's lives rely on its reliability and affordability. Moreover, energy problems have a social and economic impact on low and lower-middle-income households, particularly when energy prices increase, due for instance to the actual global demand for gas soaring and the consequent effect in power market, forcing family unit to fall behind on the payments of their utility bills [2, 3]. Therefore, without effective policies to prepare for and manage these fluctuations, the daily variation of demand could increase in pursuance of declared pledges to 270 gigawatts (GW) in the European Union (from 120 GW today) and over 170 GW in India (from 40 GW) by mid-century [4]. In order to face climate change, economical issues and encourage green transitions policies, investing in energy system transformation represents the only solution in the path to climate neutrality and social equity. One of the problem is that fossil fuel won't phase out energy market in next decades [5] because of the necessity to deal with actual energy needs. State policies should halt fossil fuel subsidies to allow investment of national budgets in innovative technologies and in dumping potential distribution effects of the transition, tackling the main technological barriers to this passage. In some regions, clean technologies have already increasingly become the principal solution for consumers due to both policy support and to their cost-effective choice: solar PV or wind actually constitute the cheapest available source of new electricity generation in power sector and among several end-uses technologies[4]. In many markets for example, because of total costs of ownership, the case of EVs is one of the most persuasive scenario. Thus, further public and private investments are crucial for energy system transition with regard particularly to storage and decentralised electricity production in order to improve resilience and to attenuate renewed electricity price increases. An acceleration is required for achieve both a socially fair transition to climate neutrality by 2050 and an insurance against the sort of price shocks, especially for states which hugely depends on energy import, such as the EU. Indeed, EU net energy import dependency reached 60.6 % in 2019 compared to 58.2% in 2018 and 56% in 2000; the highest level in the past 30 years that leads to 31 million people affected by energy poverty in EU. [6]. By a technological point of view, if nations seriously begin to place

policies in the way for net zero emission for 2050, wind turbines, solar panels, lithium-ion batteries, electrolysers and fuel cells market will grow tenfold to USD 1.2 trillion by 2050 [4]. In EU, member states have already phased out coal achieving for 2020, along with pandemic condition, to a reduction of EU greenhouse gas emissions (including international aviation) down to 31 % compared to 1990. Renewable energy resources indeed overcame fossil fuels as main power source positioning at 38 % of EU electricity vs the fossil fuels at 37 % and nuclear at 25 % [6].

1.1 Energy storage

Therefore, current integration of renewables in innovative energy scenarios and the resulting need of store energy is becoming increasingly critical and it will be the key point for the deployment of Renewables Energy Systems (RESs) worldwide in the upcoming years [7]. In particular, energy storages will lead to an increase of connections between RESs and national grids, directly facing with the problem of the intermittent nature of renewables [8]. The supply uncertainty is a critical aspect and characterises the whole green energy scenario: for example wind blows neither continuously nor according to electricity demand and power generation from solar panel is widely affected by its sensitivity to weather conditions, air pollution and other factors influencing solar radiation intensity [9]. To overcome this, Energy Storage Systems (ESSs) are currently being applied since they can provide the possibility of decoupling energy generation and demand, besides contributing to the grid flexibility through the supply-demand balance [10]. ESSs are classified based on the form of stored energy, and their proper use is strictly dependent on the application: their technical characteristics such as energy capacity, charge/discharge dynamics, self-discharge rate, energy-power ratio, and life cycles have to be carefully considered for choosing the most suitable technology [11]. Considering the energy sector, namely stationary applications, the most common storage technology is the Battery Energy Storage System (BESS). Due to their higher flexibility and regulation capacity, BESSs are the most spread and mainly used in large-scale constructions [12]. Ramos et al. [13] presented both business models and regulatory challenges of the future energy storage implementation in the Finnish market context, focusing mainly on large-scale simulations. In particular, a great amount of small and medium sized BESSs, connected to a national grid with high level of renewables, led to several advantages: both self-sufficiency and self-consumption levels were increased, network losses were decreased, and the impact of renewable energy in the network was mitigated. Wan Abdullah et al. [14] investigated on the use and the benefits of using BESSs in the Malaysian electric network to determine their commercial and technical feasibility. Results showed a considerable reduction of the peak demand, a higher response to the electricity demand variability, and a better frequency regulation within the grid. Subsequently, these pros have fallen on the end-users' monthly bills since a consistent economic saving has been achieved, thus leading to a promising future of the implementation of BESSs in the Malaysian electric network itself to achieve the target of 20% renewable energy penetration by 2050. However, the future application of BESSs is not only focused on large-scale applications, but also in small-scale ones (e.g., residential building, offices, energy intensive industries, and Electric Vehicles (EVs) charging stations). Saini et al. [15] discussed on the application of small-scale BESSs in commercial, residential, and industrial sectors with different load profiles, highly variable during the day. BESSs are coupled with Photovoltaics (PV) to store renewable energy before being used by the end-users, or to be integrated with the local electric grid. To resemble the behaviour of a

PV-BESS system, a function that decides both time and capacity of charging and discharging of batteries has been developed to manage the PV penetration, and improve the voltage profile as well. In particular, the daily energy losses can be reduced and the reverse power flow in the distribution system can be properly handled without deviating the operational limits. Results showed that yearly energy losses decreased and, at the same time, BESSs allowed PV to be easily integrated into the electric grid since both over voltage and reverse power flow have been sensibly reduced. Mustafa et al. [16] focused the attention on the use of BESSs in the health sector in UK, mainly hospitals, so that the flexibility can be provided to the national electric grid. Four scenarios have been studied where PVs were coupled with BESSs. Results showed that an economic convenience has been found only if a group of hospitals operate together to provide a flexibility service to the electric grid, since PayBack Periods (PBPs) lower than 3 years and a Net Present Value (NPV) higher than £5 million have been achieved. Thus, BESS technological investigation and integration analysis are necessary to deal with the promising scenario that could be open. By a chemical point of view, Li-ion have replaced the previous batteries technologies in most of current application. They are characterised with respect to older solutions by an elevated energy density (as shown in Figure 1.1), no memory effect, low maintenance need, being cost-effective solution, supply and absorption of high amount of current, wide depth of charge/discharge, low self-discharge rate [17].

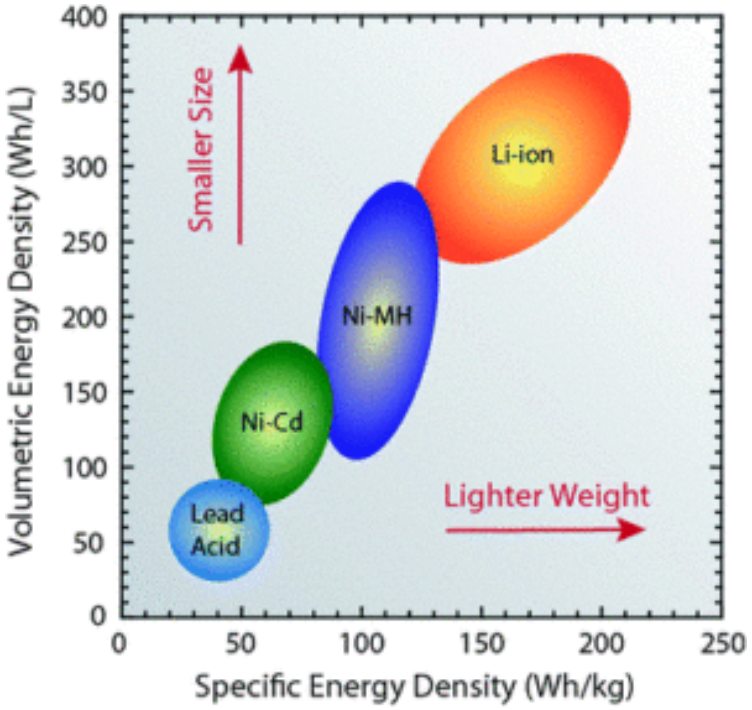

Figure 1.1: A diagram of the specific energy density and volumetric energy density of various battery types. Li-ion batteries represent the best solution over the other types of chemicals [17].

Thus, BESSs are mainly based on Li-ion, which operate with red-ox reactions occurring between the species that compose the battery's electrodes. Given the electro-chemical energy conversion pathway, BESSs are highly modular and for this reason they can be applied at different scales as previously discussed [18]. Moreover, Li-ion batteries present extremely

high round-trip efficiency (round-trip of $\geq 90\%$) compared to others types of ESSs [19], and fast charge/discharge dynamics as well [20]. Considering the versatility of BESSs, both energy planning and scheduling phases are crucial for their proper functioning in different applications, not only as a bulk energy storage, but also for price arbitrage, grid flexibility, load following, and frequency regulation [21]. Hence, an appropriate BESSs model, which describes their main technical characteristics and dynamics, must be used as input for their planning phase. Since energy scheduler have to decide the optimal solution among different technologies, the model's coherence and reliability, and also other systems considered in energy planning models, directly influences the results of the energy planning; therefore, a scenario-based validated BESSs model, able to assess different technological details at system level and to characterise most incisive parameters, is fundamental for energy planning phase. Scientific literature has focused in developing model to characterise battery dynamics. Chemical, thermal and electric models have been develop to simulate the dynamic of the batteries with the application for automotive context in [22, 23, 24, 25, 26]. Moreover, it is widely diffused in literature to model battery's electrical performance by means of circuital models. The main models used are:

- the 0^{th} order electrical model that is a simplified and widely adopted model by battery manufacturers using parameters as internal resistance (R_0), open-circuit voltage (V_{oc}), and voltage measured (V);
- the 1^{st} order electrical model that, in addition to the parameters already considered in the previous model, evaluates also polarization parameters (i.e. polarization capacity (C_p) and polarization resistance (R_p)).

First order model takes into account the battery's internal electrochemical phenomena, thus resulting in a more detailed simulation. However, the polarization parameters cannot be measured directly, but they must be estimated and thus a considerable availability of historical data is required; as a consequence, only few manufacturers can provide these estimations. Even though higher order models enable the assessment of more details, they also introduce more complexity, and thus they are barely applied due to the more efforts required. Circuital models are detailed in section 2.2.1. Another critical phenomena widely recognised in energy planning sector is that Li-ion batteries present relevant self-discharge phenomena that strongly limit their long-term storage capabilities, due to crossover reactions and material degradation [27].

Petkov et al. [28] studied the deployment of Power-to-Hydrogen (PtH_2) as a solution for long-term energy storage by taking into account several aspects such as the energy storage technologies, their size, and CO_2 emissions avoided. To perform this study, besides the hydrogen storage, also the Thermal Energy Storage (TES) and Li-ion batteries have been considered: from the literature, the self-discharge rate of the Li-ion battery technology was the lowest (0.00054 $hr^{-}1$) compared to the TES one (0.075 $hr^{-}1$). Bartolini et al. [18] adopted a self-discharge parameter of 0.1% in terms of the storage capacity per each day to assess the role of the BESS in a Local Energy Community (LEC). In another study, Zimmerman [29] measured the discharge capacity of BESSs, concluding that it can vary within the range of $2 - 7\%$ throughout a month depending on the voltage of the battery. More importantly, a central factor that characterises planning and usage of BESSs is the aging aspect, that consists in the reduction of the overall storable energy is definitely one of the main key aspects to be assessed since it affects both charging/discharging behaviours of a battery and its state of health (SOH) as well. Several approaches have been studied

by a microscopic point of view far to analyse the battery's degradation due to the aging phenomena, namely X-ray techniques, the Scanning Electron Microscopy (SEM), and the Electrochemical Impedance Spectroscopy (EIS) [30]. For real application, building models relying on battery characteristics obtained by these techniques do not represent a viable solution because the retrieval of that kind of data is challenging in a real time and large scale application by technological point of view; with some extent, scientific literature is studying how to implement EIS procedure to characterise battery impendance and other important parameters. Conventional EIS measurements include of sinusoidal perturbation in either potentiostatic or galvanostatic modes, make them unfeasible for real application. Furthermore, they rely on an accurate measurement over a wide frequency range, often not feasible for commercial scope due to problem related to data acquisition, storage and technical requirements on equipment required for the acquisition. As last, the overall procedure requires more investigation and interpretation to be used in real application purpose because of its early stage of development in the research field [31]. Other studies specifically addressed the aging aspect: among them, Eduardo et al. [32] analysed the discharge behaviour through experimental tests, showing that the loss was about 3% of the initial stored energy throughout a month of operation. The aging phenomena becomes even more important since Li-ion batteries could be considered for second life purposes, for example when a battery involved in automotive context has reached its end of life and, instead of being dismissed, can be employed with a new startup by utilities/power sector [33]. In transportation context indeed the battery end-life it is usually defined when its final capacity is almost the 20% of the original one [34], when electric vehicle autonomy is not adequately guaranteed anymore; therefore, modeling, identifying the causes and predicting degradation is highly relevant as well as developing techniques those aims to reduce degradation rate to the lowest level.

1.2 Electric vehicles

The automotive field has been heavily involved in electrification, with a resulting deep investigation and development of methodologies to improve energy efficiency, powered also by the massive production of Hybrid Electric Vehicles (HEVs) and pure Electric Vehicles (EVs) in last decades. These cars are featured by higher efficiency and energy economy with respect to Internal Combustion Engine (ICE) vehicles, achieved by recent advances in Energy Management Systems (EMSs) [35], accounting for a promising solution in transportation future perspective.

Modern EMSs are designed according to optimization-based techniques, aimed to manage the vehicle power flow according to an optimal approach driving the powertrain to operate in the best operating point of its characteristics. Common optimization-based EMSs are developed according to Pontryagin's Minimum Principle (PMP), Equivalent Consumption Minimization Strategy (ECMS), and its Adaptive version termed A-ECMS [36]. Furthermore, model-based techniques have been recently studied and applied to both hybrid and electric vehicles. In particular, Model Predictive Control (MPC) paradigm [37] have been recently considered, due to its capability to evaluate the H/EV performance over a certain future horizon [38, 39] and directly taking into account physical and logical constraints featuring the controlled plant [40, 41]. Mentioned EMSs are driven by the driver action, that is mapped on the demanded torque control, and the use of predicted driver control signal is considered a standard approach aimed to increase H/EV performances. Driving cycles pattern, vehicle velocity and torque demand have been considered as the main factors to be studied and

analyzed to optimize of H/EV powertrains with the resulting reduction of SOH degradation. Thus, development of model to predict these quantities is crucial for an increasing integration of these technologies in energy planning scenario. Driving cycle patterns contain aggregated information about next route characteristics, such as average speed and acceleration, time at rest, distance covered and so on. Vehicle velocity and torque demand reflect more directly and real-time driver's will and driving style, enabling a more accurate control action by EMSs.

1.3 Vehicle-to-grid

Nowadays a great part of power demand is still inflexible, causing a higher cost to the overall system. Power supply system has in fact to be ever more flexible to afford an increase of several and variable renewable energy production and to manage such load demand. Several techniques have been investigated in literature to face with these issues those constitute the most important barrier to green transition.

An increased flexibility level can be achieved for example by sector coupling, in the form of electrification of the mobility (electric vehicles) and the heating sectors (power to heat), or via smart appliances. The integration of electric vehicles in the electricity grid can provide flexibility due to the daily cycles of charging of their batteries. Another viable technique is the coupling of the heating and electricity sectors, which can provide flexible short-term demand by using heat pumps, heat storage and electric cooling loads. Finally, demand-side flexibility (DSF) can be obtained through aggregated residential demand-side management in smart homes [42]. Thus, harnessing of implicit and explicit demand side flexibility approaches represent a feasible solution to achieve this and to adjust (i.e. reduce, increase or shift) the electricity demand [43]. In this context BESSs hold a fundamental role and their analysis is crucial in order to guarantee an optimal use and efficiency.

As mentioned, Electric Vehicles (EVs) are characterised by an ongoing growth in the market due to their potential and innovative impact into electricity grid for new application as reported in recent forecasts of their penetration rate [44]. Vehicle-to-grid (V2G) scenario is one of the most promising technologies that may lead to a significant advancement on power system management operation [45]. EVs batteries could be used to exchange energy between the vehicles and the grid when cars are parked in a charging station and that energy isn't required by driver's route to home or work, thus creating an economic benefit for both owner and grid [46]. Moreover, the EV is no longer only a means of transportation, rather it becomes an important tool to communicate with power grid to deliver electricity into it and simultaneously control charging rate for EVs, becoming *de facto* a mobile battery electrical energy system [47]. Several services can be offered to the grid itself, such as power grid regulation, spinning reserves, peak load shaving, load leveling and reactive power compensation.

The V2G innovation will thus open up a new business scenario, namely the energy exchange manager between the power utilities and the EV drivers [48]. The V2G operation can indeed lead to two important applications. Firstly, since main issue related to renewable power generation is the natural intermittence, the use of standby generators to store this variable and unpredictable power production is expensive and inefficient while V2G operations can solve this issue [49]. Secondly, in a DSF scenario, a V2G approach allows to use the EV batteries to absorb (or buy) electrical energy from the grid during the off-peak period (load levelling), or generate (or sell) electrical energy to the grid during peak period (load shaving)

[50]. Moreover, batteries charging and discharging processes are performed more rapidly than the shutoff and startup processes of standby generators, which usually requires to respond to a black-start activation procedure and the required energisation of transformers.

An individual vehicle operating in a V2G scenario (also known as Vehicle-to-Building or V2B when dealing with home charging stations) can afford a small amount of kWh trade [51] due to its relatively limited maximum capacity, thus it may represent an inconvenient and ineffective solution in most cases. Therefore, an aggregation procedure [52] can be introduced to combine and properly control a number of EVs to ensure a smart charging and discharging management.

In the actual context, V2G has to deal with different challenges, in terms of normative regulation as well as from a technological point of view. V2G techniques indeed increase the number of charging/discharging cycles of EVs, affecting batteries SOH and remaining useful life (RUL), they require the knowledge of drivers' route and parking patterns, they strongly depend on the actual and forecasted EVs market penetration, on the geographical area, the availability of charging stations and so on. Although several possible scenarios emerge from these complex variables, engineers and grid operators have to deal with these issues without an availability of any large scale datasets. Thus, development of tools that could assist energy planning operation and allow to deploy and test energy management strategies is necessary to deal with such a complex, but equally promising and innovative, scenario.

1.4 Thesis aims and objectives

As widely discussed, BESS technological development and employment will characterise future innovative scenarios due to the important role that storage systems can hold in such energy context. This transition, over than requiring solution to assist and improve energy planning, present several technological issues those have to be tackled. Thus, an extensive study regarding BESS aging analysis and BESS application is conducted in this thesis. A particular attention is devoted to aging problem and its effects with the purpose of promoting green transition, improving the understanding of degradation dynamics, optimising BESS usage and implementation.

Focus of chapter 2 is centred on aging that is introduced and addressed. Several methodologies presented in scientific literature for SOH estimation are revised, comprising both data-driven and model-based techniques. Then, two main contributions are reported specifically regarding aging investigation. Firstly, a sensitivity analysis is conducted on real data to evaluate robustness of parametric aging models presented in literature. This study aims to analyse models proposed to assess their response to different input from which they are trained on, evaluating thereby its capability to deal with unexpected variation of input variables as usually occurs in real scenario; this measures also its feasibility and adaptability to be used in real application, leading to which model select based on requirements of specific case. Secondly, an algorithm for online SOH estimation is studied and developed. it is an automatic approach based on a data-driven model fusion approach and aims to evaluate aging progress on BESS without a prior knowledge as concerns storage operating modality, i.e. power or energy intensive.

In chapter 3 SOH degradation in EVs is addressed, analysing and comparing different methodologies for future torque demand prediction because it directly affects vehicle efficiency and economy. Performance of Energy Management Systems (EMSs) are strictly related to EV battery usage intensity, resulting in a more pronounced effect on battery aging. Accordingly,

to an improved prediction of torque requested by driver corresponds an optimised SOH management and reduced degradation. Several machine learning models are trained off-line for an on-line forecast of required torque sequence. The methodology proposed includes an online updating procedure that allows to improve results obtained at a low computational costs.

As last, development of a tool to encourage BESS integration in V2G scenario and to assist energy planning management is proposed in chapter 4. The simulation software deployed aims to fill the gap by developing a configurable EVs district platform to assist DSF strategies, prepare optimization procedures, manage grid load and move from a V2B perspective to an aggregated V2G scale. The simulator allows to easily obtain charging, discharging and parking profiles related to a district. Moreover, aging models are integrated in the tool in order to integrate vehicle's life and relative performance to V2G scenario. Thus, users can simulate and test algorithms, supervisors and aggregators to provide flexibility.

Chapter 2

Li-ion Storage: State of Health

2.1 Overview

2.1.1 Li-ion technological overview

Li-ion battery cells are composed of four elements those mainly determine the power and energy capability of batteries: a cathode and an anode immersed in an electrolyte and divided by a separator, as shown in figure 2.1 [53].

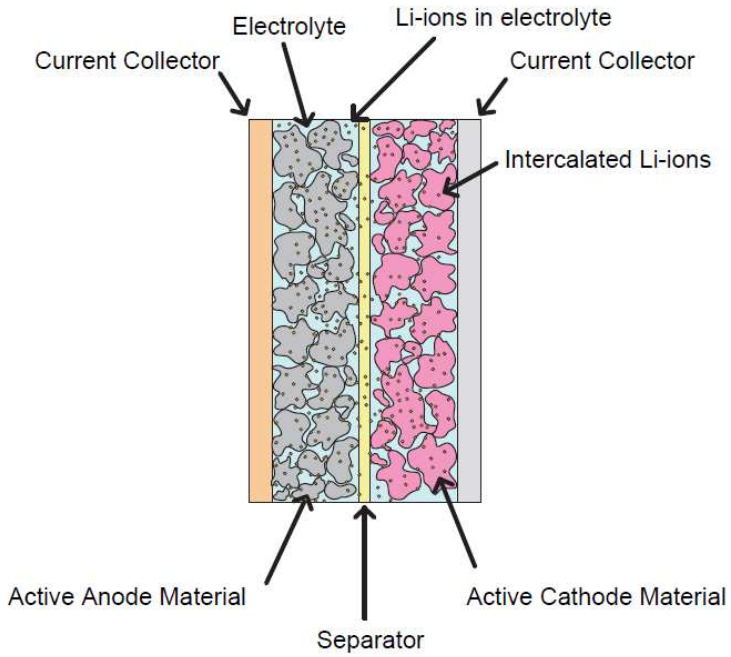

Figure 2.1: Cell internal structure. The figure is taken from [53].

The cathode represents the negative terminal and it's usually connected through an aluminium collector. Chemical structure has not been standardised and it's continuously studied, cause of its importance in determining principal operating mechanisms. Recent studies [54] report that oxide and phosphate-based materials are commonly employed, with $LiFePO_4$ and $LiMO_2$, that is a mixture of transition metal such as Ni, Mn and C, being the most promising technologies [55]. Moreover, sulfur and potassium doping, external coating treatments and specific material composition have enhanced Li-ion diffusivity, conductivity and ionic mobility ensuring high performance for high power application. Cathode element indeed gives the name to the battery itself.

Conversely, the anode represents the battery positive terminal and it's usually connected by means of a copper collector. Generally, the materials those typically compose the anode are carbon based element, which graphite is the most common choice, metallic lithium, tin or titanium-based alloys and silicon-based materials [54].

The electrolyte is usually an electrical conductive liquid or gel substance that facilitates movements of ions and stabilises cathode and anode, thus improving electrical performance. An interesting future perspective are inorganic solid electrolytes, which improve safety and represent a candidates for next-generation energy storage. Scientific community is achieving important advances in this direction [56], still it's not a widespread commercial solution.

The separator is a permeable membrane that allows ionic charge passage keeping the two electrodes separated.

2.1.2 Microscopical aging mechanisms

The main microscopic aging mechanisms occurring inside a cell are characterised by two factors [57]:

- loss of active material at both cathode and anode
- loss of available lithium ions

For the cathode lithium ions insertion and extraction cause a huge mechanical fatigue leading to structural disordering and cracks. Moreover, another factor affecting the aging is the metal dissolution from the cathode material causing a deposition on the anode. In the anode indeed, increasing formation of solid electrolyte interface (SEI) and the mechanical stress generated by diffusion on carbon particles cause the reduction of recyclable lithium ions. Studies have revealed that the SEI, formed between electrolyte and electrodes, and the deposition of metallic lithium in the anode promote the Li-ion loss [58]. Moreover, at the interface between both electrode elements and the electrolyte, an additional SEI could appear due to electrochemical decomposition reactions. The formation of SEI and passive film layers at the anode are due to the cyclable consumption of the Li-ions (charging/discharging cycles of batteries), which promotes to the formation/rupture of a thin thickness layer around it and thus being the main responsible of the Li-ion cell aging [59]. As an effect of these factors, battery performances are reduced due to capacity fading and an increase of electrical resistance. The figure 2.2 summarises all these aging phenomena.

To sum up, the microscopical effects those cause the aging behaviour of a Li-ion battery are mainly associated to three factors, namely the (*i*) Li-ions loss, the (*ii*) loss of the active resources at the anode area, and the (*iii*) loss of the active resources at the cathode area.

2.1.3 Aging characterisation

The microscopic aging mechanisms described above are strictly related to the conditions at which the battery is exposed and thus occur in both storage and utilisation modes. These last determine the aging type affecting the storage that can be characterised as calendar and cycle aging. Both aging modes effectively coexist during battery life, nevertheless the study of the combined effect is not trivial and the scientific community mainly deals with them as separated entities, as table 2.1 reports.

The calendar aging consists in mechanism that occurs when battery is at rest, stocked at fixed conditions. Thus, it is directly dependent to storage temperature, state of charge (SOC)

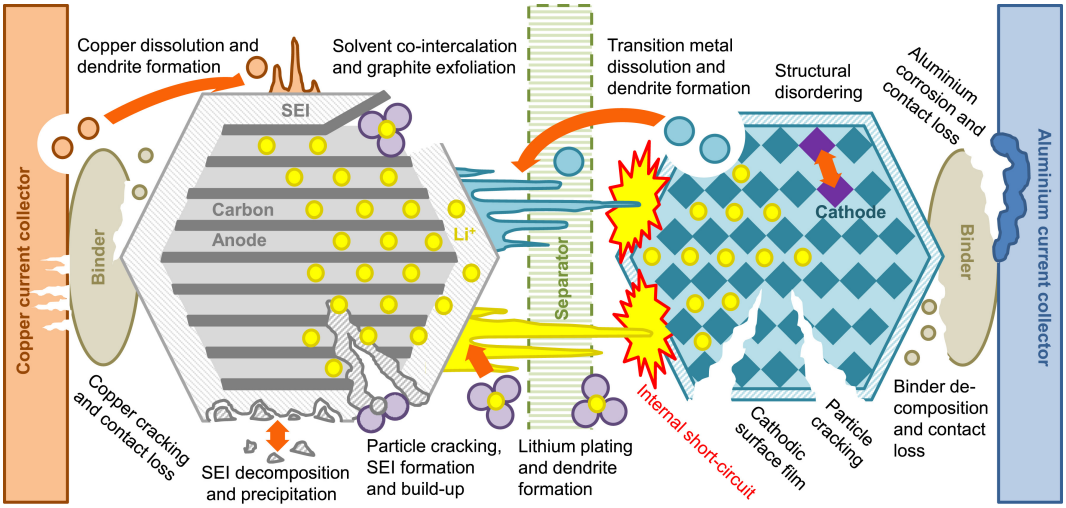

Figure 2.2: Microscopic phenomena characterising the aging of a battery cell. The figure is taken from [60].

level to which battery is maintained and the overall rest time. The cycle aging conversely is characterised by the cycling operating condition of batteries, whose main factors are temperature (ambient, pack or cell), depth of discharge (DOD), charge or discharge current and number of cycles [61].

It has been proved that batteries maintained at high temperature ($T \geq 40$řC) or at high level of SOC suffer the fast advancement of the calendar aging [62]. It is worth noting that the only load applied to batteries in these studies include a capacity test and a hybrid pulse power characterisation (HPPC) to measure battery degradation every 4 weeks, thus the overall cycle aging effects have been considered negligible.

For the cycle aging, which is the degradation of the battery due to its normal use, there are several critical factors that increase its rate of decay [63, 64]:

- High and low operating temperature ($T \geq 40°C$ and $T \leq 10°C$)
- High charging/discharging current
- High amplitude of charging/discharging
- Charging/discharging capacity, in terms of the amount of current that is totally extracted or injected to the battery

The figure 2.3 outlines these relations between storage and operating conditions and aging effect.

2.1.4 SOH definition

Both aging types, even with different causes, have the same effects: they increase the internal resistance of the battery, which worsen the power performance, but also decrease the available storage capacity [65].

The internal resistance, usually stated as R_0, determines the energy dissipated as heat due to the Joule effect. It cannot be measured directly, nevertheless its nominal value is usually reported in manufacturer's datasheet. The internal resistance significantly differs from the

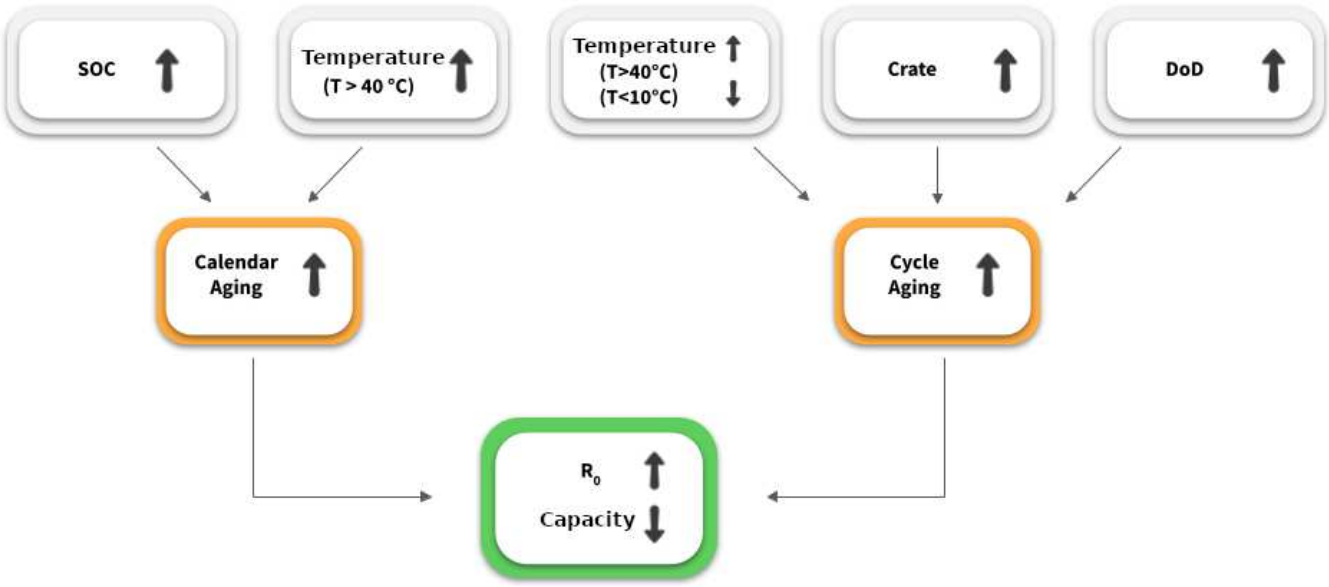

Figure 2.3: Relation between storage and operating conditions with capacity fading and increase of resistance

resistance that can be estimated from electrical model according to the amount of current injected in the battery. This will be discussed in detail later. In addition to aging dependence, battery resistance generally relies on temperature and SOC level. Resistance indeed drops instantaneously when temperature raises and conversely increase when temperature decreases [66]. Thus, even if working at high temperature could seem convenient, it represent a terrible choice because it will induce a huge effect on degradation. The effect of SOC level on internal resistance is instead considered marginal with respect to resistance variation generated by aging and temperature for li-ion batteries [67].

The maximum capacity of a battery or residual capacity (C or C_{res}) indicates the maximum amount of charge that the system is able to store and release in charge and discharge cycles. It cannot be measured directly and should be estimated through battery management system (BMS), since it computes the amount of charge that is extracted or introduced into the system. Residual capacity estimation is a challenging task and may be updated more precisely with deeper operating cycles whereas it presents several issues in case of brief charge and discharge cycles. Such quantity, similarly to internal resistance, depends on operating temperature and aging [68].

Since there's a strong relation between the internal resistance and residual capacity with aging, they are considered the main parameters to define SOH of a battery. Typically, state of health of batteries is defined as the ratio between the residual capacity C_{res} and nominal capacity C_0:

$$SOH(t) = \frac{C_{res}(t)}{C_0} \tag{2.1}$$

Less frequently, it has been computed as the ratio between the difference of actual and nominal resistance with that one at the end of life (EOL) of the battery:

$$SOH(t) = \frac{R_{EOL} - R(t)}{R_{EOL} - R_0} \tag{2.2}$$

In both cases, battery at its nominal conditions is defined with a SOH value of 1 or 100%, whereas it decreases until 0% when it becomes unusable. Value of SOH equal to 0% is not a useful indicator to determine an acceptable condition for usage. It indeed strongly depends on the field of application. Thus, EOL is specifically defined for each application according to minimum operative conditions required to the storage system. For instance, EOL for automotive application is usually set at 80% since the residual capacity reflects the vehicle range.

Another parameter to indicate the state of health of a battery is the remaining useful life (RUL), i.e. the number of cycles (or the time) needed to reach a specific EOL condition. The RUL is important in predictive maintenance and simulation scenario to determine, for instance, specific operative planning or to take corrective steps if premature aging occurs.

2.2 State of the art

State of health estimation is a topic widely studied and still remains a challenging task in international scientific research, but more specifically for real application. Several approaches developed in literature are presented, comprising both model-based and data-driven methodologies. Mainly aims, starting from training a model, build relation that can describe degradation dynamics from main characteristics passed as input. Unfortunately, many studies have explored and validated methodologies based on experimental laboratory setup rather than real application dataset; this gap has to be covered. In aging context, circuital models, those are usually employed to estimate BESS operating characteristics, are explored to provide addition information for state of health estimation. Therefore, circuital model and a review of several methodologies described in literature aiming to SOH estimation are presented in this section.

2.2.1 Electrical circuit model

Circuital models are physical models those aim to describe electrical behaviour of storage system and take into account the principal macroscopic characteristics those affect battery operating condition. Three different kind of models have been widely studied in scientific literature: zero-order, first-order and, although with less extent, second-order models. These representations are defined by parameters which are affected from battery state of health or that allow to estimate actual SOH. The most interesting ones are indeed the internal resistance (R_0) and open-circuit voltage (OCV or V_{OC}). R_0 depends on storage temperature (T) and SOC, whereas the V_{OC} is related only with the state of charge as described in equation 2.3.

$$V(t) = V_{OC}(SOC) + R_0(SOC, T) \cdot I(t) \tag{2.3}$$

The zero-order model contains all quantities those are usually contained in manufacturer datasheet[69], thus, although the approximation of the charging and discharging battery dynamics, it represents most direct and feasible model for practical application.

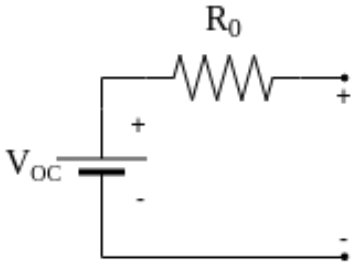

Figure 2.4: Zero-order electrical circuit model

Circuital model of the first-order allows to describe with greater accuracy battery dynamics. It indeed considers additional parameters, such as the polarisation resistance R_p and polarisation capacity C_p. They both constitute the polarisation impedance Z_p and describe electrochemical phenomena those occur inside battery cells, such as the lithium ions diffusion, intercalation and redox reactions which influence electrical battery behaviour. As disadvantage however, these polarisation quantities don't reflect real components, thus they are not measurable and must be estimated, adding complexity to the model and reflecting the necessity of enough experimental or real data for estimation. Only few manufacturer provide this estimates. Despite of these disadvantages, first-order models are widely used in literature [70, 71, 72].

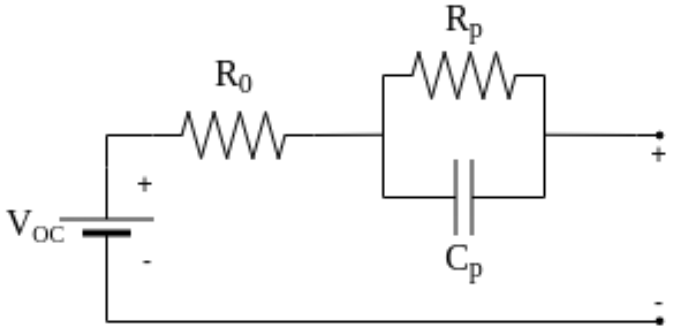

Figure 2.5: First-order electrical circuit model

In literature, higher order model are described, which are representations characterised by n additional RC components arranged in series, where n indicates the respective order of the model. These models enable a more accurate description of battery dynamics, although an addition of parameters increase the effort in parameters identification that makes them an unfeasible solution for most real application, due to the too low sampling frequency often used to acquire data and a risk of over fitting. However, though less extensively, second order models are implemented and investigated in several studies [73, 74].

2.2.2 State of health estimation

As regards SOH estimation, several models have been extensively investigated and developed by other researchers. Several parameter-based approaches have been proposed with the aim to identify relation between equation and degradation dynamics, ranging from first-principal based model to mathematical functions. In [75], the authors proposed a numerical model for the SOH estimation of grid-connected BESS relied on the efficiency index that is estimated

by two test protocols based on standard equipment and just on charge/discharge tests. In [76], a SimPowerSystems block is presented to model the charge and the discharge dynamics of the battery and the simulate aging effects due to cycling as well. The model is validated experimentally with four batteries types. A similar model developed in SimPowerSystems is proposed in [77]. The aging is estimated in function of number of charge-discharge cycles that the cell has undergone. In [78], the effects of temperature and SOH variations are integrated in the battery model. The aging model depends on the battery temperature and voltage or SOC. Reduction of the battery energy storage capability is considered by a methodology considering both a calendar and a cycle aging model. The model is based on the battery state of energy [79]. In [80], the authors developed an adaptive partial differential equation observer for battery state-of-health estimation. In [81], the investigation of the behavior of lithium-ion batteries, in particular for C/LFP batteries during calendar life at different storage conditions, is addressed. An overview of available methods and algorithms for on-board capacity estimation of lithium-ion batteries is proposed in [82]. The maximum energy storage capability estimation acts as an indicator for battery SOH and remaining useful lifetime estimation. Battery SOH monitoring is thereby a topical issue and its estimation methodologies are reviewed in [83] as well. In [84], the authors presents a overview of the different proposed battery, thermal and aging models classified in three categories: mathematical models, physical models, and circuit models. In [85], the authors investigates the degradation of the internal resistance of a lithium-ion battery based on extended laboratory calendar aging tests. Starting from the model described in [64], a generic model applied to estimate the cycling fade at each time step is proposed in [86] for the application in automotive sector. Li et al. introduce the application of rain-flow algorithm for cycle counting and a battery aging index based on DOD and Crate [87]. Omar et al. propose univariate models and least-square fitting method for cycle aging [63]. Wang et al. [64] developed a life cycle model for C/LFP batteries. The model has been developed based on statistical experimental results, whereby the proposed battery has been cycled at different operating conditions for ambient temperature, current rates, and depth of discharge. Zabala et al. [88] a combined calendar and cycle aging is investigated with dynamic and realistic complex operation profile. Baghdadi et al. [89] study the effect of calendar and power cycling aging under different aging conditions for two different battery technologies. They propose a battery aging rate index that depends on current, temperature, battery SOC in one expression.

Another part of the scientific research field has focused its effort on studying data-driven approaches in order to estimate the battery SOH. In [90], the authors investigate the nonlinear frequency response analysis tool for data-driven SOH identification of Lithium-ion batteries. Pan et al. propose a joint model-based and ELM-oriented framework for online SOH estimation [91] and Fang et al. propose a joint estimator using double extended Kalman filter for SOH estimation [92]. A similar approach based on Kalman filter and support vector regression is described in [93]. In [94], the features are extracted from voltage data and they are scored based on prognostic metrics to select diagnostic features which can conveniently identify battery degradation. Afterwards, an ensemble learning model is developed to capture the correlation of diagnostic features and batterys SOH. In [95], the authors propose a novel ensemble learning framework to estimate the battery SOH and a self-adaptive differential evolution algorithm to effectively integrate the weak learners, avoiding the trial and error procedure on choosing the trial vector generation strategy and the related parameters in the traditional differential evolution. In [96], the authors extract several features that describe

the aging process of batteries and use them to build a XGBoost model for SOH estimation of lithium-ion battery. Then, the estimation value is corrected by Markov chain. A state-of-the-art of data-driven appoaches for the SOH estimation is reported in [97]. Finally, a battery degradation model has been investigated using an electro-chemicalthermal model built in Comsol Multiphysic [98].

To sum up the review analysis, Table 2.1 lists the references described so far. The table shows also some indexes to group the different references: *calendar aging* and *cycle aging* indicate what the references propose among calendar or cycle aging models, *completeness* defines whether the model proposed includes all the main variables those affect degradation (SOC, DOD, Crate, BESS temperature), *review* indicates that the reference presents a literature review related to the battery aging, *not validate* means that the BESS aging model is not validated with real experiments and finally, *model-based* specifies whether the proposed solution is based on parametric model, considering both mathematical and first-principle based model, or otherwise it is data-driven.

Table 2.1: Aging model: state of the art

Reference	**Calendar aging**	**Cycle aging**	**Completeness**	**Review**	**Not validated**	**Model-based**
Tremblay et al. [76]		√				√
Huria et al. [77]		√				√
Barrera et al. [78]		√				√
Guenther et al. [79]	√	√	√			√
Moura et al. [80]		√			√	√
Omar et al. [81]	√					√
Farmann et al. [82]				√		√
Berecibar et al. [83]				√		√
Barcellona et al. [84]				√		√
Stroe et al. [85]	√		√			√
Yuksel et al. [86]		√	√		√	√
Li et al. [87]		√				√
Wang et al. [64]		√	√			√
Omar et al. [63]		√	√			√
Baghdadi et al. [89]	√	√	√			√
Zabala et al. [88]	√	√	√			√
Ragone et al. [98]		√				√
Rancilio et al. [75]		√				
Harting et al. [90]		√				
Pan et al. [91]		√				
Fang et al. [92]		√				
Khaleghi et al. [94]		√				
Meng et al. [95]		√				
Song et al. [96]		√				
Vidal et al. [97]		√				
Andre at al. [93]		√				

2.3 Sensitivity analysis

The development and the training of an aging model feasible for real application is a challenging task. Training phase should produce a model that is able to represent appropriately the degradation behaviour contained in a specific dataset, but more importantly the model has to be robust when it's used with different input values from those used in training step. For real application particularly, because usage condition cannot be controlled as in experimental laboratory context and operating conditions can present several profiles, a solution that is not able to generalise over different data or that varies hugely when subject to small variation, affected then by model overfitting, has to be avoided. In real cases, dataset often acquired are usually referred to one or some specific operating conditions, not covering a wide range of intensities and type of usage, weather conditions or other parameters those could be related for example to geographical position or to driving profiles in the case of an EV.

Thus, sensitivity analysis, i.e. the study of how a model deal with an unexpected variation in input variables with respect to training dataset, is conducted to evaluate the applicability of a model in real context. For this study, three models described in literature [63, 64, 89] are selected. The main selection criterion considered is the completeness of the model, in terms of inclusion of the principal macroscopic quantities affecting aging such as temperature, charge/discharge current, DOD and SOC. In [63] four mathematical equations are employed to describe separately real acquisition based on variation of the principal quantities affecting aging. Since input variables are treated individually, these models can be easily trained. Wang et al. [64] used an exponential model that is widely employed when dealing with cumulative degradation dynamics in scientific literature [99] since its robustness and easy parameters identification procedure. Finally, in [89] both calendar and cycle aging dynamics are implemented using only one model, improving its feasibility in several conditions to the detriment of an increase of complexity in terms of number of parameters. Selected models are further detailed in section 2.3.2.

2.3.1 Material and methods

Sensitivity to variation of temperature and current are considered, since they represent the principal cycling factors those impact on battery life [100]. Simulated data of a 160 Ah BESS are used for the whole analysis. Data are built changing one at a time both temperature and current keeping the other fixed. Current values are varied among $\{0.1, 0.25, 0.5, 0.75, 1\}$C whereas temperature values considered are $\{20, 25, 30, 35\}$°C. For each value, a residual capacity curve is generated as shown in figure 2.6 and figure 2.7. Then models are trained on curve associated to 0.1 C and 1 C for current sensitivity analysis and to 20°C and 35°C for temperature one. Particle Swarm Optimisation (PSO) algorithm [101] is employed to obtain optimum model parameters because of its effectiveness to deal with non linear function. In the end, each model previously trained is tested to the excluded values, i.e. 0.25 C, 0.5 C and 0.75 C and 25°C and 30°C for current and temperature respectively. Therefore, values selected for testing represent quantities on which model have not previously been trained. The metrics used to compare models effectiveness is the mean average percentage error ($MAPE$), as described in equation 2.4. This constitutes a coherent comparison metric for Baghdadi and Wang models because outputs computed by these models are the same (i.e. capacity), while representing an indication of error for all Omar models those return outputs in terms of number of cycles, so at a different scale.

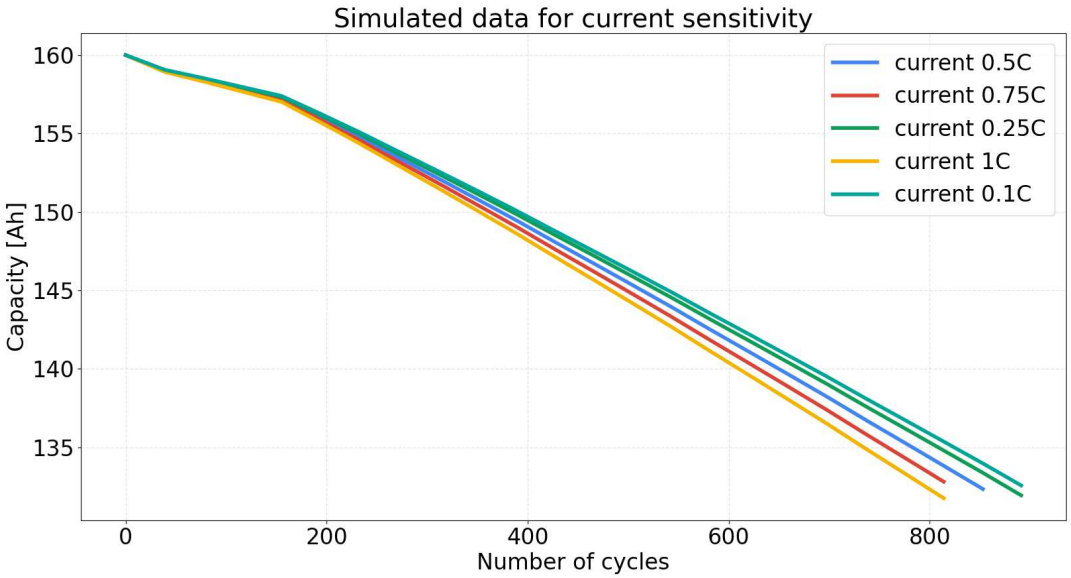

Figure 2.6: Dataset used for current sensitivity analysis. Battery residual capacity of battery is plotted in function of the number of cycles. Current values are ranged from 0.1 C to 1 C.

$$MAPE = \frac{100\%}{n} \sum_{t=1}^{n} \left| \frac{y_t - \hat{y}_t}{y_t} \right| \tag{2.4}$$

The other cycling quantities those affect an aging degradation are fixed as reported in table 2.2:

Table 2.2: Other cycling parameters used for data simulation

Fixed input	**Values**	**Notes**
DOD	85%	depth of discharge of each cycle
SOCaverage	50%	mean SOC level in each cycle
Crate	0.1 C	current (fixed during temperature analysis)
T	20°C	temperature (fixed during current analysis)

2.3.2 Model selected

In this section, the aging models selected for sensitivity study are summarised.

Baghdadi [89]

$$k_{cal}(T, SOC) = \exp(k_1 \frac{SOC}{R}) \cdot \exp(\frac{k_2}{R}) \cdot \exp(-\frac{k_3}{RT}) \tag{2.5}$$

$$a(T) = \exp(\frac{k_4}{RT} + k_5) \tag{2.6}$$

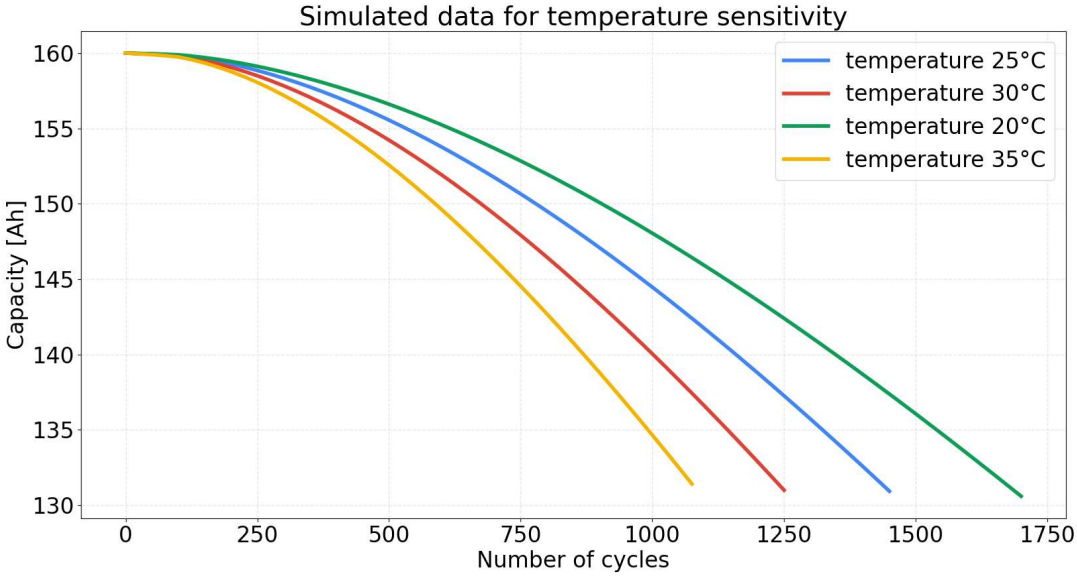

Figure 2.7: Dataset used for temperature sensitivity analysis. Battery residual capacity of battery is plotted in function of the number of cycles. Temperature values are ranged from 20°C to 35°C.

$$k_{cyc} = \exp(a(T) \cdot \frac{I}{I_0}) \tag{2.7}$$

$$k_{tot} = k_{cal} \cdot k_{cyc} \tag{2.8}$$

$$C(t) = C_0 \exp(-k_{tot} t^{k_6}) \tag{2.9}$$

The model proposed is the most comprehensive among the selected ones, though it is the more complex resulting in a potential higher risk of overfitting. It returns maximum capacity available at a defined time instant and considers both cycle and calendar aging phenomena; it's based on the computation of two parameters, namely k_{cyc} and k_{cal} those are related to cycle and calendar aging respectively, leading to a description and possible application in different real context simultaneously. The model approach aims to reproduce a chemical rate approach, based on a Dakin's degradation.
Application: Energy- and power-intensive.
Input: SOC, temperature, time, current.
Parameters: $k_i, i = 1, \ldots, 6$.
Coefficients: I_0, reference current at $1A$; C_0, nominal capacity; R, universal gas constant.
Outputs: $C(t)$, which is the capacity at a specific time.
Storage size: validated with 5.3 Ah with 4.2 V, and 7 Ah with 4 V, scalable to other sizes.
Pro: Both calendar and cycle aging are considered.
Cons: The model validation proposed is performed keeping constant SOC and temperature; furthermore, the analysis is focused on a single Li-ion cell, ignoring the internal resistance variation.
Note: in our study, the calendar contribution computation is simplified. Differently from the

author, which computed the calendar factor as the average of k_{cal} with respect to State of Charge (SOC) interval, here it's evaluated using the average SOC of charge and discharge cycles.

Wang [64]

$$Q_{loss} = k_1 \cdot \exp\left(k_3 + 370 \cdot \frac{C_{rate}}{RT}\right) \cdot (Ah)^{k_2} \tag{2.10}$$

This model evaluates the capacity loss as percentage in function of the current used and gathered in the electric storage; the exponential modeling is widely used in literature.
Application: energy- and power-intensive context.
Inputs: temperature, total amount of capacity supplied and extracted to the battery, crate.
Parameters: k_1, k_2, k_3.
Output: Q_{loss}, capacity loss in percentage due to aging.
Storage size: validated with 2.2 Ah with 3.6 V, scalable to other sizes of storage.
Pro: Computational efficiency and robustness due to the single exponential equation, inputs data always noted.
Cons: A single exponential model doesn't adequately describe the high variation of the quantities. Different training are needed based on the operating conditions.
Note: k_3 is an additional parameter included to improve model performance instead of using a constant value as in the original study.

Omar [63]

$$CL(T) = k_1 T^2 + k_2 T + k_3 \tag{2.11}$$

$$CL(I_d) = k_1 \exp(k_2 I_d) + k_3 \exp(k_4 I_d) \tag{2.12}$$

These models allow degradation description in terms of cycle life, i.e. RUL to achieve 80% of residual capacity, due to the effect of cycle aging. Each model is univariate, i.e. it evaluates aging effect according to the variation of a single input while all the others are kept fixed. Since the interest of this study is restricted to current and temperature analysis, only the models including them are reported.
Application field: The model can be applied in both energy- and power-intensive fields.
Inputs: current and temperature.
Parameters: $k_i, i = 1, \ldots, 5$.
Outputs: RUL of the battery expressed in cycles.
Storage size: 2.3 Ah with 3.3 V. It is scalable to other dimensions.
Pros: It allows to study multiple parameters regarding the aging. It has been also experimentally tested and validated.
Cons: The variables that are not evaluated through equations are considered as constant parameters.
Note: in this study polynomial equation 2.11 is reduced of one degree with respect to the model proposed in literature. The simplification, since the coefficient relative to the third degree term is evaluated to be close to zero, is introduced to avoid overfitting and simplify training phase. Since these models estimate the number of cycles executed to reach a specific capacity threshold, many set of parameters are trained, each for a different residual capacity value, such that the capacity degradation curve could be modeled. As last, for temperature modeling, k_1 is forced to be lower than zero according to data shown in paper.

2.3.3 Results

In this study, effect on several aging models of variation of temperature and current with respect to the values on which models are trained, is investigated in order to evaluate which model presents a more robust behaviour. Data of 160 Ah BESS are simulated for this study varying both temperature and current singularly, maintaining the other fixed. In the case of current, models are trained on 0.1 C and 1 C and tested on 0.25 C, 0.5 C and 0.75 C; for temperature, 20°C and 35°C curves are used for training while 25°C and 30°C for testing. Parameters computed and $MAPE$ are reported. Results of temperature and current are presented separately.

Temperature

Trained parameters for temperature sensitivity are reported in tables 2.3, 2.4 and 2.5. Each model is characterised by a different number of parameters according to the mathematical equations described in section 2.3.2.

For Baghdadi model, the six parameters characterising the equations are reported presenting relatively large numbers, highlighting the risk of being sensible to variation due to the presence of nested exponential functions in the model.

Table 2.3: Trained Baghdadi model parameters for temperature

k1	**k2**	**k3**	**k4**	**k5**	**k6**
4565.029	-2298.808	4999.728	1.331	-1874.153	-2389.017

The three Wang parameters as described in model equation are computed returning a very low $k1$ parameter value in modulus.

Table 2.4: Trained Wang model parameters for temperature

k1	**k2**	**k3**
6.362×10^{-6}	1.228	-799.922

Since Omar model equation describes degradation in terms of number of cycles necessary to reach a specific levels of residual capacity, a set of three parameters is computed for each value of capacity threshold, as reported in the first column of table 2.5. Thus, model is trained on seven level of residual capacity, returning the same number of set of parameters which are then used to compute error from simulated curves in terms of number of cycles.

By means of the parameters computed, all the models are tested on capacity curves related to 25°C and 30°C. Figure 2.8 shows Baghdadi (red and blue lines) results obtained at 25°C and 30°C. The model reasonably follows the decreasing trend of simulated data plotted as green and yellow curves on which it wasn't trained, reaching a maximum error of 8.04Ah, a mean absolute error (MAE) of 1.82Ah and a root mean square error (RMSE) of 2.52Ah. However, reproduced curves are sensibly close, underlying a lack of the model on generalising among these temperature values.

Similar results are reported for Wang but reporting a slight increase in error computed, reaching a maximum error of 9.1Ah, a MAE of 2.09Ah and a RMSE of 2.9Ah. Figure 2.9 shows Wang model tested at 25°C and 30°C with red and blue lines. Anyway it reasonably follows the behaviour described by yellow and green simulated curves on which it wasn't

Table 2.5: Trained Omar model parameters for temperature. Each parameters row is related to residual capacity threshold of the first column.

$C_{res}[\%]$	**k1**	**k2**	**k3**
100	-0.261	14.332	-82.402
99.375	-0.595	26.041	17.054
98.125	-0.981	40.631	79.844
96.875	-1.259	55.916	-14.692
93.75	-1.978	88.767	-84.313
91.25	-2.345	102.314	-8.235
86.875	-3.060	134.971	-75.395

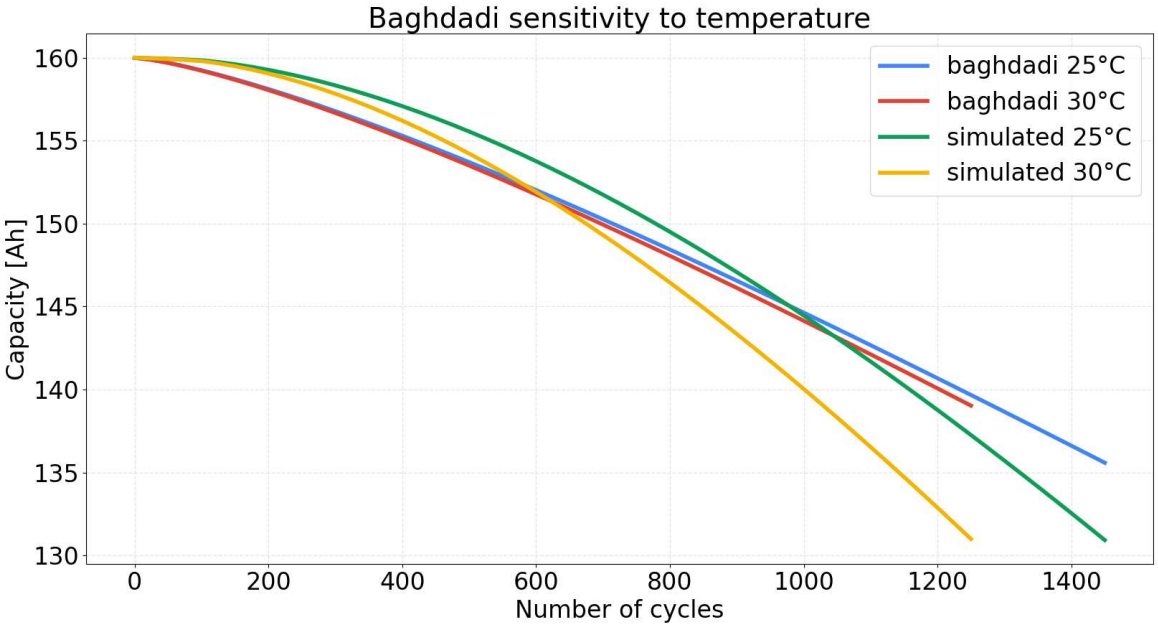

Figure 2.8: Baghdadi model tested at 25°C (blue line) and 30°C (red line). It reasonably follows simulated data, reaching a maximum error of 8.04Ah, a MAE of 1.82Ah and RMSE of 2.52Ah

trained.

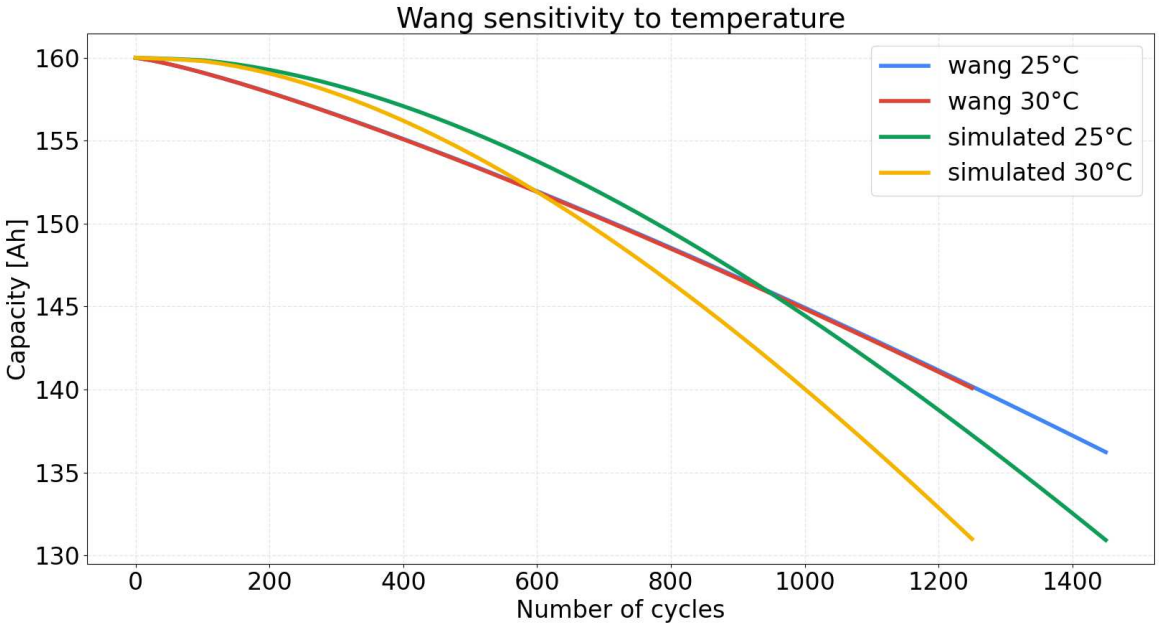

Figure 2.9: Wang model tested at 25°C (blue line) and 30°C (red line). It reasonably follows simulated data on which it wasn't trained, reaching a maximum error of 9.1Ah, a MAE of 2.09Ah and a RMSE of 2.9Ah.

Finally, differently from Baghdadi and Wang models, the seven outputs indicating the number of cycles necessary to reach a particular related to the respective set of parameters are computed for Omar model. Figure 2.10 depicts modeling results at 25°C and 30°C. It slightly overestimates simulated data on which it wasn't trained, reaching a maximum error of 180 cycles, a MAE of 50 cycles and a RMSE of 75 cycles for the seven modeled values.

MAPE computed for temperature to compare models performances is reported in Table 2.6. The most robust model to temperature variation is Baghdadi for both 25°C and 30°C, though marginally with respect to Wang. The worst performance is obtained by Omar, particularly for the 30°C curve. Moreover, since Omar modeling does not consider any other quantities and involves a more complex training phase because it requires to compute a set of parameter for each residual capacity value desired, it does not represent a feasible solution with respect to the others. Although both Baghdadi and Wang cannot significantly discriminate aging evaluation among the two values of temperature, Baghdadi is slightly more robust and represent the best choice when considering temperature variation. However, experimental data reported in Omar et al. [63] indicate that 20°C is the optimal temperature condition which ensures a greater RUL, whereas a decrease of life cycles is expected for temperature lower and greater than 20°C. Conversely to Wang model which describe each residual capacity point at different temperatures with a concave downward parabola, Baghdadi and Wang are not able to reproduce that behaviour unless a training curve with temperature lower than 20°C is used.

Current

Trained parameters, according to the mathematical models described in section 2.3.2,

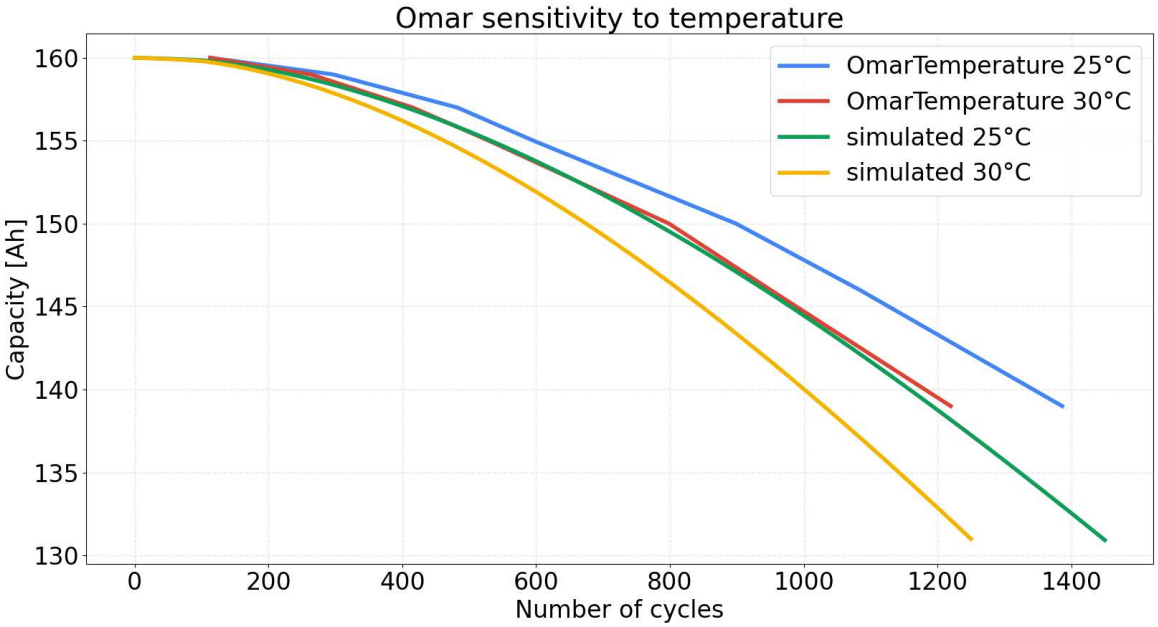

Figure 2.10: Omar model tested at 25°C (blue line) and 30°C (red line). It slightly overestimates test data, reaching a maximum error of 180 cycles, a MAE of 50 cycles and a RMSE of 75 cycles.

Table 2.6: MAPE computed for temperature sensitivity

Temperature	**Wang**	**Baghdadi**	**Omar**
$25°C$	1.19 %	1.05 %	3 %
$30°C$	1.79 %	1.54 %	13.09 %

for current sensitivity are reported in tables 2.7, 2.8 and 2.9. For Baghdadi model, the six parameters characterising the equations are reported resulting in large numbers with respect to current variation passed as input, highlighting the risk of being sensible to variation due to the presence of nested exponential functions in the model.

Table 2.7: Trained Baghdadi model parameters for current

k1	**k2**	**k3**	**k4**	**k5**	**k6**
2661.486	-1361.219	-318.699	1.319	-1096.049	1.713

The three Wang parameters as described in model equation are computed returning a very low $k1$ parameter value in modulus.

Table 2.8: Trained Wang model parameters for current

k1	**k2**	**k3**
9.81×10^{-6}	1.25	-635.860

Similar to above for temperature, for Omar model a set of four parameters is computed for each value of capacity threshold, as reported in the first column of table 2.9. Thus, model is trained on sixteen level of residual capacity, returning the same number of set of parameters which are then used to compute error from simulated curves in terms of number of cycles.

Table 2.9: Trained Omar model parameters for current. Each parameters row is related to residual capacity threshold of the first column.

$C_{res}[\%]$	**k1**	**k2**	**k3**	**k4**
100	13.69	-989.066	-20.44	-993.074
99.375	274.123	-675.799	84.245	-0.770
98.75	116	4.257×10^{-17}	667.176	-479.812
98.125	155	2.606×10^{-9}	219.112	-202.168
97.5	194	-1.449×10^{-14}	-229.219	-321.364
96.25	275.588	-0.168	231.643	-686.973
95.625	314.666	-0.149	160.136	-391.729
93.75	392.599	-0.118	-296.494	-498.801
93.125	430.445	-0.104	-464.388	-538.636
91.25	508.53	-0.089	197.177	-987.357
90	590.251	-0.158	181.206	-302.273
88.125	83.219	-109.698	668.287	-0.14
87.5	707.251	-0.132	173.989	-699.821
86.25	745.093	-0.123	-273.609	-385.423
84.375	823.162	-0.112	-270.926	-775.372
83.125	-302.86	-274.405	904.916	-0.155

By means of the parameters computed, all the models are tested on capacity curves related

to 0.25C, 0.5C and 0.75C. Figure 2.11 shows Baghdadi model (red, blue and green lines) tested at 0.25C, 0.5C and 0.75C. It overestimates simulated data (orange, yellow and aqua green curves) on which it wasn't trained, reaching a maximum error of 14.17Ah, a MAE of 5.72Ah and a RMSE of 7.02Ah, although the model moderately follows the decreasing trend.

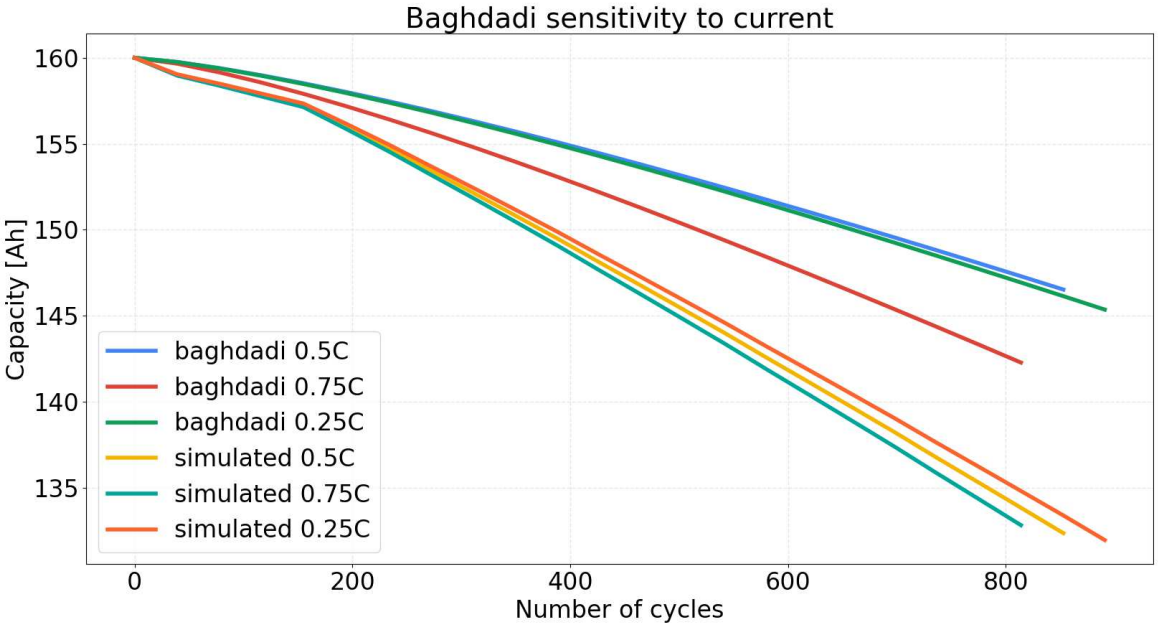

Figure 2.11: Baghdadi model tested at 0.25C (green line), 0.5C (blue line) and 0.75C (red line). It overestimates simulated data, reaching a maximum error of 14.17Ah, MAE of 5.72Ah and a RMSE of 7.02Ah.

Figure 2.12 depicts Wang model performance when tested at 0.25C, 0.5C and 0.75C. It successfully follows simulated data on which it wasn't trained, highlighting a high robustness to variation of Crate. The numerical results report a maximum error of 0.57Ah, a MAE of 0.17Ah and a RMSE of 0.22Ah, supporting the graphical outcome.

Along with Wang results, Omar model significantly represent simulated data on which it wasn't trained underlying its robustness as well. Figure 2.13 shows Omar model tested at 0.25C, 0.5C and 0.75C, representing the sixteen number of cycles values computed by the model. It reaches a maximum error of 95 cycles, a MAE of 25 cycles and a RMSE of 34 cycles.

MAPE computed for current to compare models performances is reported in table 2.10. The most robust model to current variation is Wang for all Crate values.

The worst performance is obtained by Omar, particularly for the 0.25 C curve. Moreover, since Omar modeling does not consider any other quantities and involves a more complex training phase obtaining a set of parameter for each capacity value, it does not represent a feasible solution with respect to the others. Baghdadi performs slightly better than Omar but it's not comparable with results obtained by Wang model, with a MAE of 5.72 Ah. Thus, Wang is the most robust and represent the best choice when considering current variation.

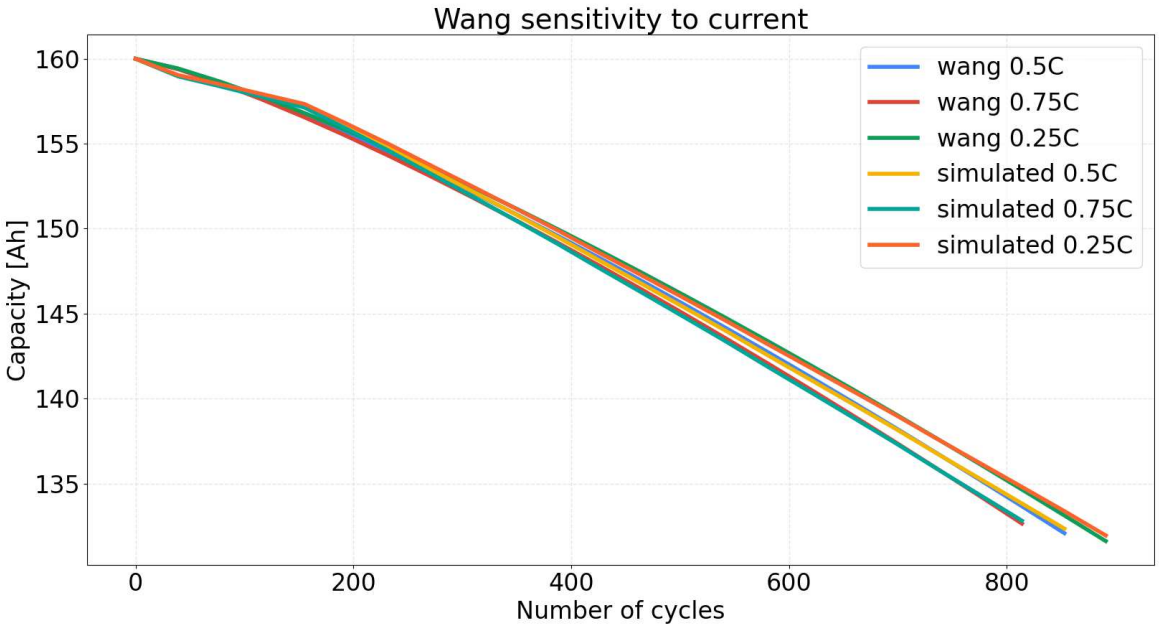

Figure 2.12: Wang model tested at 0.25C (green line), 0.5C (blue line) and 0.75C (red line). It successfully follows simulated data, reaching a maximum error of 0.57Ah, a MAE of 0.17Ah and a RMSE of 0.22Ah.

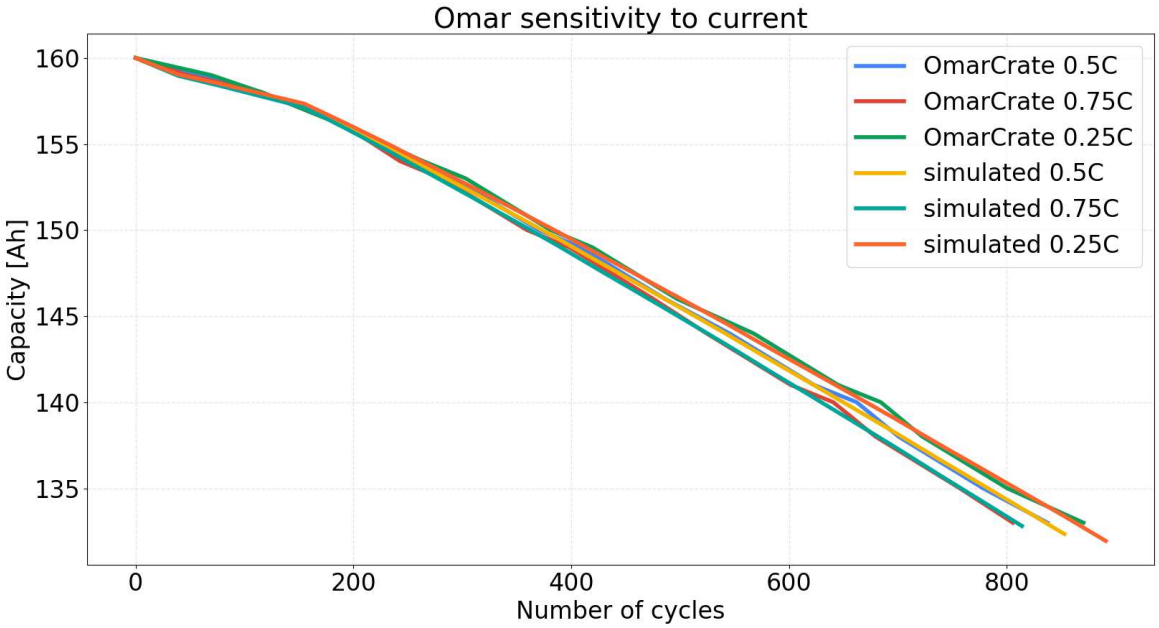

Figure 2.13: Omar model tested at 0.25C (green line), 0.5C (blue line) and 0.75C (red line). It reasonably follows simulated data, reaching a maximum error of 95 cycles, a MAE of 25 cycles and a RMSE of 34 cycles.

Table 2.10: MAPE computed for current sensitivity

Crate	**Wang**	**Baghdadi**	**Omar**
0.25 C	0.12 %	4.4 %	12.03 %
0.5 C	0.11 %	4.62 %	7.62 %
0.75 C	0.12 %	3.09 %	3.63 %

2.4 Data driven approach

Since the wide diffusion and the ongoing growth of BESS in several technological applications, the capability to model aging behaviour among different operating condition is an increasingly crucial challenge. Furthermore, the implementation of a methodology able to run online and estimate battery degradation with regardless of working condition of BESS is important as well, since in stationary application context BESS could be used either for delivering huge amount of power in a brief period to manage frequency fluctuation or to store energy to assist grid flexibility demand. Thus, the development of an algorithm able to estimate online SOH in real application scenarios, without a priori knowledge about its operating condition is studied and developed to achieve company requirements as a part of an R&D project.

Data used to test proposed methodology have been acquired in utilities context, where BESS operates as both energy and power intensive storage. Power intensive behaviour is characterised by a high power delivered in limited time, ensuring security and inertia to power system; conversely, energy intensive is mainly composed of cycles able to deliver or accumulate a great amount of energy for prolonged period, leading to load balance and shifting and decreasing grid congestion. The first are typical of auxiliary services, e.g. in primary/secondary frequency regulation, the latter can handle the increasing fluctuation due, for example, to the intermittence of renewable resources. Thus, contribution of energy intensive services will increase its importance with the raise of renewable capacity, that already overcomes the actual electricity demand in some hours during specific days [102]. EV's BESS, due to the nature of vehicle usage, can be assumed to be energy intensive and can be modeled as a storage that deliver or absorb power for relative prolonged time.

In this study, in order to address these different operating applications, several challenges have been addressed:

- automatic definition of modality of storage use, i.e. whether it's cycled through power or energy intensive profiles.
- obtaining from macroscopic and easy to measure quantities an aging modeling approach able to describe degradation effect.
- define similar operating conditions throughout the BESS life on which estimate SOH.
- not uniform sampling time among datasets.

Dataset obtained from each BESS containers includes sensor information about current, voltage and temperature down to a single rack. Moreover, each BMS estimate SOC level of the battery and it's included in this study. Since three BESSs case studies with different acquisition protocols have been included in the study, sampling time is not uniform among the three case studies ranging from 2 seconds to 1 min. Table 2.11 resumes the three BESS size and operating characteristics.

Algorithm developed can be summarised in three main steps:

1. Usage Modality Recognition: BESS usage is detected among a power intensive, an energy intensive or an undefined behaviour.
2. Similar Operating Condition Definition: in order to obtain a more accurate estimate SOH it's necessary to identify when BESS operating condition are comparable throughout BESS life. In power intensive case, V_{OC} is estimated.
3. *SOH* estimation based on different BESSs mode and operating conditions.

Table 2.11: Li-ion batteries size and characteristics. Energy capacity, voltage range and nominal current are reported.

	Energy Capacity [kWh]	Minimum Voltage [V]	Maximum Voltage [V]	Nominal Current [A]
BESS1	70	620	780	90
BESS2	200	680	780	450
BESS3	45	930	1050	40

Figure 2.14 show the main steps of implemented algorithm.

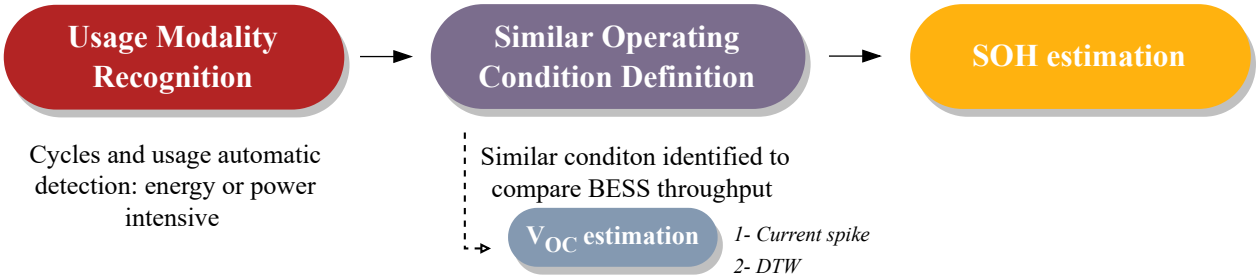

Figure 2.14: Online data driven approach

2.4.1 Usage Modality Recognition

The first algorithm step is to determine charge and discharge cycles and automatically identify whether the main BESS usage modality is energy intensive or power intensive.

Defining how the BESS is employed is crucial in order to implement a reliable SOH estimation algorithm. Once usage similarity is ensured, it's possible to compare different conditions over time according to the principal BESS operating conditions affecting aging. If battery dynamics can be assumed to be comparable, differences estimated on maximum storable energy reflects aging effect and SOH.

Charge/discharge cycles are defined as profiles where current continuously presents same signs (positive or negative respectively) and battery present at least 5% of depth of discharge, computed based on *SOC* data. In figures 2.15 - 2.18 charge and discharge cycles are represented for two of the three case studies, specifically an energy intensive and a power intensive behaviour.

Once the charge/discharge cycles are identified, the algorithm aims to define which is the principal usage modality. The problem is a multi-label classification with three output classes: *"Mostly power intensive"*, *"Mostly energy intensive"* and *"Undefined"*. A Fuzzy Inference System (FIS) is employed to classify in which modality BESS is used.

Fuzzy Inference

A zero-order Takagi–Sugeno (TS) FIS [103] is implemented to obtain usage modality from the input features. Membership functions are built with trapezoidal functions. The trapezoidal fuzzy set $\mathbf{S}$ in the universe of discourse $\mathbf{U} \in \mathbb{R}$ with the membership function $\mu_{\mathbf{S}}$ is parameterized by four real scalar parameters: (a, b, c, d) where $a < b < c < d$. The trapezoidal

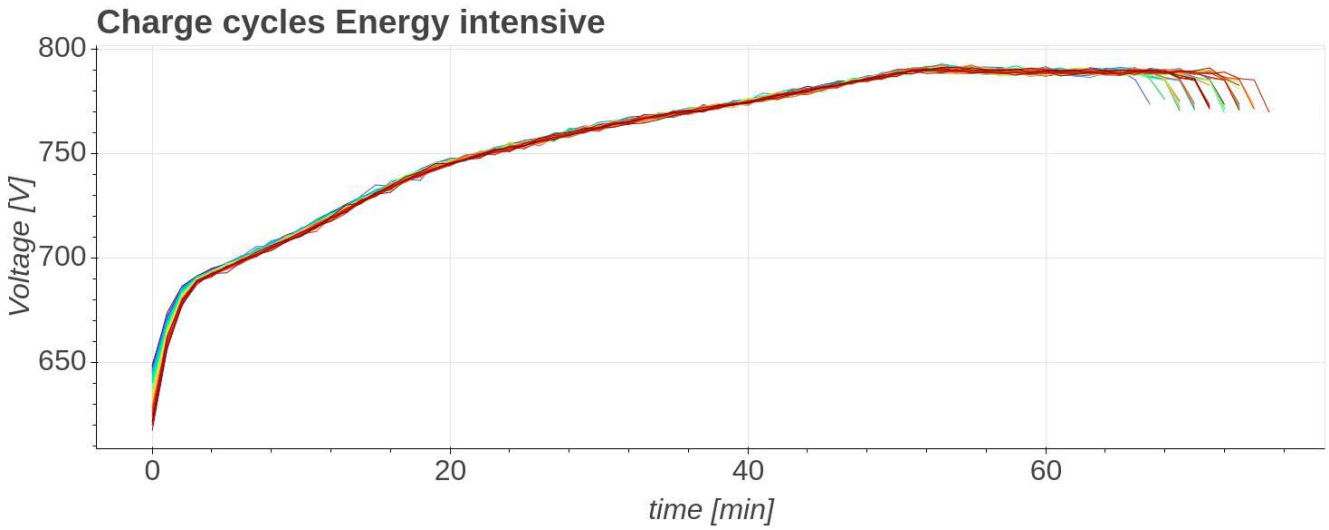

Figure 2.15: Charge cycles for energy intensive BESS

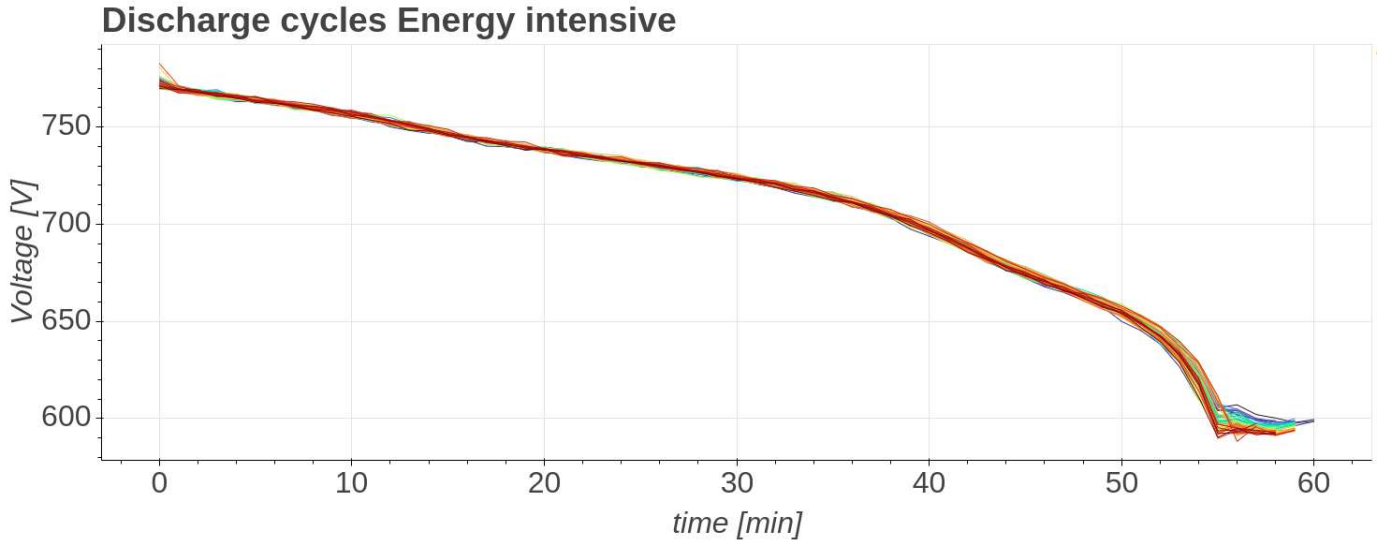

Figure 2.16: Discharge cycles for energy intensive BESS

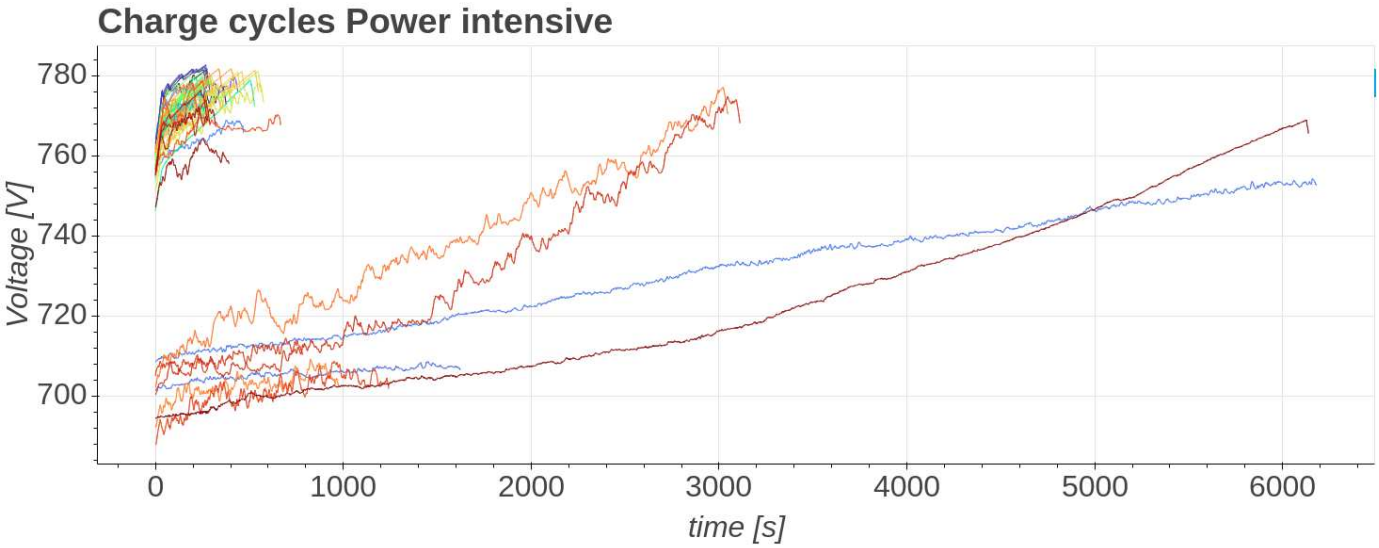

Figure 2.17: Charge cycles for power intensive BESS

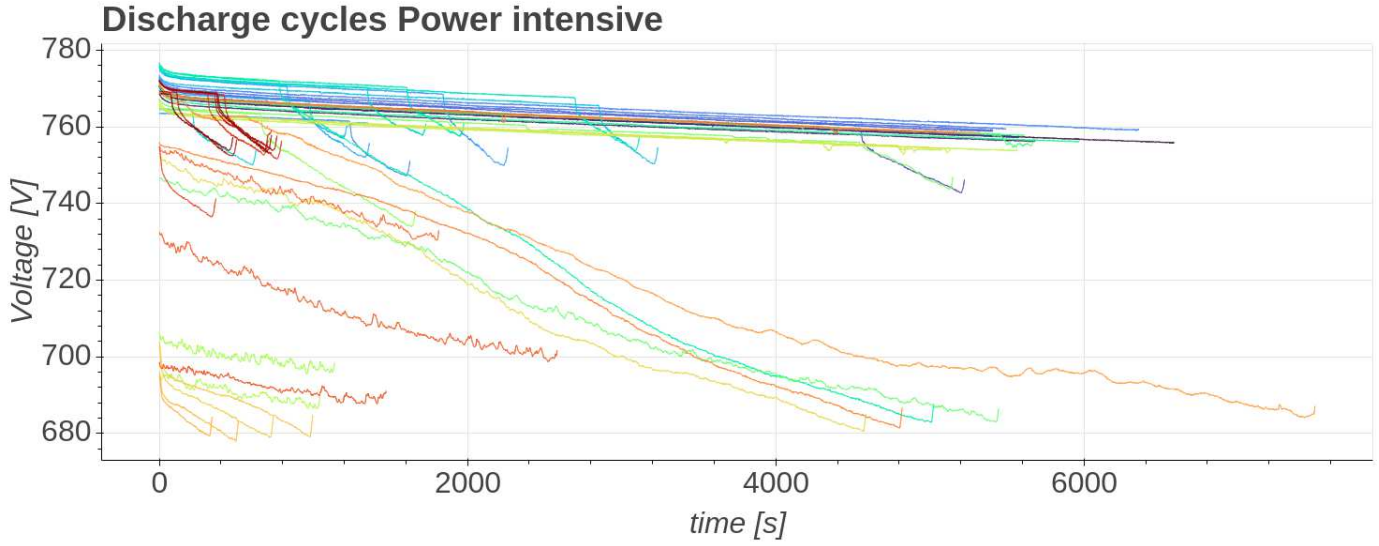

Figure 2.18: Discharge cycles for power intensive BESS

membership function is described mathematically as follows:

$$\mu_{\mathbf{S}}(x) = \begin{cases} 0, & x < a \\ \frac{x-a}{b-a}, & a < x < b \\ 1, & b < x < c \\ \frac{d-x}{d-c}, & c < x < d \\ 0, & x > d \end{cases} \tag{2.13}$$

When $b = c$, the triangular function is used and can be considered as a particular case of the trapezoidal one. The fuzzy system proposed is composed of two inputs and one crisp output (the class output). The values of the fuzzy sets are reported in Table 2.12.

Table 2.12: Fuzzy sets of the input and output variables for modality classifier: linguistic terms and their corresponding trapezoidal fuzzy set parameters.

Input Variables	**Linguistic Terms**	**Fuzzy Sets (a, b, c, d)**
Number of cycles at $P > 50\%$ [%]	Few	0, 0, 20, 40
	Many	20, 40, 100, 100
Number of cycles at $SOC > 50\%$ [%]	Few	0, 0, 30, 40
	Many	30, 40, 100, 100
Output Variable	**Linguistic Terms**	**Crispy Value**
Modality	Mostly energy intensive	1
	Mostly power intensive	-1
	Undefined	0

Output is computed through FIS rules described in table 2.13 and by means of weighted average as defuzzification method. Finally, the classification label is defined based on fuzzy output value: if defuzzification result is greater than 0 the BESS is associated to *"Mostly energy intensive"* class, if result is lower than 0 it is considered *"Mostly power intensive"* and *"Undefined"* if equal to 0.

Table 2.13: Fuzzy system rules for usage modality classification.

$\mathbf{N_{cycles}}$ $SOC > 50\%$	$\mathbf{N_{cycles}}$ $P > 50\%$	**Output**
Few	Many	Mostly power intensive
Few	Few	Undefined
Many	Few	Mostly energy intensive
Many	Many	Mostly energy intensive

2.4.2 Energy intensive

If the BESS modality is considered energy intensive, then SOH is computed directly. When batteries cycles are characterised by wide DOD range, transient dynamics can be assumed to be negligible and large range of V are considered to reflect similar operating characteristics among usage time. Thus, fixed ΔV at 20% ad 85% of minimum and maximum voltage respectively, capacity delivered or absorbed is computed in charge or discharge cycle profiles

in ΔV chosen as the amount of current injected or extracted. Capacity values are averaged over 20 cycles in order to reduce outliers and noise effect and return a more realistic results. $SOH(t)$ at the time t is then estimated as the ratio of capacity at time t and the nominal capacity at the same fixed ΔV as defined in equation 2.14.

$$SOH(t) = \frac{C_{\Delta V}(t)}{C_{\Delta V 0}} \tag{2.14}$$

Voltage is prefered over the SOC as quantity on which fix interval in operating curves. It is indeed directly measured and so it's supposed to be less noisy than SOC that is estimated by BMS with varying method depending on manufacturer, thus it could accumulate large error [104], not representing a suitable solution. Moreover, Voltage and SOC are related each other, both reflecting V_{OC}.

Figure 2.19 shows the SOH progress estimated for the case study identified as energy intensive. The non linear behaviour of degradation reflecting an increase of capacity is due to conditioning issue, when the temperature is raised and temporarily leads to an apparent boost in capacity absorbed in charge. However, capacity available to be supplied during discharge in the same period is reduced and aging effects are more severe.

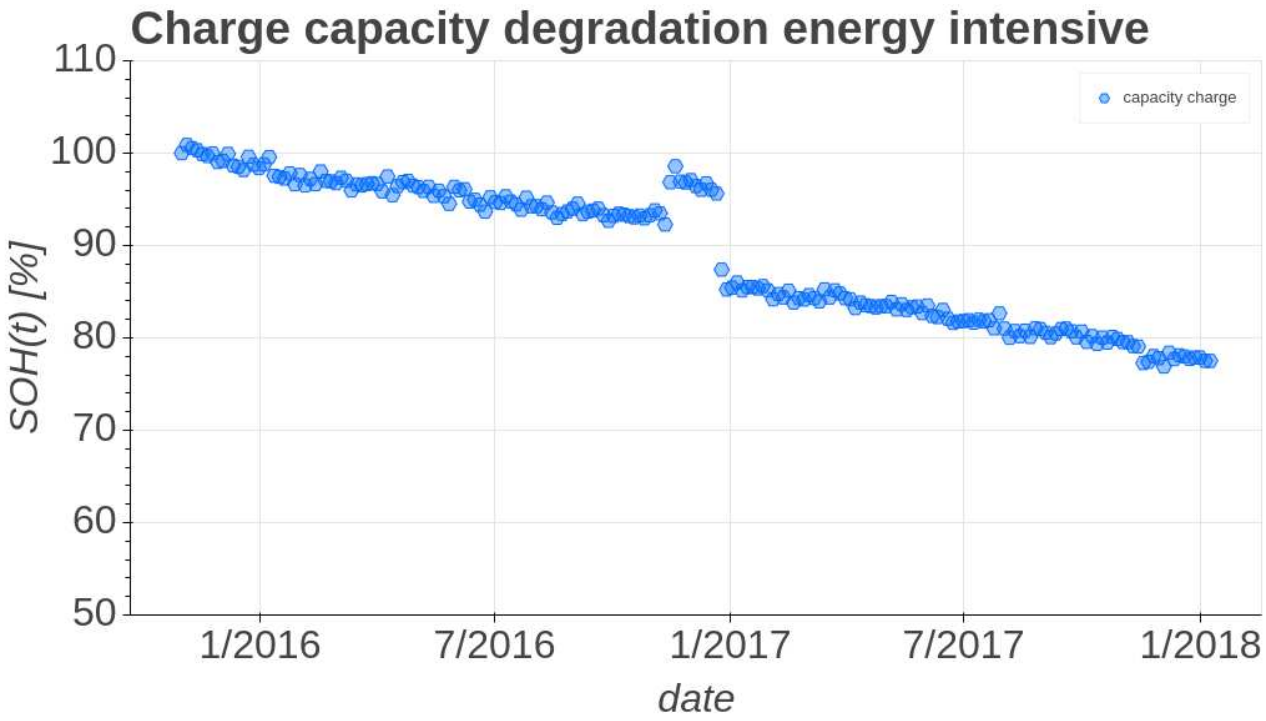

Figure 2.19: Capacity degradation in the case of energy intensive usage, each capacity point is averaged over 20 cycles.

2.4.3 Power Intensive

Power intensive behaviour is typical of grid application and more specifically of auxiliary services and grid support (e.g. frequency regulation) application. Identifying similar operation range within this context, where DOD intervals are limited, is more challenging, since battery dynamics can be different between various SOC level and comparing energy stored or delivered

in a specific ΔV could be affected by noise due to transient dynamics that occur differently according to various chemical reaction connected to the SOC level. Thus, if the storage is considered to mainly cycle in power intensive mode, different analysis have been conducted to achieve the detection of similar operating condition during BESS lifetime. Once two similar conditions are detected, then capacity can be compared.

V_{OC} is the battery characteristic that directly reflects battery state without being affected of transient electrochemical dynamics. Thus, V_{OC} is the BESS quantity that algorithm aim to estimate to define similar operating conditions as described above. In figures 2.20 and 2.21 an example of two different power intensive profiles is shown. Figure 2.20 depicts a battery profile characterised by numerous spikes in current time series, while this behaviour less frequently occurs in operating conditions shown in figure 2.21.

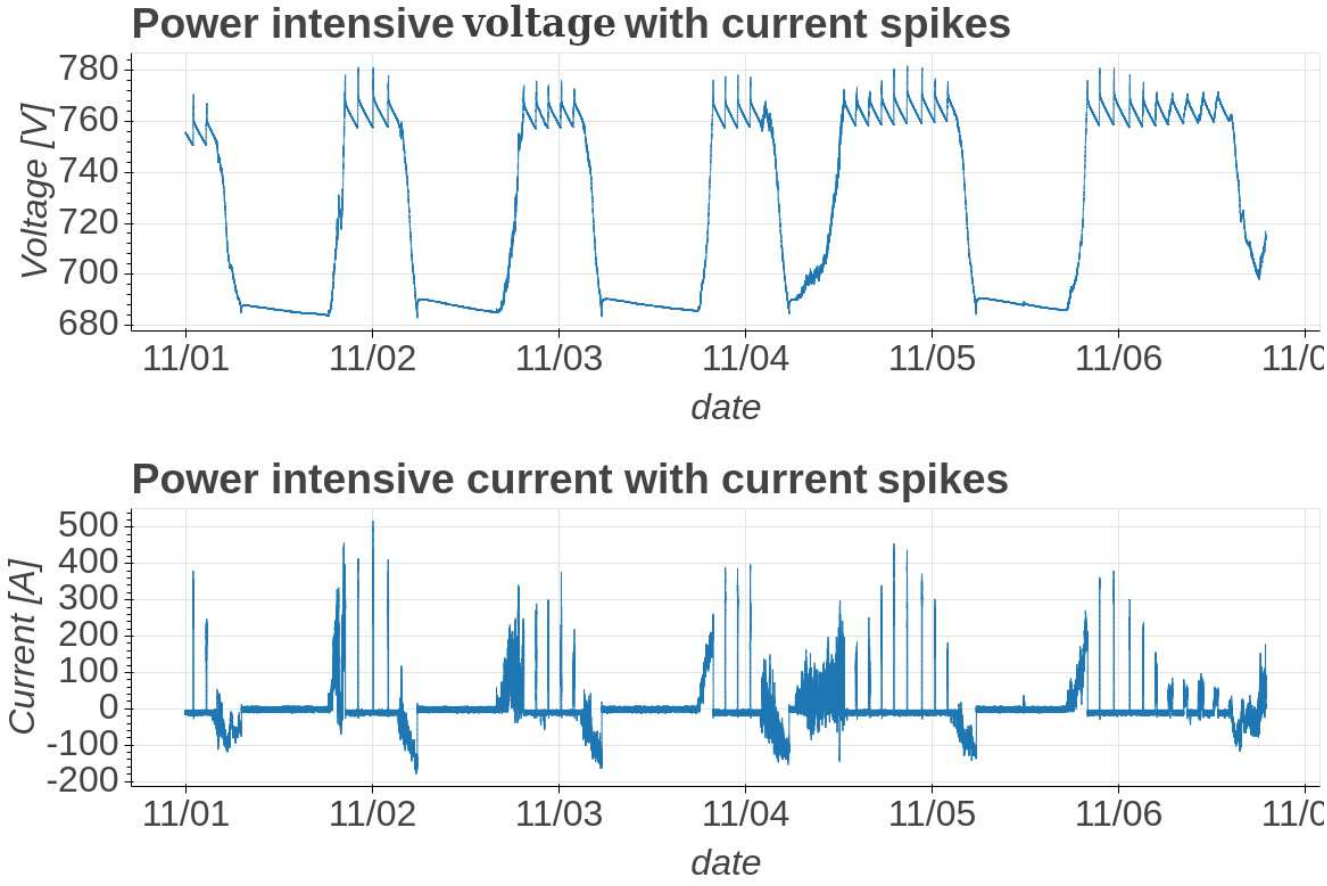

Figure 2.20: Example of BESS2 operating profiles mostly characterised by a power intensive behaviour. Numerous spikes can be observed in current time series leading to a more accurate R_0 estimation, as described in section 2.4.3.

V_{OC} estimation

The algorithm estimates V_{OC} by means of two possible approaches depending on the presence of profiles characterised by a fast and huge raise of current (current spikes). Both possible methodologies are based on zero-order electrical circuit model, described previously by equation 2.3 and figure 2.4.

Current spikes are defined as profile characterised by an absolute current rise at least at

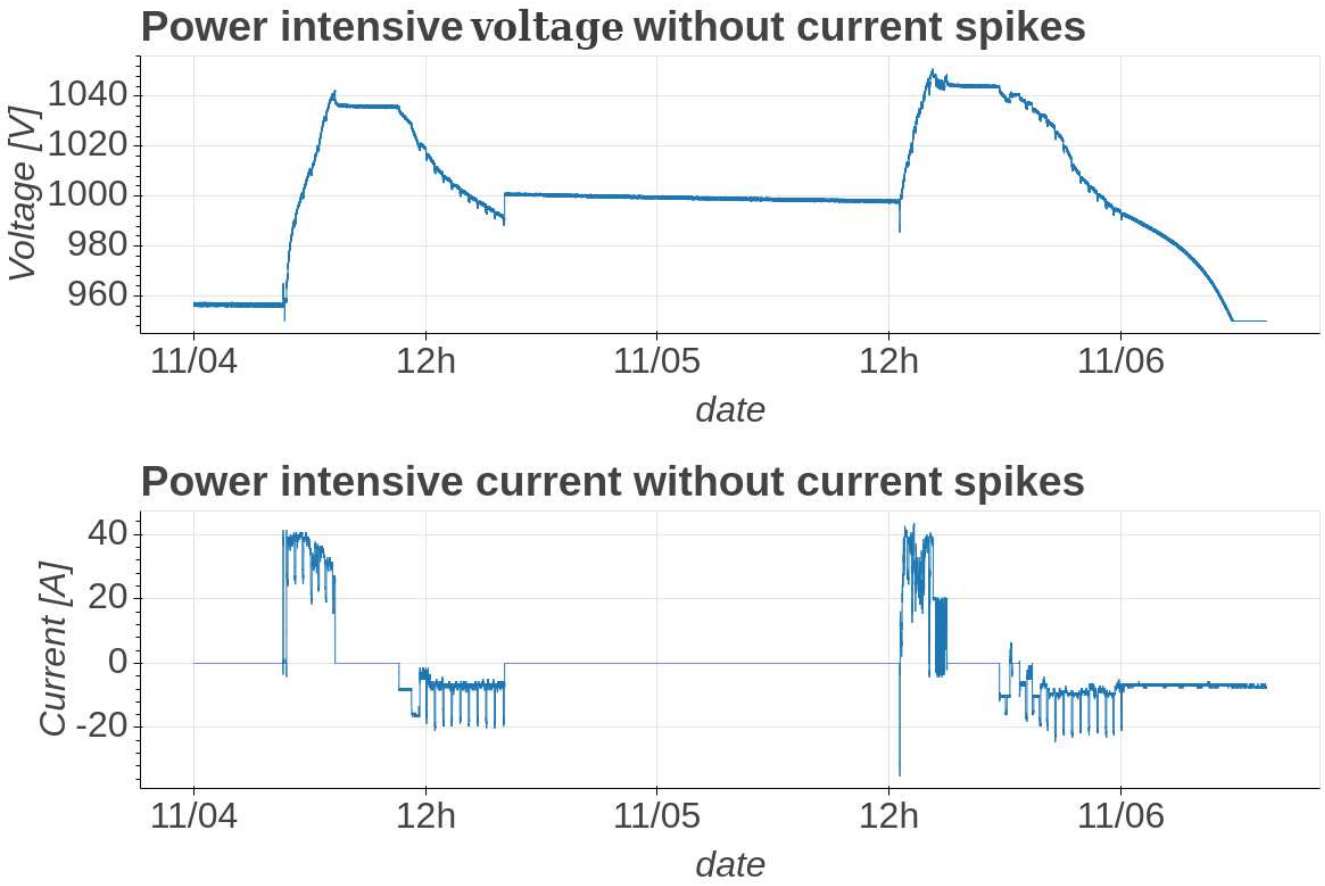

Figure 2.21: Example of BESS3 operating profiles mostly characterised by a power intensive behaviour. Current spike are not so frequent, rather current profiles present a similar step shape; thus, V_{OC} is estimated using DTW, as described in section 2.4.3.

50% of nominal one in a short time interval, arbitrarily chosen up to 10 seconds. Figure 2.20 depicts a BESS profile characterised by numerous current spikes so defined, corresponding to a sudden increase of voltage and SOC. If such spikes are present, firstly resistance is estimated through equation 2.15 because V_{OC} variation in such short time is considered negligible.

$$R = \frac{\Delta V}{\Delta I} \tag{2.15}$$

where ΔI is the spike current and ΔV is computed on related voltage values in the interval. The value of resistance estimated is averaged over the last ten values and updated each current spike. Figure 2.22 shows resistance estimated by this approach. It's notable that estimated resistance tends to increase throughout the battery cycling life, due to aging effect.

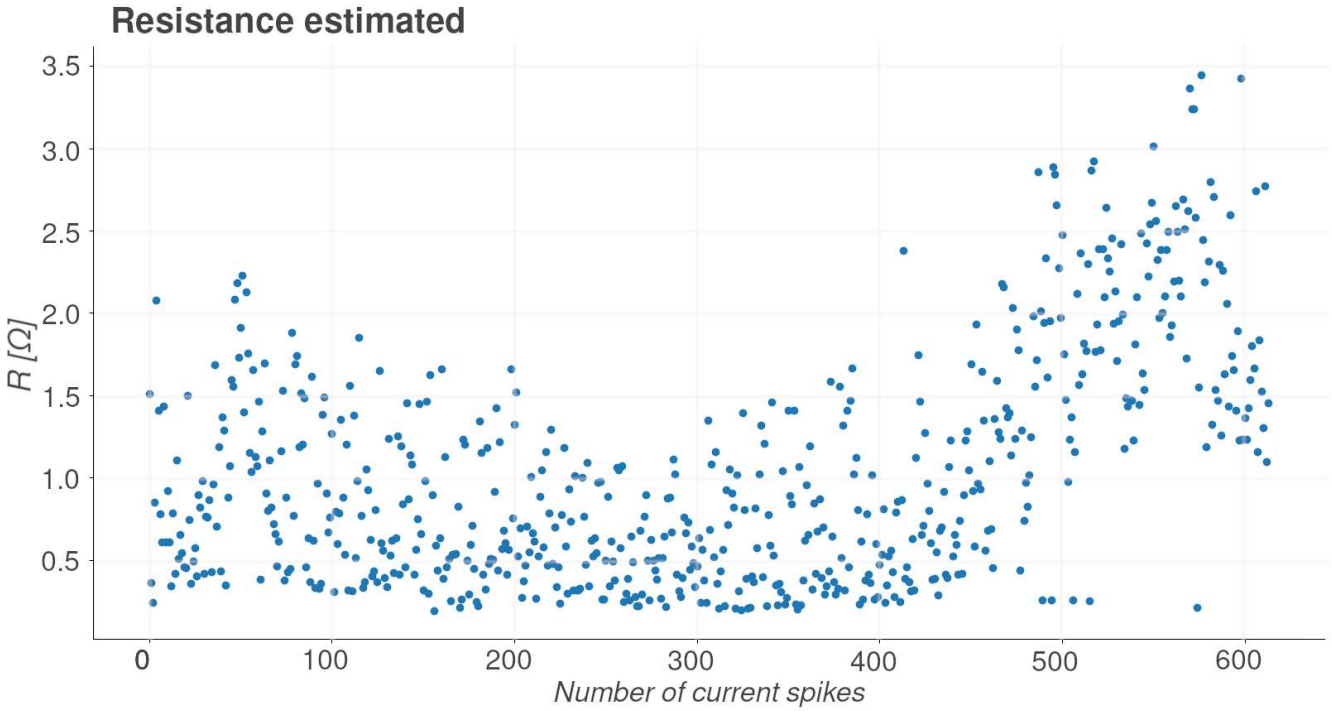

Figure 2.22: Resistance estimated (not averaged) on current spike. On x-axis current spikes are ordered chronologically.

Once the resistance is estimated, for each value V_{OC} is computed from zero-order model as defined in equation 2.16.

$$V_{OC}(t) = V(t) - R_{estimated}(t)I(t) \tag{2.16}$$

Finally, capacity at specific instant is computed as amount of current in charge/discharge profiles in a fixed range of ΔV_{OC} and averaged over 20 cycles, similarly to energy intensive procedure. Thus, $SOH(t)$ is defined as follows:

$$SOH(t) = \frac{C_{\Delta V_{OC}}(t)}{C_{\Delta V_{OC}0}} \tag{2.17}$$

Figure 2.23 reports decreasing SOH due to aging for our case study using V_{OC} estimation

on current spikes.

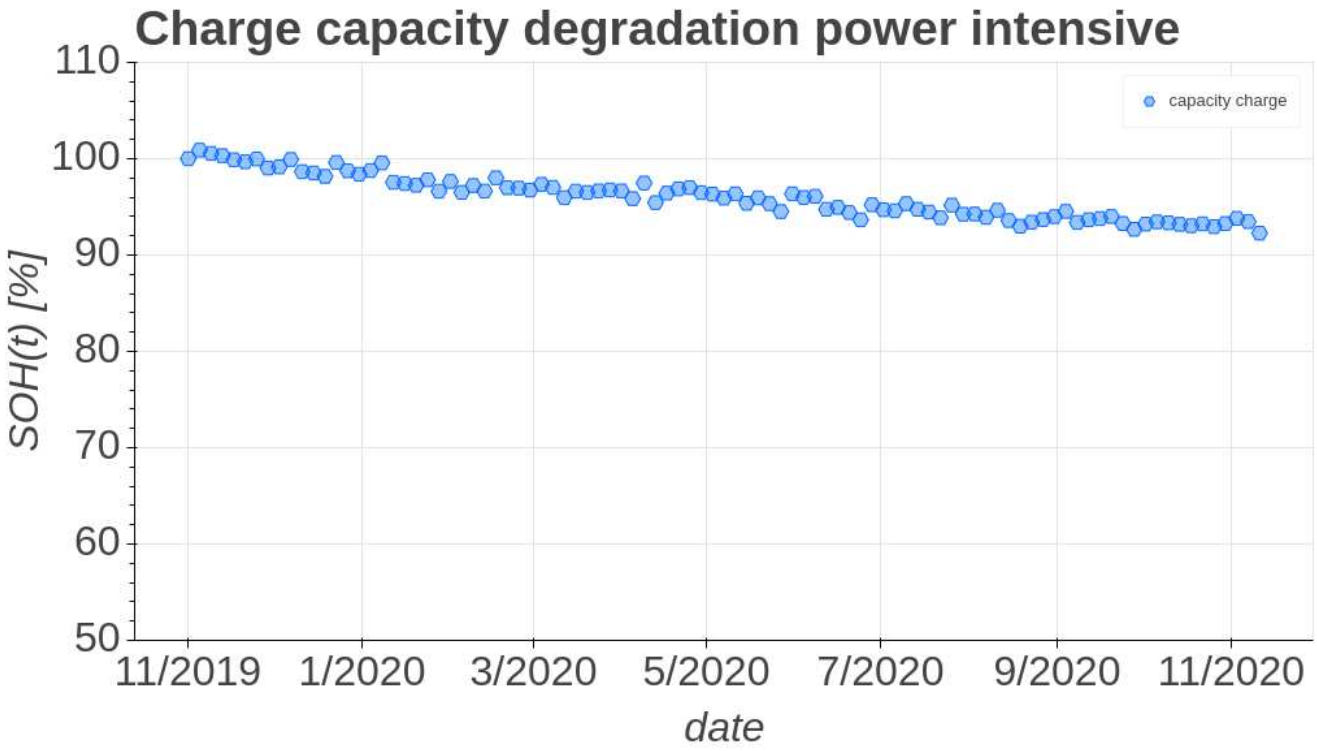

Figure 2.23: Capacity degradation in the case of power intensive usage, each capacity point is averaged over 20 cycles. Capacity is computed as current injected or extracted at fixed bin of V_{OC}.

Figure 2.21 shows power intensive profiles, where current mostly presents behaviour similar to a square wave with not so frequent sudden current peaks. Whether current spikes are not present or not numerous V_{OC} is estimated using zero order model on charge/discharge profiles of ΔSOC of about 4-5%. In this window, resistance is assessed as in equation 2.15 and then V_{OC} is computed. After V_{OC} estimation, operating profiles are divided in bin of open circuit voltage and dynamic time warping (DTW) [105] is applied to energy and power profiles group together similar curves and behaviour. It indeed aligns and computes distance between two time series through non-linear distortion. Grouped of similar power and energy curves are shown in figure 2.24.

In the most populated group of similar curves, $SOH(t)$ is computed as described in equation 2.17. Figure 2.25 reports decreasing SOH due to aging for the last case study using V_{OC} estimation and DTW on power and energy profiles.

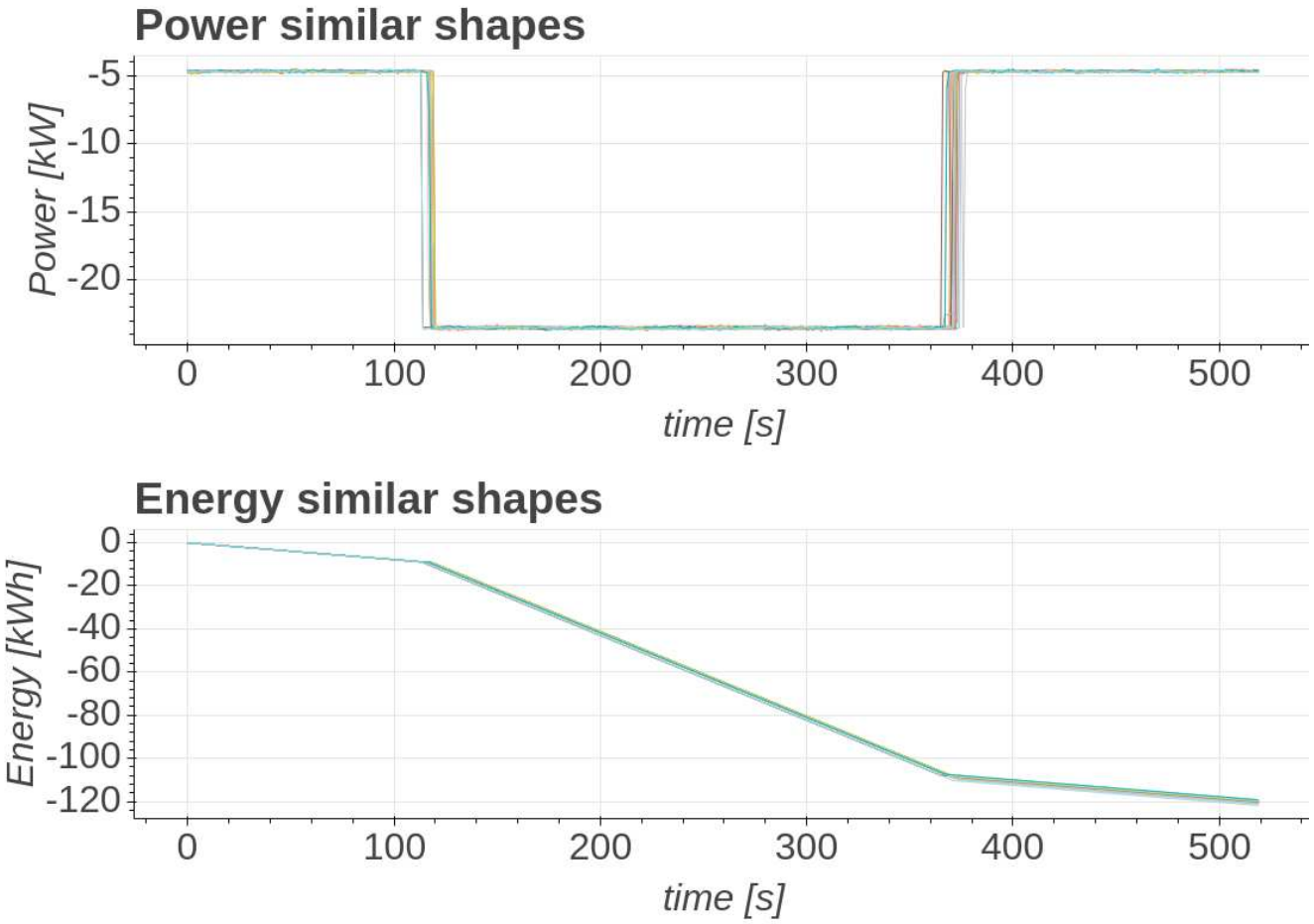

Figure 2.24: Similar operating profiles. Dynamic time warping is computed contemporaneously on both power and energy profiles. For each bin of V_{OC} DTW similarity is computed for shape of energy released or absorbed and power supplied or required.

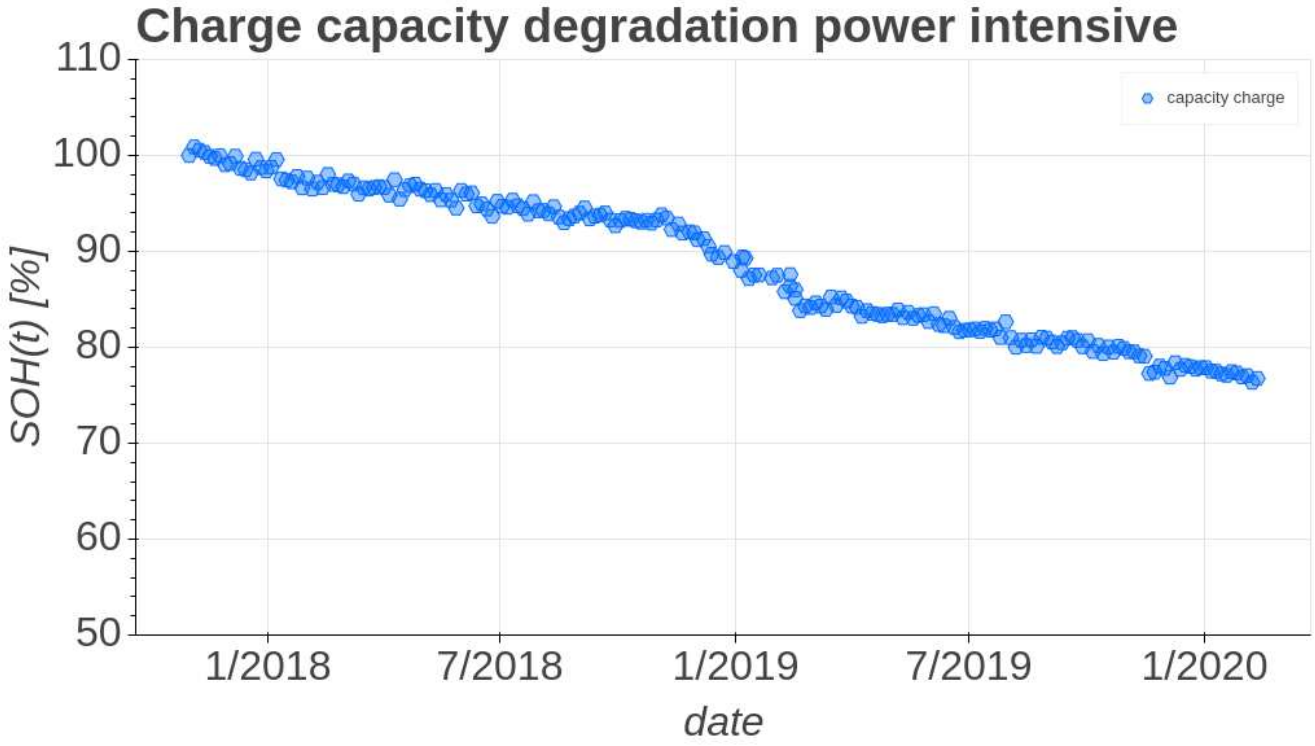

Figure 2.25: Capacity degradation in the case of power intensive usage, each capacity point is averaged over 20 cycles. Capacity is computed as current injected or extracted in group of similar profiles defined by means of DTW.

Chapter 3

Electric Vehicles

3.1 Overview

The performance of Energy Management Systems (EMSs) for Electric Vehicles (EVs) and Hybrid Electric Vehicles (HEVs) are highly dependent on the forecast of future driver torque/power request sequence that affects vehicle efficiency and economy. Since it is hard to model/predict the behaviour of the driver by first-principles models, modern data-driven Machine Learning (ML) and Artificial Intelligence (AI) algorithms would represent feasible methods for approaching this problem in real-world automotive systems.

3.2 State of the art

Driving cycle pattern prediction consists in forecast of aggregated features of the whole cycle segment, leading to an approximate knowledge of next route characteristics. In [106] driving cycles have been clustered in six different groups by means of a k-Shape algorithm, a technique that employs a shape-based distance as clustering metric. Then each driving series has been divided into several shorter segments on which features such as maximum velocity, average velocity, minimum acceleration, maximum acceleration and maximum deceleration have been computed. All this information has been used as input of a convolutional neural network (CNN) to predict the type of driving cycle. Niu et al. [107] have combined two neural networks to predict both driving trends and standard driving cycle with a time horizon of 1s. Driving trends have been grouped in a set of 5 possible types, whereas standard driving cycles in a set of 11. Features used in both neural networks have been built on data related to velocity, acceleration and time spent at specific velocity. Authors aimed to develop a fuzzy-based controller to manage energy consumption. Furthermore, the use of Learning Vector Quantization neural network (LVQNN) has been exploited to recognise real-time driving patterns and improve velocity prediction in [108].

Driving cycle pattern could be considered for EMS integration and optimization, but their use within mentioned EMS frameworks would be limited due to the hard customization required to exploit this information. On the other side, velocity predictors have been widely studied due to the possibility to directly exploit vehicle speed prediction within EMSs for achieving superior H/EV performance. Due to the stochastic nature of driving profile variation many studies have employed bayesian network and markov process in their predictive algorithm. Zhang et al. [109] developed an algorithm to predict velocity based upon a Bayes Network model that uses information about driving characteristics of succeeding vehicles, Geographic Information System (GIS) and Global Positioning System (GPS) data. Several studies have employed Markov processes, another kind of stochastic process, as in [108] mentioned before. In [110], a Discrete Markov process has been built

on velocity and acceleration: similar values of velocity and acceleration compose a state of transition matrix, representing similar driving conditions. Then, combining the Markov chain and Monte Carlo theory, an adaptive-horizon prediction method has been proposed and used to anticipate future moments. Furthermore, the combination of Markov process with backpropagation neural network (BPNN) has been explored [111]. A vehicle speed prediction has been advanced using both approaches to predict velocity in a horizon of 5s. Acceleration and velocity based features have been used for prediction. Another study [112] has involved velocity and acceleration data from highways and urban driving cycles and has compared forecasting results obtained by a Markov chain predictor, by an exponential-based predictive model and with outcomes from three types of neural networks (NNs): a BPNN, a layer recurrent (LRNN) and a radial basis function (RBFNN) neural networks. Thus, NNs based models have widely been employed to predict velocity are NNs, as reported before [111] [112]. Moreover, Rezaei et al. [113] have employed an autoregressive model to predict the desired drivers velocity at 10-seconds horizon. Data from three driving cycles have been used and GPS and GIS data have been involved in the predictive model to improve forecasting depending on upcoming events.

The principal drawback of speed prediction models is that velocity does not exactly reflect the drivers guide style because it depends on torque demanded by driver, which instead represents directly driver's reaction. Furthermore, desired velocity contains intrinsic delay in its information about the driver's will, i.e. engine time response and time elapsed to reach wanted velocity. The main approaches explored in literature for torque prediction have been neural networks, stochastic processes, autoregressive modeling and support vector machine (SVM). In [114] a three layer NN has been used to predict torque demand and vehicle velocity at 2.5 s horizon. Six drive cycles data have been recorded from a vehicle driven by the same driver at different days. Five driving cycles have been used for training and the other one for testing. In the study conducted by Zeng et al. [115], a single-hidden layer feedforward neural network (SLFN) has been presented to predict gasoline engine output torque with high accuracy but using as input features computed on engine characteristics such as engine speed, intake manifold pressure, barometric pressure, intake air rather than driving profiles. Also stochastic approaches have been employed to predict torque demand. Shi et al. [116] have used a one-step markov chain model for a MPC model with a time horizon of 1 second. Positive driving torque have been discretised between the maximum and minimum values to create transition probability map based on two real drive cycles and CTBCDC (China Transit Bus City Driving Cycle) profile. In [117], a fixed gain algorithm method has been developed for an online, multi-step and real-time prediction for the demanding power of an electro-mechanical transmission based on an autoregressive model with external inputs. Both desired power demand of the vehicle and actual power demand have been used as input. The prediction horizon has been set at 0.3 s. Meng et al.[118] have applied an autoregressive model for torque demand prediction as well. Simulated data have been generated with 0.01s sampling interval and 10 steps has been set as horizon prediction; features have been computed by means of torque and Vehicle-to-vehicle (V2V) information, such as distance, speed and acceleration. In [119] a second order polynomial regression and second order Volterra model have been compared for torque forecasting, using as input engine velocity and accelerator pedal. Dataset used have been collected from 300 samples of real vehicle data and prediction step has been set at 1. As last, a different approach has been proposed by Vong et al. [120], using a Least Squares SVM (LS-SVM) based on engine characteristics. 200 different engine setups has been acquired from a Honda B16A DOHC to predict output

torque.

3.3 Driver torque demand prediction

A comparative study of different strategies for torque prediction requested by the driver for the optimal EMS of H/EVs is conducted. Exponentially varying torque predictor, linear regression, shallow and deep NN and LS-SVM based strategies have been considered [121, 122]. The choice fell on the above classes since they allow developing multiple-input and multiple-output (MIMO) models and direct models for accurate long-term prediction. MIMO and direct models permit to obtain better results in terms of accuracy forecasting with respect to iterative one-step-ahead models [123]. Mentioned predictors are systematically compared in terms of prediction capability and computational cost. The considered methods belong to the supervised learning class, as they use stored data for training off-line a data-driven estimation policy to be used on-line for providing required torque sequence.

In this study, two additional original contributions are included with respect to the related literature. First, extensively analysis of data-driven based torque demand predictors are conducted, for the first time, for HEV energy management. Second, the LS-SVM based torque predictor is investigated to fully explore its potential in the model adaptation when the driving style changes over-time.

3.3.1 Exponential predictor

Exponential torque demand predictor assumes that power request increases/decreases exponentially over the prediction horizon. In each prediction horizon, the exponentially varying horizon torque is formulated as stated in equation 3.1:

$$T_{k+n} = T_k \cdot (1+\epsilon)^n, \quad n = 1, 2, \ldots, p \tag{3.1}$$

where p is the prediction horizon, T_k is the initial torque at time step k and ϵ is the exponential coefficient. Different ϵ values are considered to examine the sensitivity of model. The model proposed in literature was considered for its ease of developing in a real-time application [112].

3.3.2 Multivariate linear regression

Multivariate linear regression (MLR) considers the following model:

$$y_k = W^T x_k + e_k \tag{3.2}$$

where $k \in \mathbb{Z}$ is the discrete time index, y_k is the l-dimensional vector of responses, x_k is a design m-dimensional vector of predictor variables, $W \in \mathbb{R}^{m \times l}$ is the matrix of regression coefficients and $e_k \sim \mathcal{N}(0, \Sigma)$ is the l-dimensional vector of error terms, with multivariate normal distribution. The prediction is performed as $\hat{y}_k = W^T x_k$ The matrix W of regression coefficients is found by the ECM algorithm [124]. The MLR model is considered for its ease of developing in a real-time application and for its capability to learn models, one for each horizon, from the time series.

3.3.3 Cascade Neural Network

Cascade-forward neural network is a class of neural network similar to feed-forward networks, but it includes a connection from the input and every previous layer to following layers. It corresponds to the case where all previous hidden units are used as regressors in the next layer, not only the ones from the previous layer. The advantage of this network is that it accommodates the nonlinear relationship between input and output by not eliminating the linear relationship between the two layers. In [125], the authors showed as a deep learning model with six layers of cascaded-forward nets gives better results in the validation dataset with respect to deeper LSTM models. The authors highlighted as the cascade-forward neural network obtains models for the standard Silverbox benchmark case [126] that easily match the best results obtained with other sophisticated solutions [127], so, lastly, the cascade-forward neural network is considered in this work as regression model for driver torque demand prediction. The figure 3.1 show the standard structure of a cascade-forward neural network. Cascade neural network is considered for its capability to learn MIMO models and to obtain

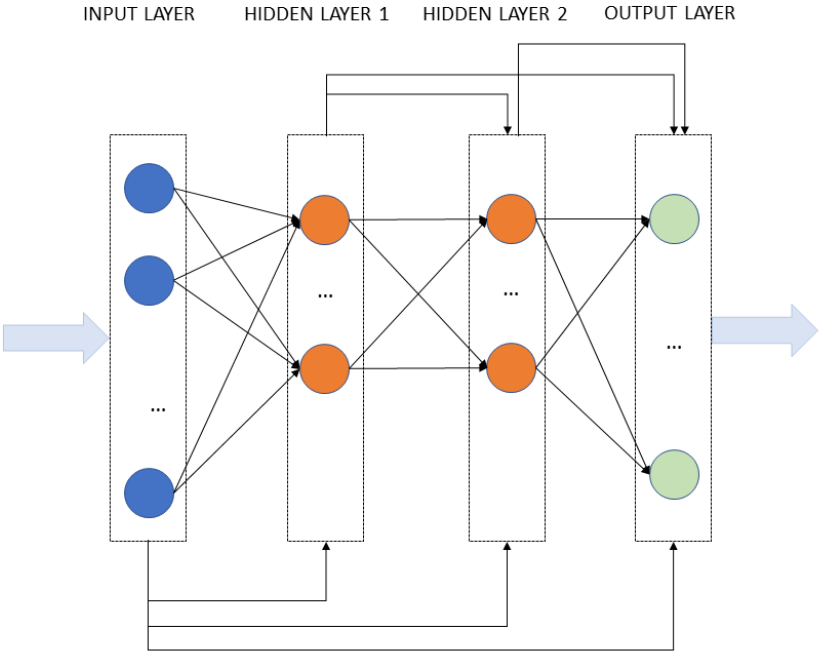

Figure 3.1: Cascade neural network.

models that easily match the best results obtained with other sophisticated solutions in different benchmarks [125].

3.3.4 Deep Neural Network

With the advancement of computational hardware resources and algorithms, deep learning methods such as the long short-term memory (LSTM) model and sequence-to-sequence (seq2seq) modeling have shown a good deal of promise in dealing with time series forecasting by considering long-term dependencies and multiple outputs [128]. This study presents a regression model based on LSTM and the seq2seq structure to predict the driver torque demand. An LSTM network is a type of recurrent neural network (RNN) used in the field of

deep learning that can learn long-term dependencies between time steps of sequence data and it is used for different tasks such as anomaly detection, speech recognition, and in the context of time series forecasting as well.

3.3.5 Least Square Support Vector Machine

LS-SVM is a variant of SVM that lead to solving linear Karush-Kuhn-Tucker (KKT) conditions. LS-SVM method considers the regression problem as the following optimization problem.

$$\min_{w;e;b} J(w;e) = \frac{1}{2}w^T w + \frac{1}{2}\gamma \sum_{i=1}^{n} e_i^2 \tag{3.3}$$

$$\text{subject to} \quad y_i = w^T \phi(x_i) + b + e_i, \quad i = 1, \ldots, n \tag{3.4}$$

where $w, b \in \mathbb{R}$, γ is a regularization constant, $\phi(x_i)$ is the feature map to the high dimensional future space and e_i denotes the prediction error term for the i-th data point. The Lagrangian function is

$$L(w;b;e;\alpha) = J(w;b) + \sum_{i=1}^{n} \alpha_i \left(y_i - w^T \phi(x_i) - b - e_i \right) \tag{3.5}$$

where α_i are the Lagrange multipliers. So by using Lagrange multipliers, the solution can be obtained by considering the Karush-Kuhn-Tucker (KKT) conditions for optimality and solve the dual problem.

$$\frac{\partial L}{\partial w} = 0 \rightarrow w = \sum_{i=1}^{n} \alpha_i \phi(x_i) \tag{3.6}$$

$$\frac{\partial L}{\partial b} = 0 \rightarrow \sum_{i=1}^{n} \alpha_i = 0 \tag{3.7}$$

$$\frac{\partial L}{\partial e_i} = 0 \rightarrow e_i = \frac{\alpha_i}{\gamma} \tag{3.8}$$

$$\frac{\partial L}{\partial \alpha_i} = 0 \rightarrow y_i = w^T \phi(x_i) + b + e_i \tag{3.9}$$

So the standard framework for LS-SVM is based on a primal-dual formulation and the solution in α, b is given by the following linear system

$$\left[\begin{array}{c|c} \Omega + I/\gamma & 1_n^T \\ \hline 1_n & 0 \end{array}\right] \left[\begin{array}{c} \alpha \\ \hline b \end{array}\right] = \left[\begin{array}{c} Y \\ \hline 0 \end{array}\right], \tag{3.10}$$

with $Y = [y_1, \ldots, y_n]$, $\alpha = [\alpha_1, \ldots, \alpha_n]$, $1_n = [1, \ldots, 1]$, $\Omega_{ij} = \phi(x_i)^T \phi(x_j) = K(x_i, x_j)$ and with $K(x_i, x_j)$ a positive definite kernel. The previous linear system can be rearranged as

$$\Theta_n \hat{\alpha}_n = Y_n \tag{3.11}$$

where $\hat{\alpha}_n = [\alpha, b]^T$, $Y_n = [Y, 0]^T$ and the Lagrangian multiplier can be estimated by inverting the matrix Θ_n. According to Mercer's theorem, the resulting LS-SVM model for function estimation becomes $\hat{y}(x) = \sum_{i=1}^{n} \alpha_i K(x, x_i) + b$.

When working with large data sets it is important to emphasize that the use of the entire training sample of size n to compute kernel matrix and the solution of (3.10) can be

prohibitive. So in [129, 130], the authors proposed an explicit approximation for the feature map ϕ when working in the primal space. The method is based on the Nyström method [131] that determines an approximation of ϕ. This finite dimensional approximation $\hat{\phi}(x)$ can be used in the primal problem to estimate w, b. In particular, the authors provided an algorithm for making a good selection of the support vectors and a methodology to choose a working set of fixed size $m \ll n$. In order to make a more suitable selection of the support vectors instead of a random selection, one can relate the Nyström method to kernel principal component analysis, density estimation and entropy criteria. The m support vectors which maximize the quadratic Rényis entropy that can be approximated by using

$$\int \hat{p}(x)^2 dx = \frac{1}{N^2} 1_n^T \Omega 1_n \tag{3.12}$$

One chooses a fixed size m then and actively selects points from the pool of training data as candidate support vectors. An algorithm that select the points from the training data set that iteratively improves the entropy criterion was proposed in [129, 130] and considered in this study. Fixed-size LS-SVM model is considered for its capability to handle large data sets and to learn models, one for each horizon, from the time series [130].

3.4 Results

Results are compared between performance of baseline supervised learning approaches and the proposed policy based on the model updating.

Popular certification cycles are the outdated New European Driving Cycle (NEDC) which was replaced by the World-harmonized Light-duty Test Cycle (WLTC) and the World-harmonized Light-duty Test Procedure (WLTP) for Europes certification test procedure starting in 2017. Driving cycles considered in this study are the NEDC, the WLTP (class 1, 2, and 3 termed as WLTP1, WLTP2, WLTP3, respectively), the FTP-75 and the US06. Three different WLTC have been defined, depending on vehicle class defined, i.e., class 1- low power vehicles, class 2- medium power vehicles and class 3- high-power vehicles. The EPA Federal Test Procedure is a series of tests defined by the US Environmental Protection Agency. The current procedure has been updated in 2008 and includes four tests, in this study the city driving test (FTP-75), and the aggressive driving test (US06) are considered.

Signals analyzed for the prediction of driver torque demand are torque, acceleration, velocity, and engaged gear sequences. To generate such a signal, the Mathworks MATLAB/Simulink HEV P3 Reference Application simulation model as been considered. This model permits to simulate the behaviour of a realistic HEV featured by a hybrid powertrain with internal combustion engine, transmission, electric motor and battery, an EMS based on PMP, and a a nonlinear model of the driver computing the torque reference signal that permits to track the vehicle speed reference signal defined according to the selected driving cycle.

By running this model over the set of selected driving cycles, required signals have been collected. Algorithms evaluated in the following sections have been developed by considering as input the last 10 samples of driver demanded torque signal, the last 5 samples of vehicle speed and acceleration, and the last gear control signal sample. The size of such a input signal represent the size of the buffer iteratively updated at each sampling time with the last measured signals' value. The size of each delay buffer represent the memory of the algorithm and has been established empirically such that longer delays don't improve significantly the obtained performances in this specific experimentation. The sampling time T_s is 0.1 s and

the prediction horizon is 20 steps ahead. The data was standardized in the range -1 to 1.

Achieved prediction results have been evaluated according to the Best Fit Rate (BFR) index, adjusted RMSE (aRMSE) and adjusted MAE (aMAE), computed as

$$\text{BFR} = 100 \times \max\left(0, 1 - \frac{\|y - \hat{y}\|_2}{\|y - \frac{1}{N}\sum_{k=1}^{N} y(k)\|_2}\right), \tag{3.13}$$

$$\text{aRMSE} = \frac{\left(\frac{1}{N}\sum_{k=1}^{N}\left(y(k) - \hat{y}(k)\right)^2\right)^{0.5}}{\max(y) - \min(y)}, \tag{3.14}$$

,

$$\text{aMAE} = \frac{\frac{1}{N}\sum_{k=1}^{N}\left(y(k) - \hat{y}(k)\right)}{\max(y) - \min(y)}. \tag{3.15}$$

where y and $\hat{y}$ are the real and the predicted torque, respectively, and $y(k)$ is the real torque at the time instance k.

The dataset has been divided in 50% for training and 50% for testing, a 10-fold strategy is applied to the training dataset to set the hyperparameters by using the Bayesian optimization algorithm. The procedure has been replicated 20 times and the results shown in this paragraph are the average value and standard deviation of the repetitions.

3.4.1 Baseline Predictor

The considered baseline predictor maintains constant the measured torque value at instant k to predict the value to the instants $k+1, \ldots, k+p$, where p is the prediction horizon. Figure 3.2 shows the indexes BFR, adjusted RMSE and adjusted MAE of the baseline, in which the driver torque prediction is basically considered constant from k to $k+p$. The figures 3.2a, 3.2b and 3.2c show that the worst cases that is the WLTP1 considering BFR and the US06 considering adjusted RMSE and adjusted MAE. The 1-step ahead prediction is quite adequate whereas the performance becomes worst for long-term prediction for some type of driving cycles.

3.4.2 Results of Exponential Predictor

The exponential predictor gives results very close to the baseline, as shown in Figure 3.3. The figures 3.3a, 3.3b and 3.3c show the BFR, adjusted RMSE and adjusted MAE of the exponential predictor. The parameter ϵ belongs to the set of values $[-0.1, -0.09, \ldots, 0.1]$. The average BFR, RMSE and MAR reach their minimum for each driving cycle when $\epsilon \in \{-0.03, -0.02, -0.01, 0\}$.

3.4.3 Multivariate Linear Regression based Predictor

Concerning multivariate linear regression, linear, second order and third order polynomial models are trained. The figures 3.4, 3.5, 3.6 show the indexes BFR, adjusted RMSE and adjusted MAE for the case MLR. In particular, the figures 3.4a, 3.4b, 3.4c show the indices for the linear model, the figures 3.5a, 3.5b, 3.5c show the indices for the second order polynomial model and as last the figures 3.6a, 3.6b, 3.6c show the indices for the third order polynomial

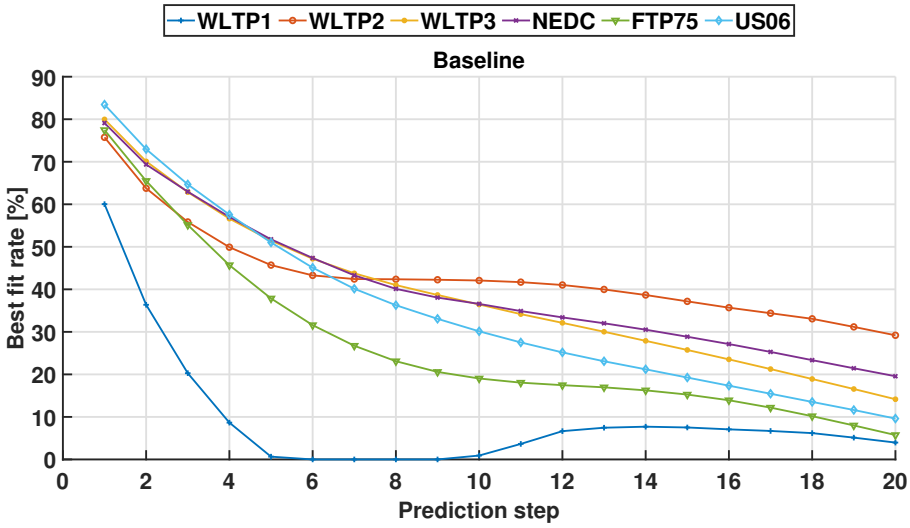

(a) BFR

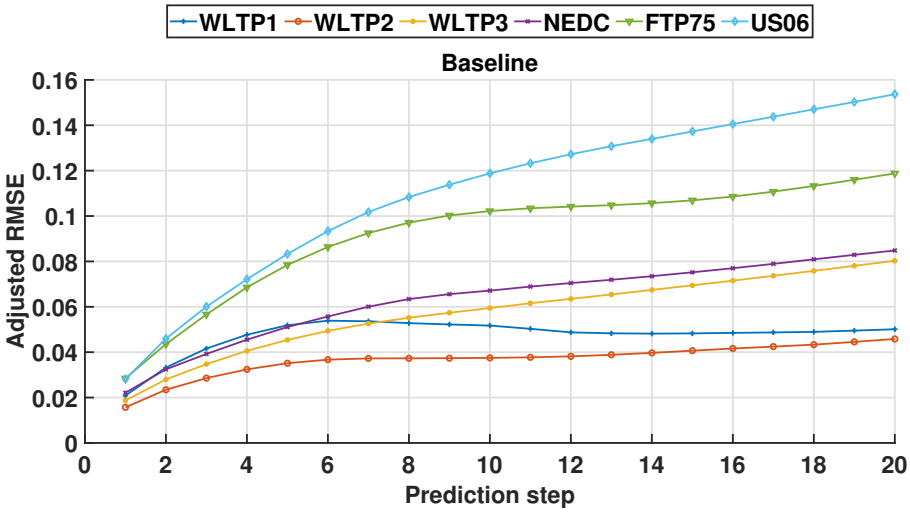

(b) Adjusted RMSE

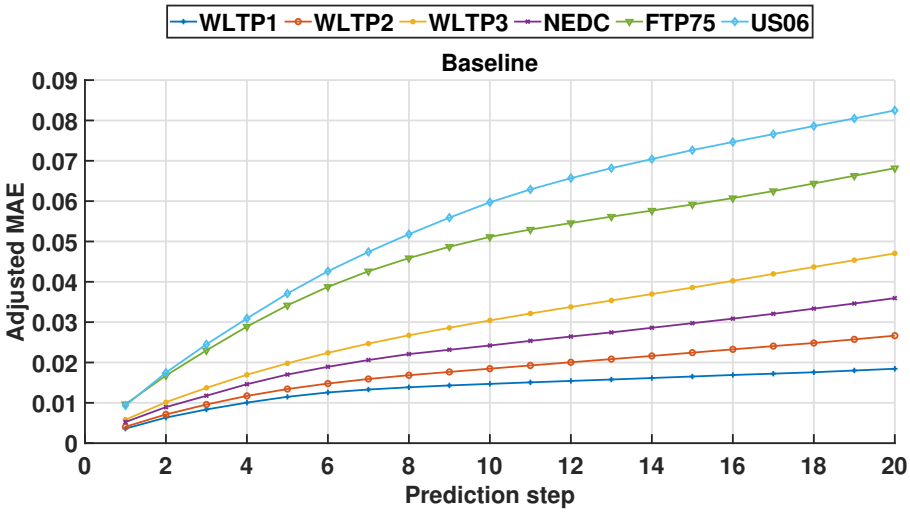

(c) Adjusted MAE

Figure 3.2: Baseline predictor performance

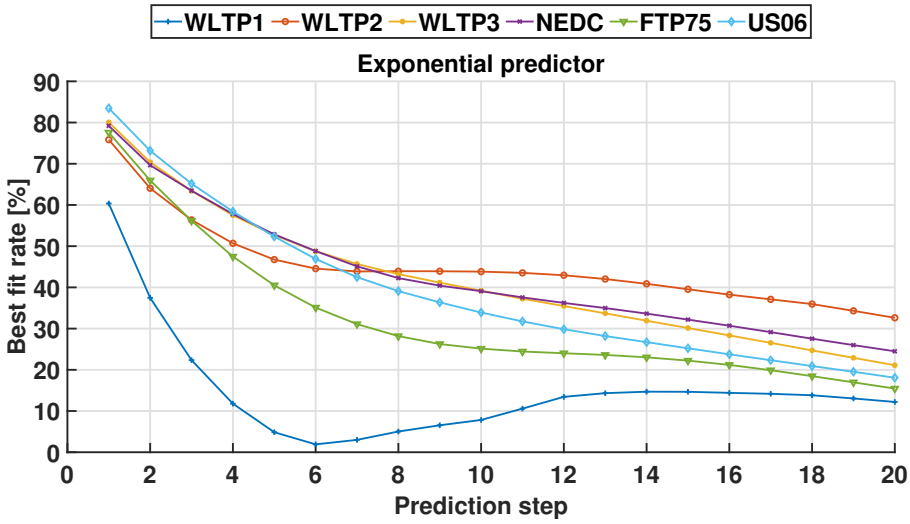

(a) BFR

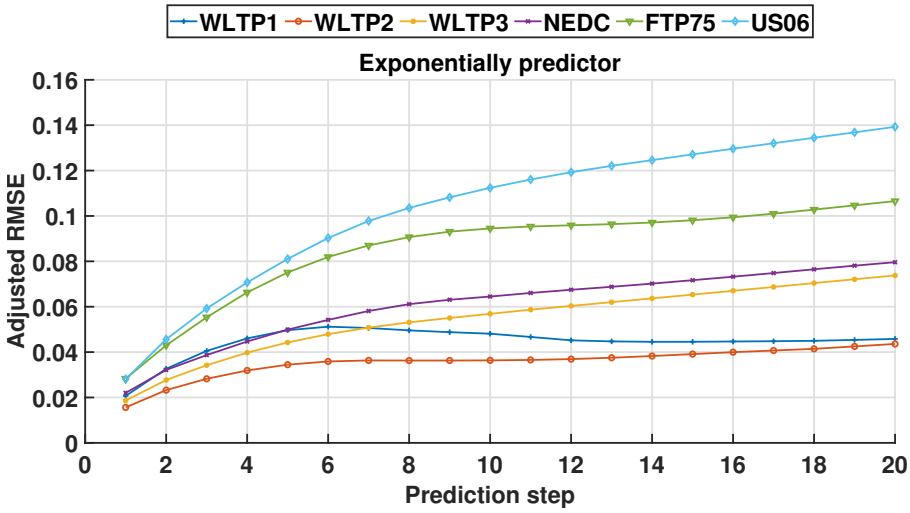

(b) Adjusted RMSE

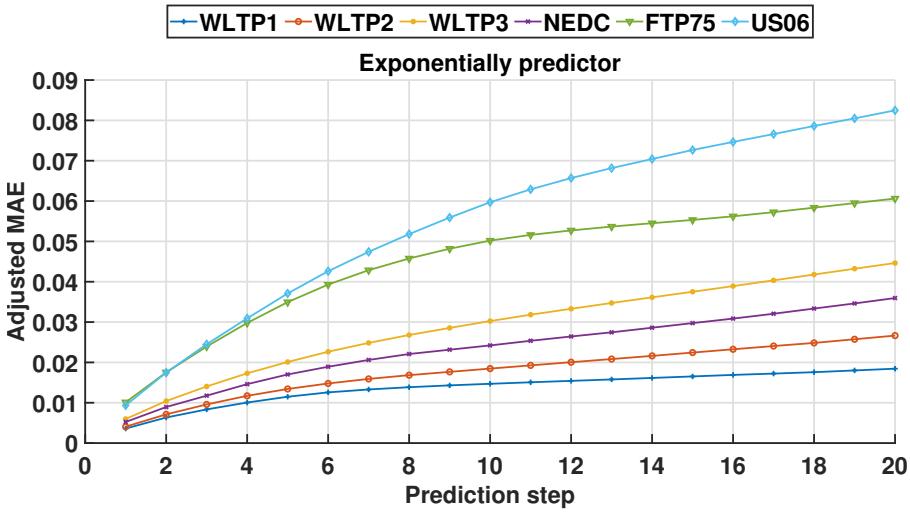

(c) Adjusted MAE

Figure 3.3: Exponential varying predictor performance

model. The BFR is best for the third-order model (i.e., 43 predictors), but the improvement with respect to the second-order (i.e., 64 predictors) is low despite a greater increase of the computational burden for model training, then a second-order polynomial model is preferable.

3.4.4 Cascade Neural Network based Predictor

Concerning cascade neural network, the figures 3.7, 3.8 shows the indexes BFR, adjusted RMSE and adjusted MAE. In particular, the figures 3.8a, 3.8b, 3.8c show the indices for the cascade neural network trained with Scaled Conjugate Gradient (SCG) training algorithm and the figures 3.7a, 3.7b, 3.7c show the indices for the cascade neural network trained with Levenberg-Marquardt (LM) algorithm. These training algorithms have been chosen due to their popularity and effectiveness for NNs [132]. After hyperparameters tuning, the optimal neural network is composed of three hidden layer with 20, 10 and 20 neurons, respectively. A regularization term of 0.01 is added to the training algorithm.

3.4.5 Sequence-to-Sequence Model based Predictor

Concerning deep neural network has been considered a structure composed of 6 layers in particular, an input layer, a LSTM layer of 500 neurons, a fully connected layer of 100 neurons, a dropout layer with probability 0.5, a fully connected layer of 20 neurons and a regression layer. The figure 3.9 shows the indexes BFR, adjusted RMSE and adjusted MAE. In particular, the figures 3.9a, 3.9b, 3.9c show the indices for the sequence-to-sequence regression model using LTSM model.

3.4.6 Fixed-Size LS-SVM based Predictor

Concerning least square support vector machine, standard and fixed size models are trained. The figures 3.10, 3.11, 3.12 show the indexes BFR, adjusted RMSE and adjusted MAE for the case LS-SVM. In particular, the figures 3.10a, 3.10b, 3.10c show the indices for the fixed size model with m=200 samples, the figures 3.11a, 3.11b, 3.11c show the indices for the fixed size model with m=500 samples and as last the figures 3.12a, 3.12b, 3.12c show the indices for the standard LS-SVM model.

3.4.7 Torque Demand Prediction Comparison

The Table 3.1 shows the results considering the mean and standard deviation of all simulations varying the driving cycle and a prediction horizon from 1 to 20 steps ahead. In the Table 3.1 is reported only the cascade neural network trained with Levenberg-Marquardt because the scaled conjugate gradient training algorithm gives worst results. The table showed as the exponential predictor gives results very close to the baseline. As can be seen from Table 3.1, the maximum average BFR and the minimum average RMSE and MAE are reached considering the Fixed-Size LS-SVM (m=500 samples). Cascade neural network showed similar average results to Fixed-Size LS-SVM but the standard deviations are higher. Multivariate linear regression showed worst results with respect to Fixed-Size LS-SVM and cascade neural network but the standard deviations are low. Finally, the sequence-to-sequence model based on LSTM showed the best outcomes among the machine learning based predictors.

Simulation was performed on a personal computer with an Intel Core i7-7700HQ CPU at 2.8 GHz CPU. Computational times required by each prediction algorithm are reported in Table 3.1 showing how Sequence-to-Sequence predictor is computationally heavier than CNN,

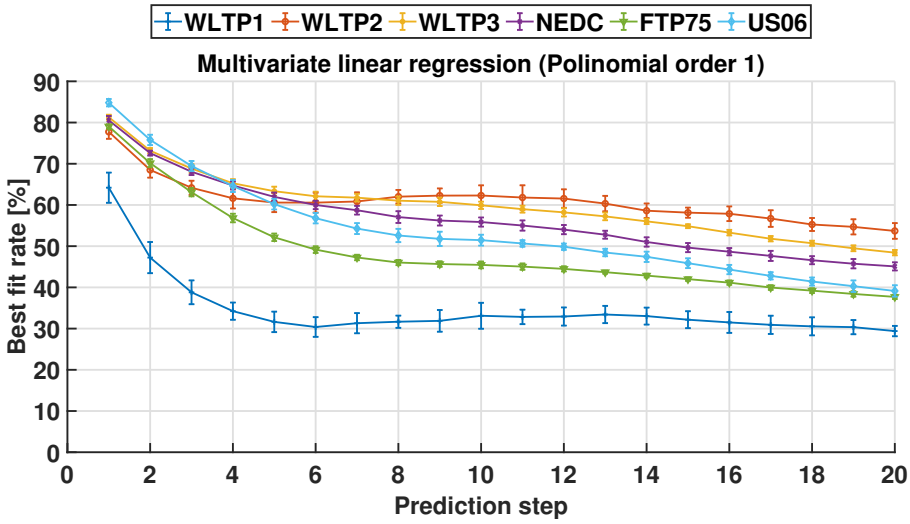

(a) 1st order, BFR

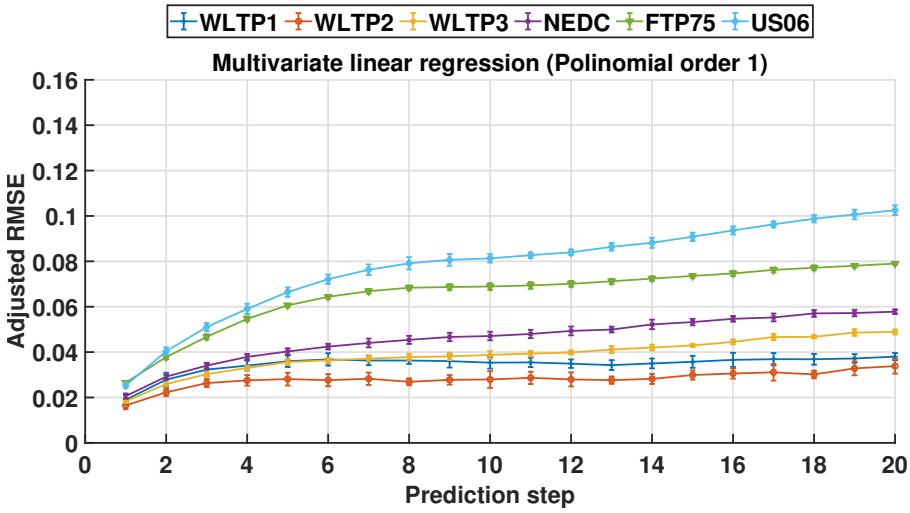

(b) 1st order, adjusted RMSE

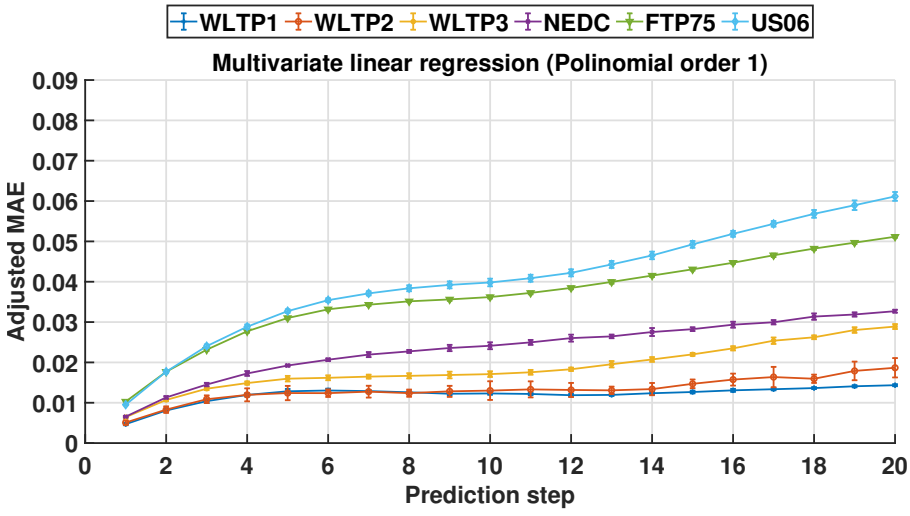

(c) 1st order, adjusted MAE

Figure 3.4: Multivariate linear regression: 1st order polynomial model.

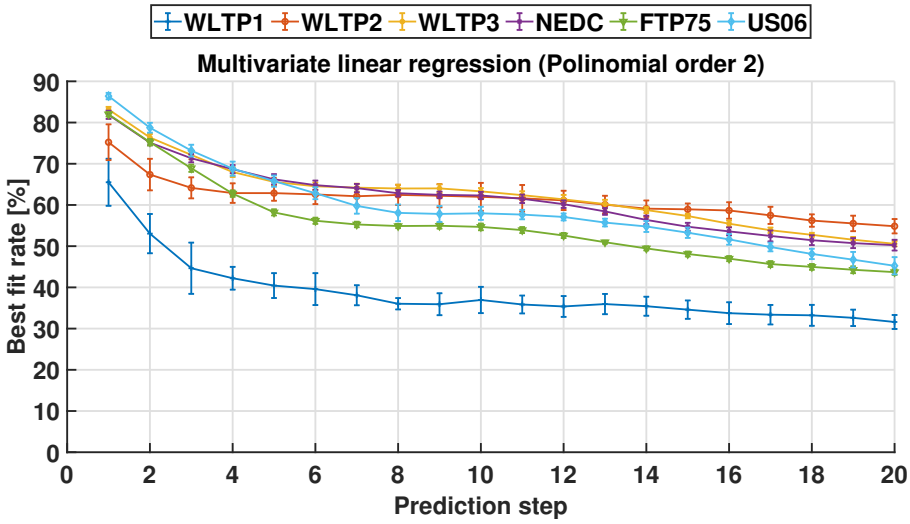

(a) 2nd order, BFR

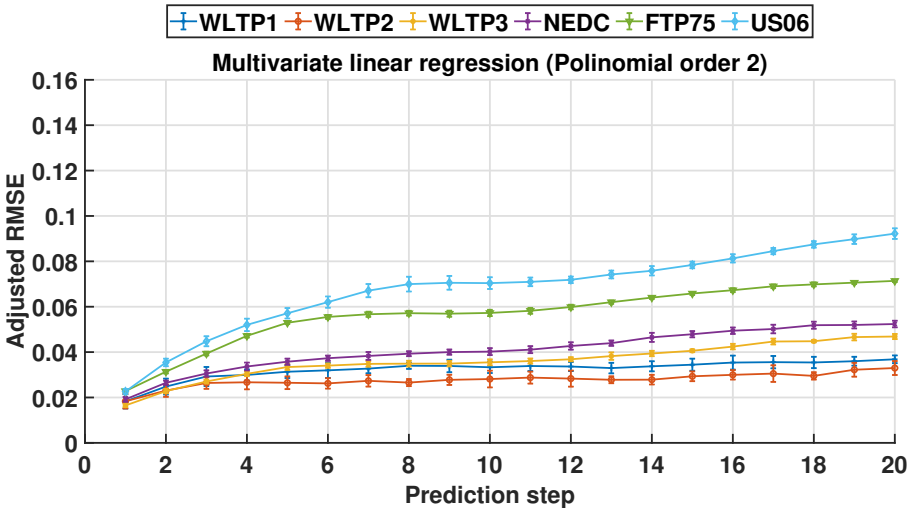

(b) 2nd order, adjusted RMSE

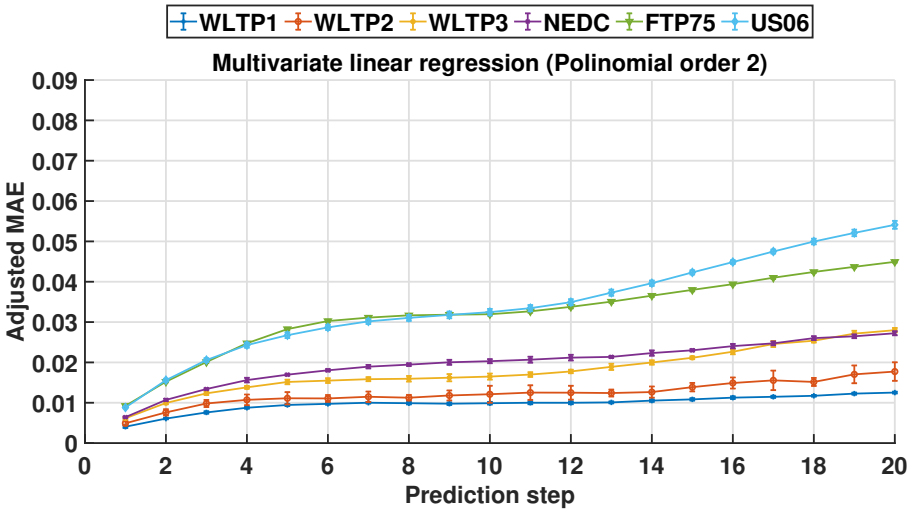

(c) 2nd order, adjusted MAE

Figure 3.5: Multivariate linear regression: 2nd order polynomial model.

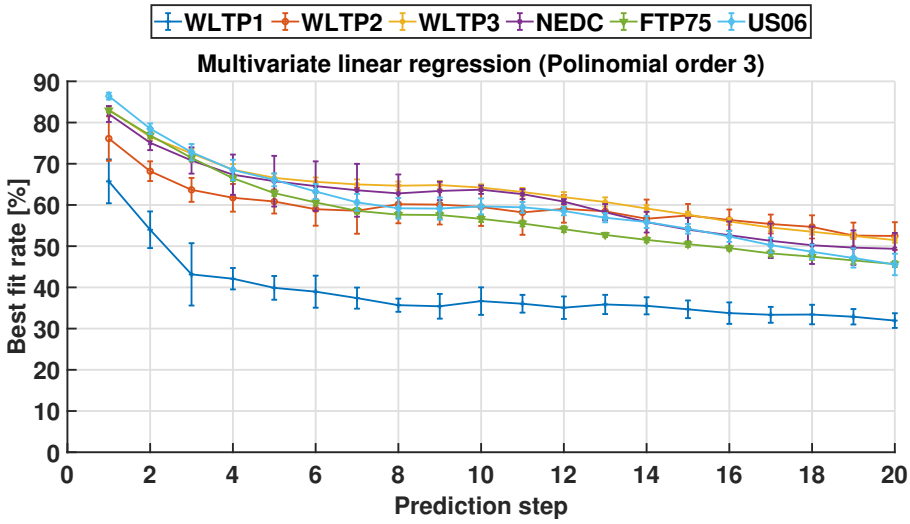

(a) 3rd order, BFR

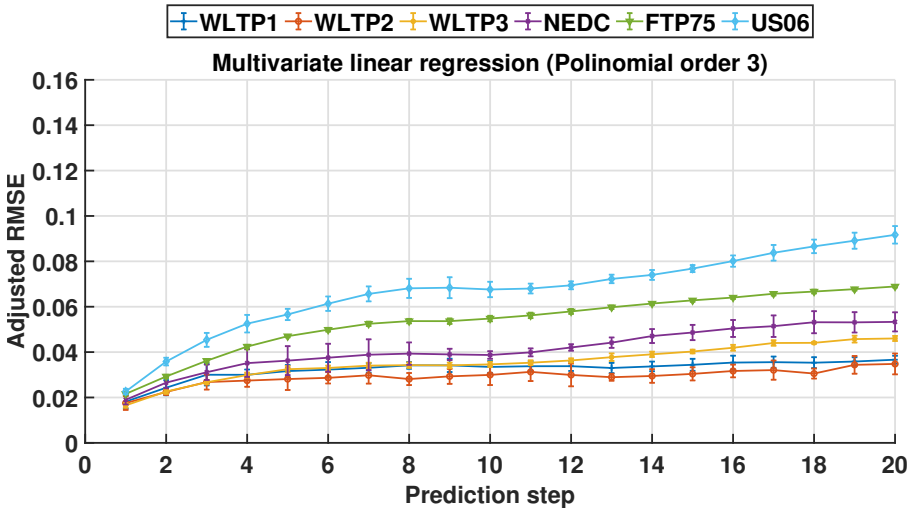

(b) 3rd order, adjusted RMSE

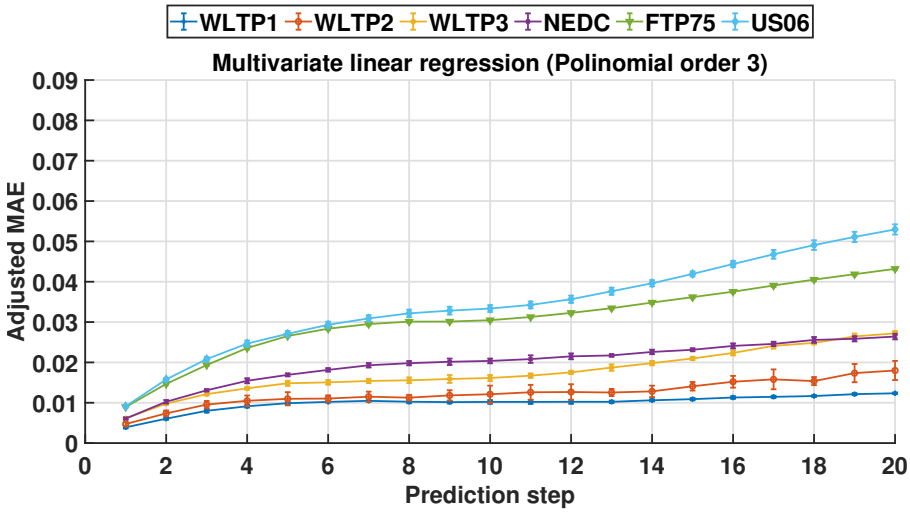

(c) 3rd order, adjusted MAE

Figure 3.6: Multivariate linear regression: 3rd order polynomial model.

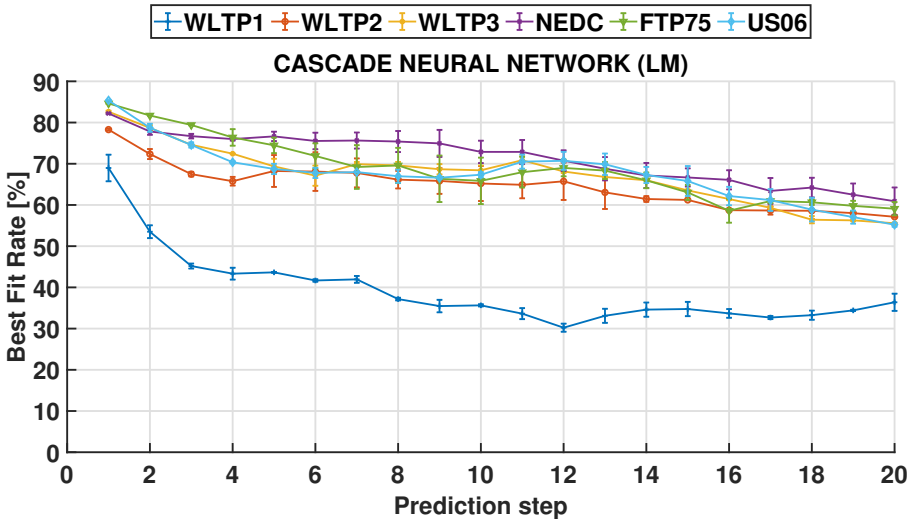

(a) Cascade NN (LM), BFR

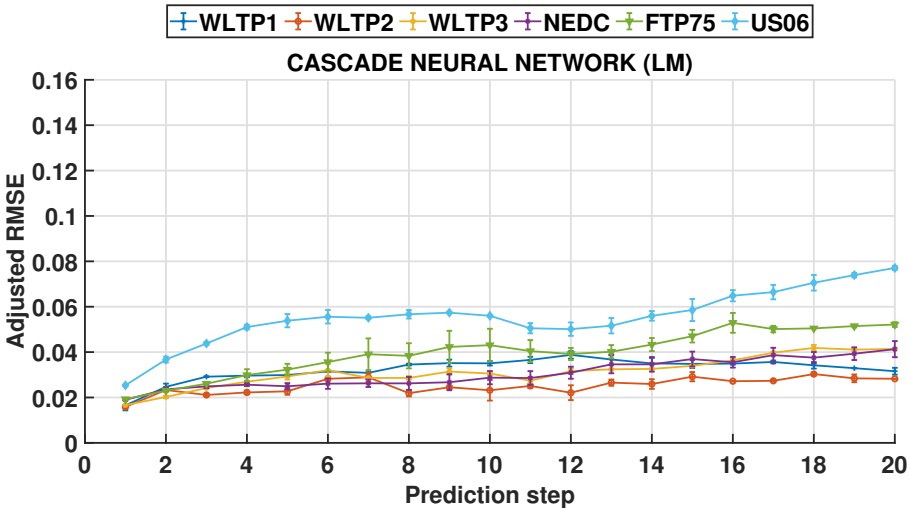

(b) Cascade NN (LM), adjusted RMSE

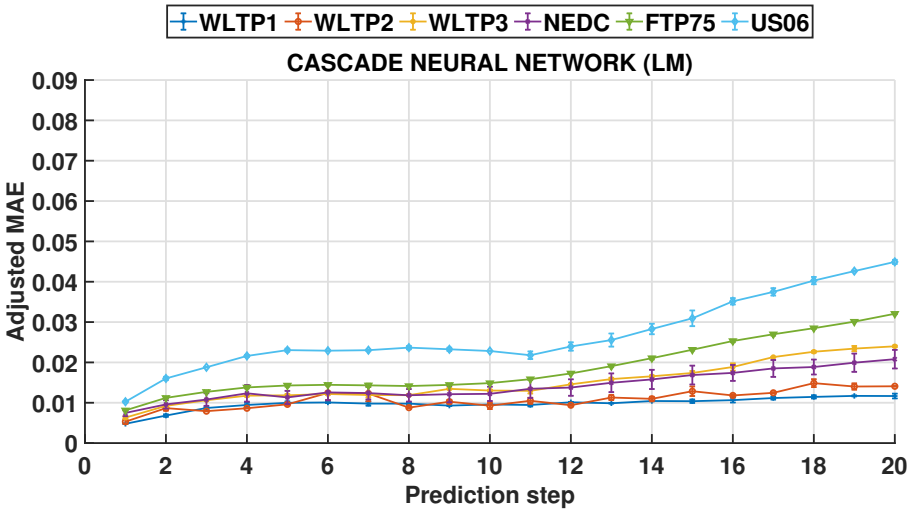

(c) Cascade NN (LM), adjusted MAE

Figure 3.7: Cascade neural network: cascade NN trained with LM training algorithm.

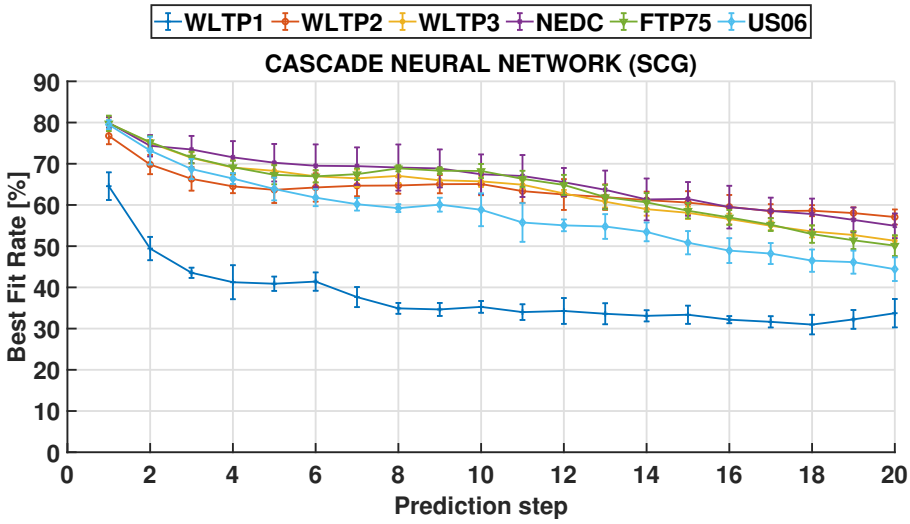

(a) Cascade NN (SCG), BFR

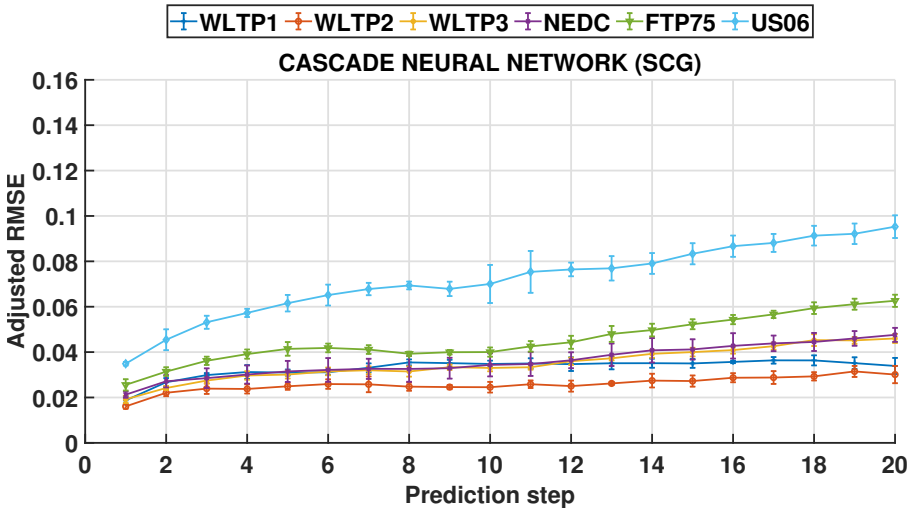

(b) Cascade NN (SCG), adjusted RMSE

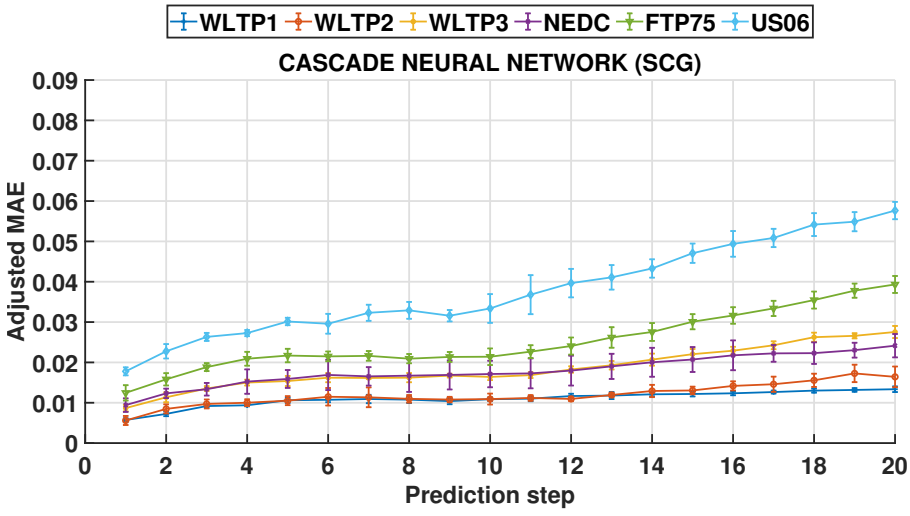

(c) Cascade NN (SCG), adjusted MAE

Figure 3.8: Cascade neural network: cascade NN trained with SCG training algorithm.

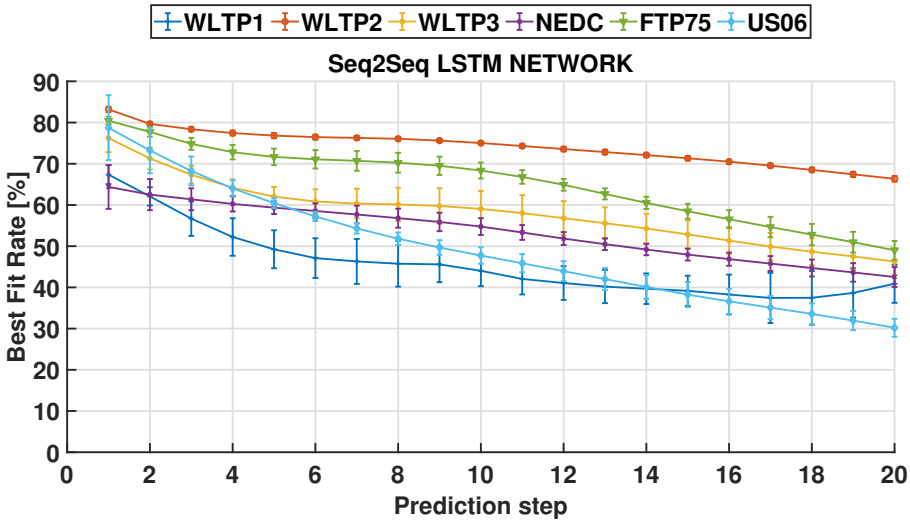

(a) Deep neural network (seq2seq), BFR

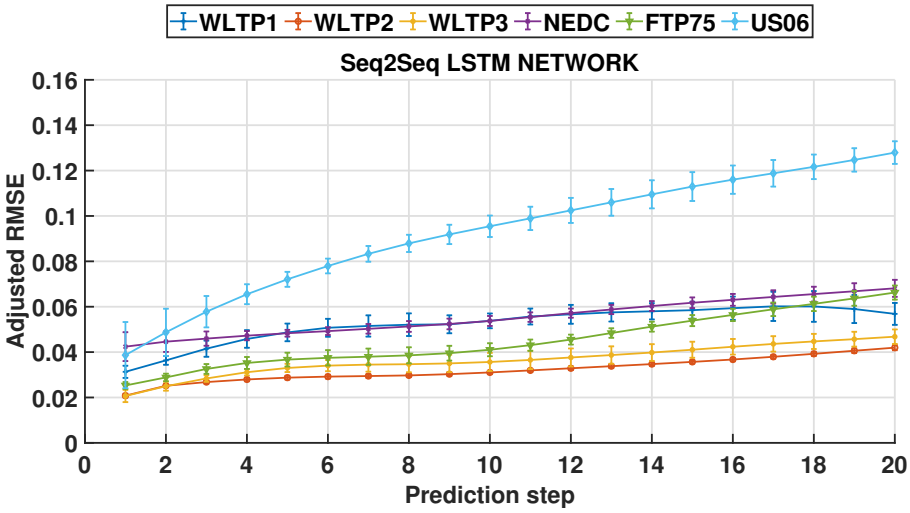

(b) Deep neural network (seq2seq), adjusted RMSE

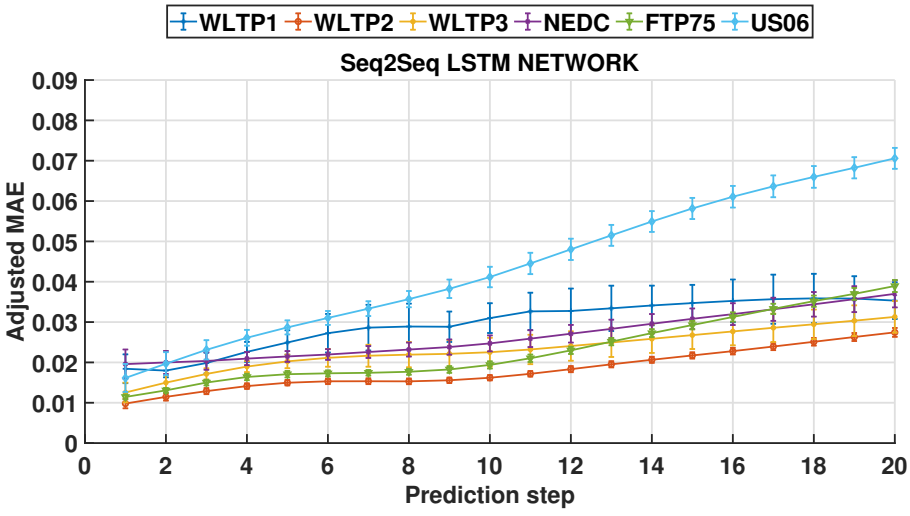

(c) Deep neural network (seq2seq), adjusted MAE

Figure 3.9: Sequence-to-sequence regression using deep learning.

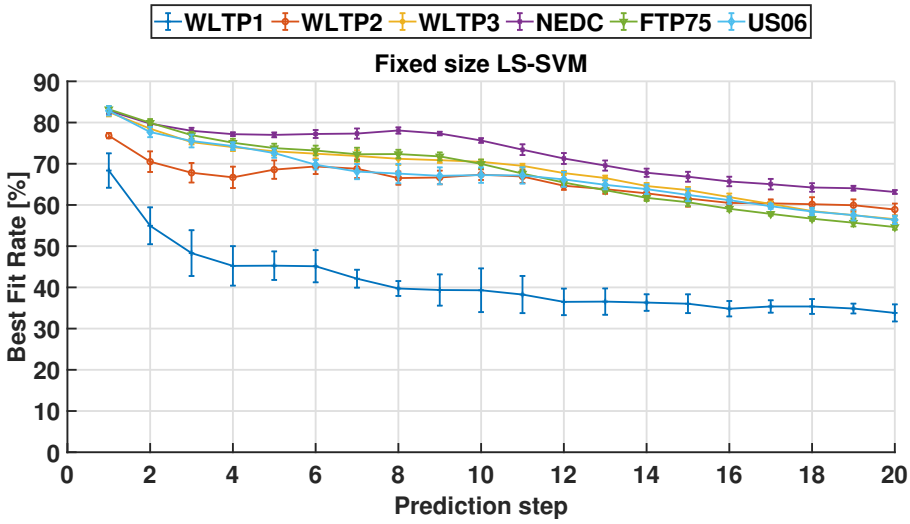

(a) Fixed-size LS-SVM, m=200, BFR

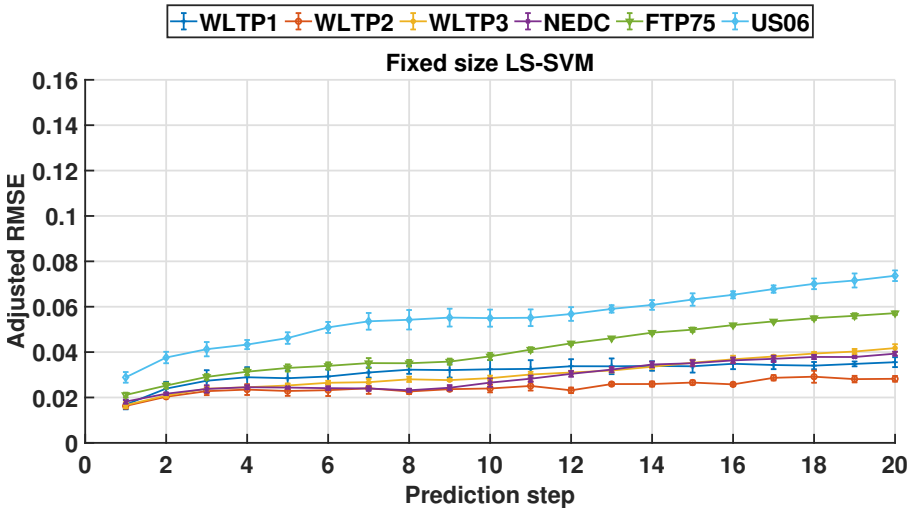

(b) Fixed-size LS-SVM, m=200, adjusted RMSE

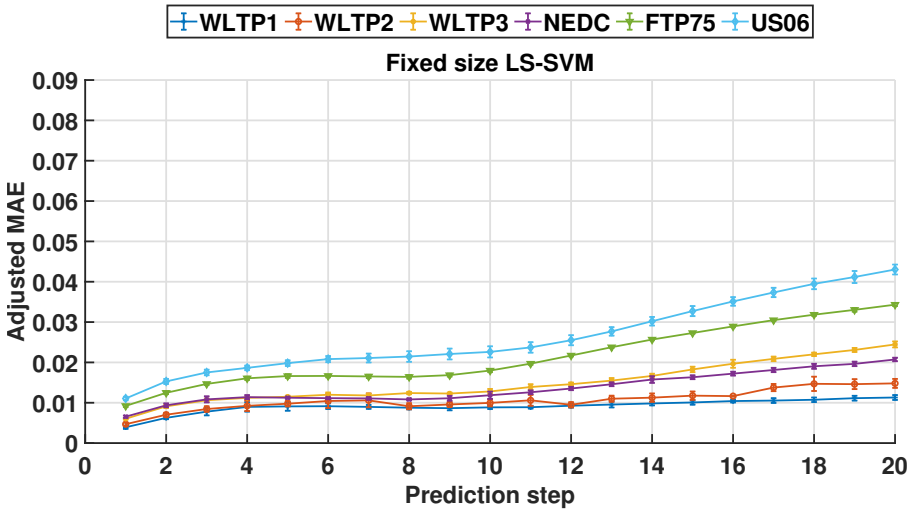

(c) Fixed-size LS-SVM, m=200, adjusted MAE

Figure 3.10: LS-SVM: fixed size model, m=200.

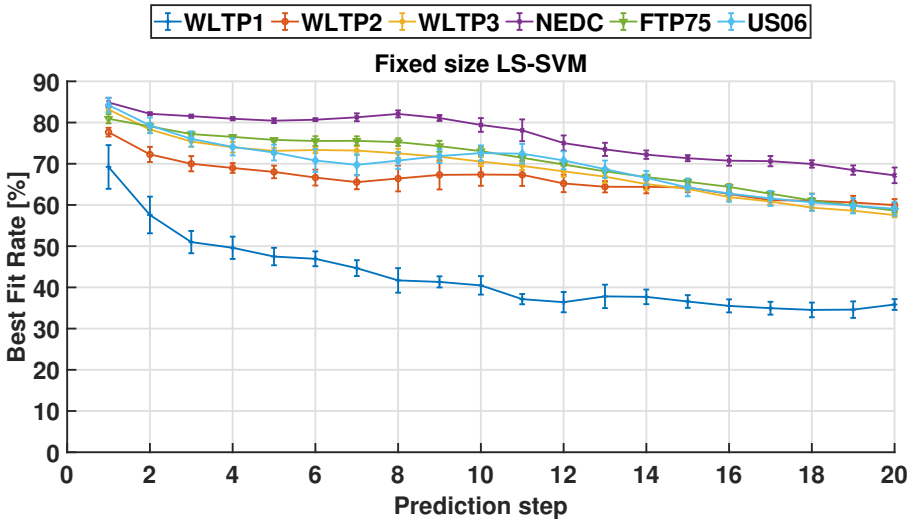

(a) Fixed-size LS-SVM, m=500, BFR

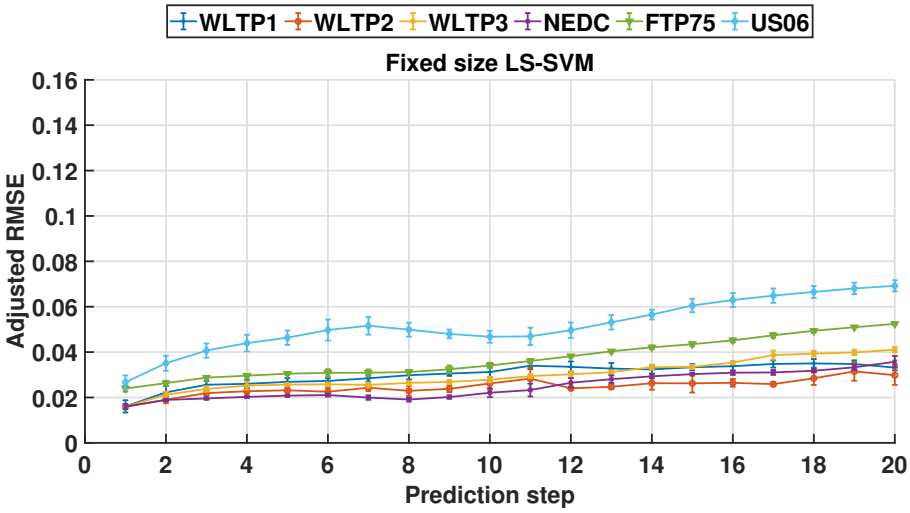

(b) Fixed-size LS-SVM, m=500, adjusted RMSE

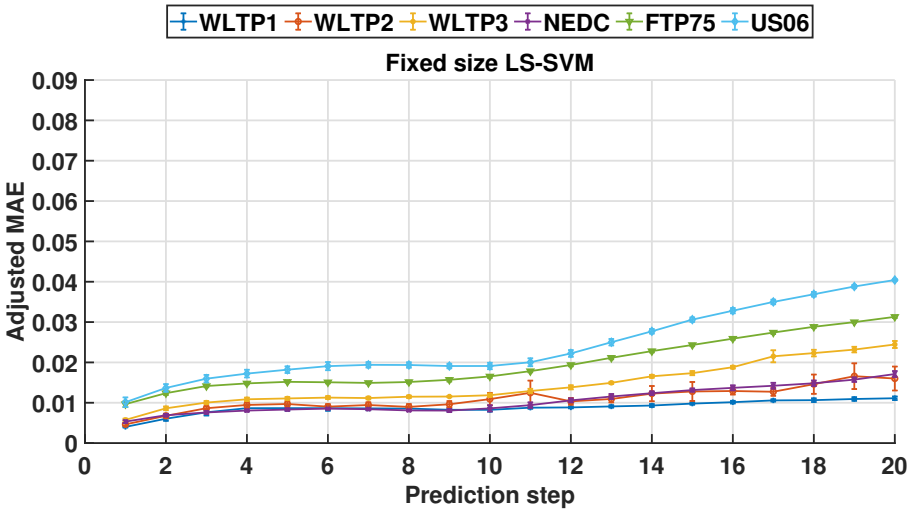

(c) Fixed-size LS-SVM, m=500, adjusted MAE

Figure 3.11: LS-SVM: fixed size model, m=500.

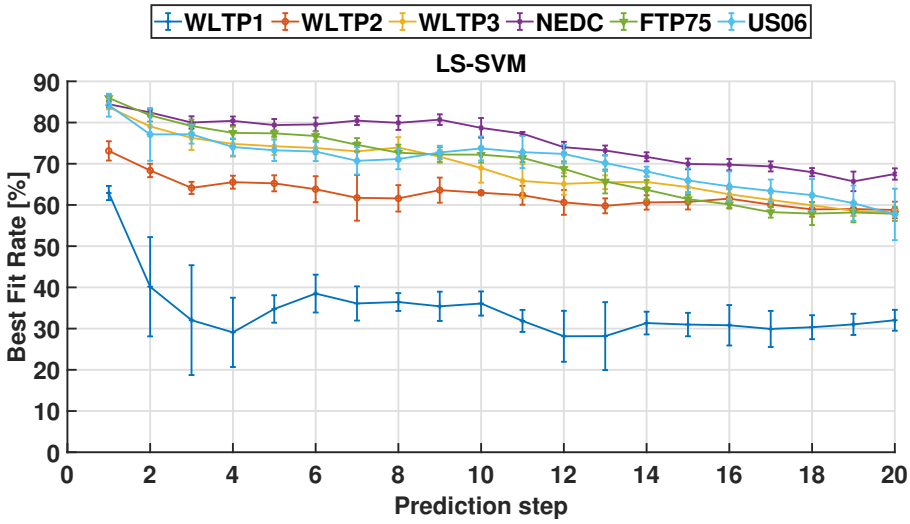

(a) LS-SVM, BFR

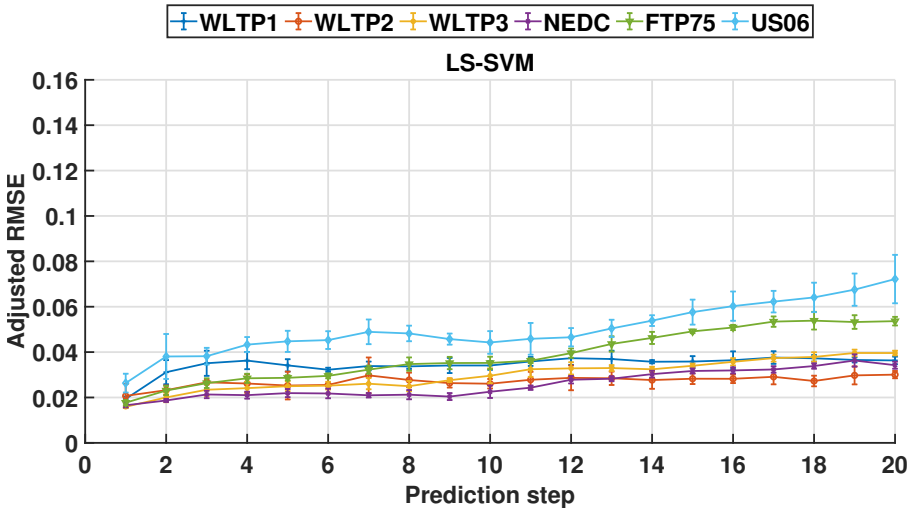

(b) LS-SVM, adjusted RMSE

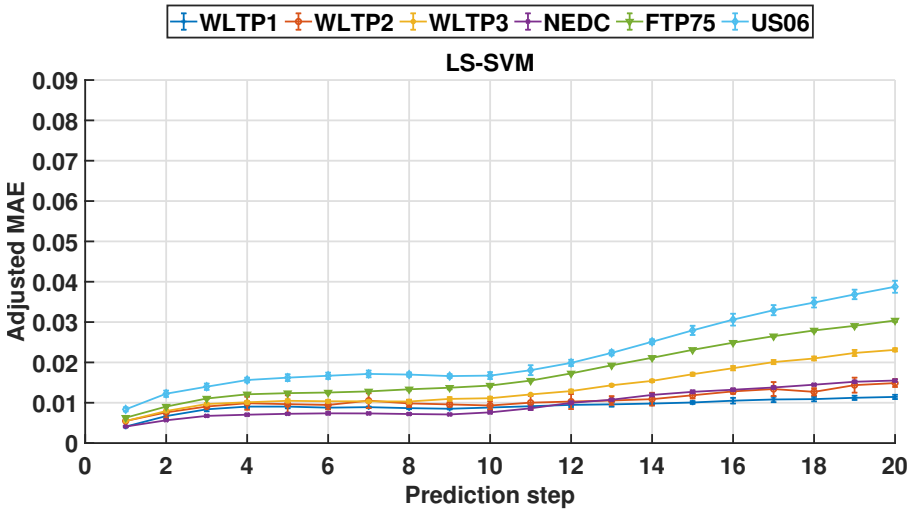

(c) LS-SVM, adjusted MAE

Figure 3.12: LS-SVM: full model.

	AVG BFR	STD BFR	AVG adjRMSE	STD adjRMSE	AVG adjMAE	STD adjMAE	Tcomputation (microseconds)
BASELINE	32.2	20.42	0.0680	0.0330	0.0313	0.0200	
EXPONENTIAL PREDICTOR	35.9	18.24	0.0641	0.0299	0.0308	0.0194	0.0027
FIXED-SIZE LS-SVM m=500	69.4	0.29	0.0519	0.0006	0.0240	0.0002	1.1516
FIXED-SIZE LS-SVM m=200	67.0	0.47	0.0555	0.0008	0.0263	0.0003	0.3423
CASCADE NEURAL NETWORK (Levenberg-Marquardt)	67.7	1.03	0.0556	0.0013	0.0268	0.0005	0.2853
MVN (1st order)	53.6	0.26	0.0778	0.0004	0.0405	0.0003	0.0019
MVN (2nd order)	59.5	0.39	0.0679	0.0006	0.0343	0.0002	0.0148
MVN (3rd order)	60.2	0.56	0.0668	0.0010	0.0345	0.0003	0.0734
Sequence-to-Sequence (LSTM)	49.2	1.57	0.0929	0.0026	0.0440	0.0004	3.4254

Table 3.1: Predictors Results

MVN, and exponential based predictors, whereas fixed-size LS-SVM requires a computational burden proportional to the sample number m.

3.5 Online Updating Procedure

In this section the online updating procedure for fixed-size LS-SVM predictor is described. In the literature, a incremental procedure for standard LS-SVM has been described in [133] and proposed for application in the automotive context in [134, 135]. In [136], the authors proposed a online learning algorithm based on incremental chunk for LS-SVM. Differently from the literature, in this work, starting by a fixed-size LS-SVM model, the entropy value is adopted to evaluate the novelty between a new sample and the existing sample in the training dataset $\mathcal{D}_N$ which is composed of predictor variables. The incremental algorithm updates the trained LS-SVM whenever the entropy of a new sample (x_{n+1}, y_{n+1}) is over a threshold fixed used by training dataset thus the new sample can be considered to improve the base of knowledge because this new sample can enhance the generalization of the LS-SVM model or reboost the model accuracy.

To develop the online update procedure in the dual form, since the solution is given by the set of linear equations $\Theta_n \hat{\alpha}_n = Y_n$, the next new model is given by

$$\Theta_{n+1} \hat{\alpha}_{n+1} = Y_{n+1} \tag{3.16}$$

where Y_{n+1} is the vector of samples $[Y_n, y_{n+1}, 0]$. In order to efficiently update Θ_{n+1} whenever a new sample is added without explicit computation of the matrix inverse, the matrix inverse Θ_{n+1} can be computed from Θ_n with the bordering method as in the following

$$\Theta_{n+1} = \begin{bmatrix} \Theta_n & u \\ u^T & a \end{bmatrix} \tag{3.17}$$

$$\Theta_{n+1}^{-1} = \begin{bmatrix} \Theta_n^{-1} + \frac{\Theta_n^{-1} u u^T \Theta_n^{-1}}{q} & -\frac{\Theta_n^{-1} u}{q} \\ -\frac{u^T \Theta_n^{-1}}{q} & \frac{1}{q} \end{bmatrix} \tag{3.18}$$

where $q = a - u^T \Theta_n^{-1} u$, and $u = [K(x_{n+1}, x_1), \ldots, K(x_{n+1}, x_n), 1]$, $a = \gamma^{-1} + K(x_{n+1}, x_{n+1})$. The above incremental procedure can update, reboost and improve the built LS-SVM model continually. At the next sample, the training dataset and the data vectors are incremented as follows

$$\mathcal{D}_n \rightarrow \mathcal{D}_{n+1} \tag{3.19}$$

$$x_{train} = [x_{train}, x_{n+1}]^T \tag{3.20}$$

$$Y_{train} = [Y_{train}, y_{n+1}]^T \tag{3.21}$$

and the Lagrangian multiplier becomes

$$\hat{\alpha} = \Theta_{n+1}^{-1} Y_{train} \tag{3.22}$$

However, the incremental procedure continually increases the memory length that enlarges the model complexity and reduces the computational speed, thus a First-In First-Output (FIFO) decremental procedure is therefore employed after every incremental procedure by removing the earliest trained data in the training dataset. Similar to the case of the incremental procedure, in order to avoid the computation of the matrix inverse, Θ_n must be updated from Θ_{n+1}, where Θ_{n+1} is the matrix without the first row and the first column. Following the decremental procedure, the decremented matrix is obtained as shown in Eq. (3.23)

$$\Theta_n(i-1, j-1) = \Theta_{n+1}(i, j) - \frac{\Theta_{n+1}(i, 1)\Theta_{n+1}(1, j)}{\Theta_{n+1}(1, 1)} \tag{3.23}$$

where $i, j = 2, \ldots, n+1$ and the training dataset and the data vectors are decremented as follows:

$$\mathcal{D}_{n+1} \rightarrow \mathcal{D}_n \tag{3.24}$$

$$x_{train}(1) \rightarrow \emptyset \tag{3.25}$$

$$Y_{train}(1) \rightarrow \emptyset \tag{3.26}$$

To test the proposed online updating procedure, the Fixed-Size LS-SVM model is trained with the driving cycle FTP75 and the driving cycle US06 is concatenated with FTP74 for testing. The figure 3.13 show the results in terms of normalized real torque and normalized torque prediction at 0.5-seconds horizon (5 steps ahead). The figures 3.13a and 3.13b show the cases with and without online updating procedure and the coefficient of determination, R^2, is reported as well. The online updating procedure permits to improve the results, in particular, the adjusted RMSE decrease from 0.183 for the case without online updating procedure to 0.0943 in the opposite case.

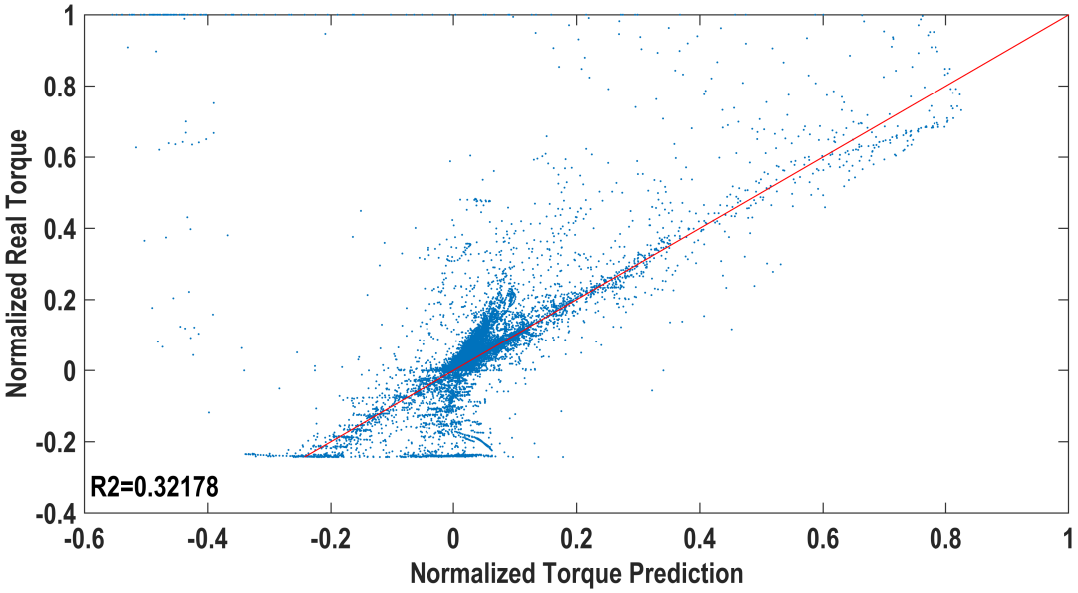

(a) Without updating

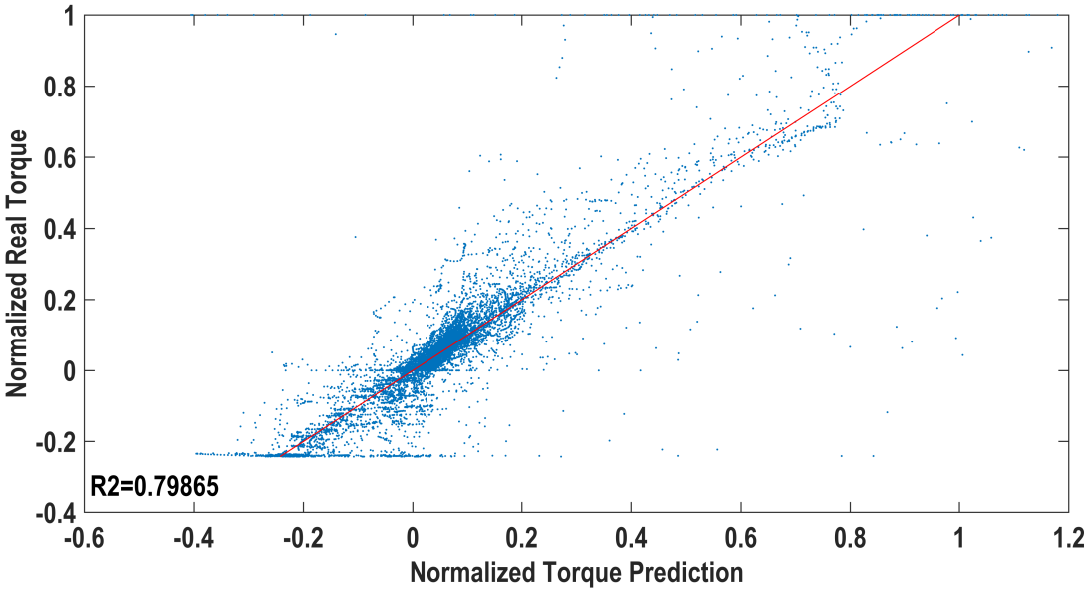

(b) With updating

Figure 3.13: LS-SVM torque predictor: R^2 plot.

The figure 3.14 shows the US06 driving cycle and the prediction at 0.5-seconds horizon with and without online updating procedure. The figure shows as the online updating procedure permits improving online the model in the case of driving style changes.

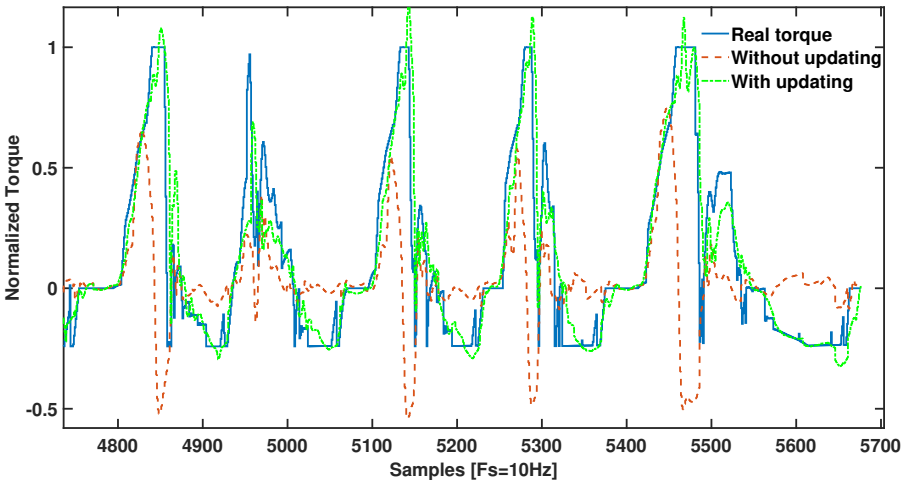

Figure 3.14: US06 driving cycle.

Thus, results show that fixed-size LS-SVM-based predictor is able to provide the best performance while tested over a range of well-known and certified driving cycles. Furthermore, the fixed-size LS-SVM-based torque predictor is investigated to evaluate capabilities given by the presented on-line updating policy used to adapt the data-driven algorithm to changes on the off-line evaluated driving style.

The study summarizes several results and related analysis providing a better understanding of available torque prediction policies suitable for H/EV EMS integration, contributing to the definition of a real-time approach that could improve EMS control in EVs and resulting in a reduced SOH rate degradation.

EMS are designed in order to lead powertrain in the best operating conditions by means of optimization-based technique. The MPC allows to control H/EV over a certain future horizon based on vehicle operating characteristics conducted by driver actions. In literature, studies have been conducted to analyse the effect of torque prediction and SOH trend. In [137], a battery wear model is included for powertrain optimal control problem, highlighting the effectiveness of a control strategy on reducing aging degradation and improve maintenance and costs management as well. Moreover, also Ebbesen et al. [138] proposed a formulation optimal control problem including a dynamic state-of-health model for a Li-ion battery. Then, a causal energy management strategy is derived applying a Pontryagin's minimum principal. The implemented solution results in minimisation of fuel consumption while maximizing battery life.

Chapter 4

V2G: Vehicle-To-Grid

4.1 Overview

The recent growth of EVs share into the transportation industry and their impact on the electricity grid open a new set of applications at different scales. The study of V2G paradigm strategies has become an important focus in both the electric mobility and distribution grid research areas. Each EV indeed can be seen as a mobile distributed BESS, thus giving to each consumer a potential active role in the energy distribution scenario.

In a residential scenario V2G, also referred as Vehicle-to-Building (V2B), is one of the most promising technologies which may have a significant impact on energy flexibility due to its capability to manage the load demand and to accommodate shares of intermittent renewable energy production. However, there is still a lack of large scale data (often location dependant) to test and deploy energy management strategies for vehicle-to-grid services.

In this context, tools able to simulate the behavior of an EV can be crucial to design, develop and test different DSF algorithms and scenarios. The proposed tool provides individual and aggregated charge, discharge and plug-in/-out events data of a custom geographically defined population of EVs, considering both home and public charging stations. The population is generated on the basis of statistical data (which can be obtained by data driven approaches or a priori assumptions) including commuting distances, vehicles models, traffic, social behavior of the owners and driving style of the consumer. It is designed as a web simulator as well as a Matlab/Simulink block, in order to facilitate its integration in different projects and applications. During the last years, several simulation approaches have been proposed in the literature but, to the best of our knowledge, none of them integrates a realistic modeling of the aging process of the battery. Indeed, the modeling of BESSs aging is necessary to simulate the real behavior of an EV and properly analyze the effects of DSF algorithms on the vehicles life.

4.2 State of the art

In last decade, many predictive models of different EVs scenarios and their possible interaction with electrical grid have been developed due to the ongoing increase of electrification of the transportation market and the absence of significant datasets.

In 2009, Karnouskos and De Holanda [139] developed a simulator built on an agent-based tool, modeling the discrete heterogeneous devices that consume and/or produce energy, that are able to act autonomously and community in a smart city context, including EVs and smart homes. Their simulation approach consider that objects, such as house appliances or EVs, change their behaviour and the energy capable to exchange following possible event that could casually occur during simulation (e.g. the unplugging of a device) or modeled by

a probability distribution, such as the chance of unexpected traffic jams or other adverse conditions.

In 2010, Pillai and Bak-Jensen [140] proposed a study that aims to model the EVs power load onto a Danish distribution grid, considering different EVs population ranging from 0% to 50% of the total numbers of cars in the district. These EVs are characterised by two particular type of recharging modes: a 40% of EVs follow a "smart recharging" procedure, taking into account fixed amount of charging time and loads shifted towards hours of low electricity prices; a 10% of the total vehicles were EVs characterised by a "dump recharging" with no time constraints. Unfortunately, neither geographical or traffic information, nor a costumer profiling or a consumer population based on a statistical distribution or model have been included in this case study.

In the following years, the focus of scientific study has been shifted toward the study of model for recharging stations and EVs at circuital level, aiming for the development of novel fast-recharging modalities and V2G oriented bidirectional AC/DC, DC/DC converters [141, 142].

In the years between 2014 and 2019, several studies have proposed both custom and commercial simulators, modeling and combine hourly-distributed energy consumption profiles in a wide grid scenarios, in order to develop and test strategies that deals with energy investments, scheduling issues, optimal topological arrangement of charging station as well power loss minimisation [143, 144, 145, 146, 147, 148]. Of particular interest is the study of Bedogni et al. [145], that improves several pre-existing simulators (Omnet++, SUMO and VEINS) those model event-based recharging operations, by means of traffic conditions and geographic information. The significant effort of this work is the focus on public recharging stations and a simulator, which offered recharging spot reservation. On the other hand, for consumer profiling only distance constraint and fixed time are considered and home-recharging events aren't treated.

Novosel et al. [144], featuring the MATSim and EnergyPLAN tools, proposed a model of the energy exchange and impact on Croatia, similarly to the work of Pillai et al. Here, consumer activities profiling and commuting distances are modeled based on parametric probability distribution drawing a distance vs traveling time realistic scenario. Moreover, more accurate model of energy production, import and export is developed, but at the expense of an accurate EV modeling.

In [147], Rigas et al. proposed a custom Java-based simulator named of EVLibSim. A thorough comparison with other existing tools is presented, confronting them in terms of V2G EVs and charging station modeling, electricity prices and scheduling. The simulator developed is based on an event-based approach to manage EV activities at charging station level, focusing on the model and the customisation of the latter. Although behavioural aspects of the district population are not considered, thus leaving out commuting distances, EV models and home recharge capabilities, a detailed model of charging station leads to an accurate simulation of charges, discharges and queues.

As last, the study of Canizes et al. [148] provided a tool to analyse the effect of the variation of electricity costs on the behavior of EV consumers. Not only an extensive comparison with current available tools is reported, rather a simulator is presented, improving consumer behaviour profiling, traffic conditions and home and public charging station customization. An optimisation model is integrated in the tool in order to determine the variable charging price. In conclusion, the study demonstrates that the variable-rate of electricity prices is a more advantageous solution for consumers, allowing to reduce charging costs while

contributing to the required grid flexibility, rather than modeling recharging events based on consumers' behaviour and electrical grid load.

None of the studies previously presented have considered the aging problem related to EVs batteries, which is particularly enhanced in a scenario where charging and discharge cycles are increased.

The Table 4.1 summarises every tool presented by scientific literature.

Table 4.1: Overview of the different simulation approaches in literature

Citation	**Vehicle Type**	**Vehicle Modeling**	**Price Driven Vehicle Choice**	**Plug-In/-Out Scheduling**	**Consumer Daily Routine Model**	**Daily Charge Data Generation**	**Traffic/Trip Simulation**	**Home Recharging**	**Public Station Recharging**	**Simulator (Language)**
ePopSimulator	EV, Hybrid	Yes	Yes	Yes	Yes	Yes (1,10,15,30) minutes resolution	Yes	Yes	Yes	Custom (Python, Matlab)
[148]	EV	Partial	No	No	Partial	No	No	Yes	Yes	Custom (R - RStudio)
[147]	EV	Yes	No	No	No	No	No	No	Yes	EVLibSim (Java)
[146]	EV, Hybrid	Yes (autonomy estimation)	No	No	No	No	Yes	No	Yes	Custom (Matlab/Simulink)
[145]	EV	Partial	No	Partial	Partial	Yes	Yes	No	Yes	Omnet++, SUMO, VEINS
[144]	EV + CO_2	No	No	No	Partial (Statistical)	No	Yes	No	No	MATSim, EnergyPLAN
[143]	EV	No	No	No	Partial	Yes	Yes	Yes	Yes	DER-CAM
[142]	EV	Yes (Battery model)	No	No	No	Partial	No	No	Yes	Custom (Matlab/Simulink)
[140]	EV	Yes	No	Yes	Yes	Yes	No	Yes	No	Custom
[139]	EV	Yes	No	No	Yes	Yes	No	Yes	No	JADE

4.3 Simulator Architecture

The proposed simulator architecture is composed of a cloud-based component, a Simulink and an aging simulator blocks. While the cloud-based simulator can work as a stand-alone tool, the Simulink block, which can be added to any custom Simulink project, needs to be initialized with the output data provided by the cloud-based simulator. The `AgingSimulator` is integrated in the architecture processing charge and discharge cycle provided and computing the consequent decrease of SOH.

An overview of the software architecture is shown in figure 4.1. The cloud-based frame, as shown on the top of figure, represents cloud-accessible software to compute a simulation without considering an aggregation approach. Simulated consumer habits and profiling are thus downloaded and provided to the offline Simulink block through the `Initializer.m` script. The bottom frame represents the customisable offline Simulink-based simulator. The Aggregator Online Assistant (AOA, in the orange box), explained in detail in the following sections, manage the recharging procedures imposed by the custom aggregator logic (green box), following the simulated habits and requirement constraints of the EV owners simulated in the online block. The aging simulator, implemented as an external service, estimates, based on charge and discharge profiles imposed by AOA, the SOH of all the EVs batteries simulated.

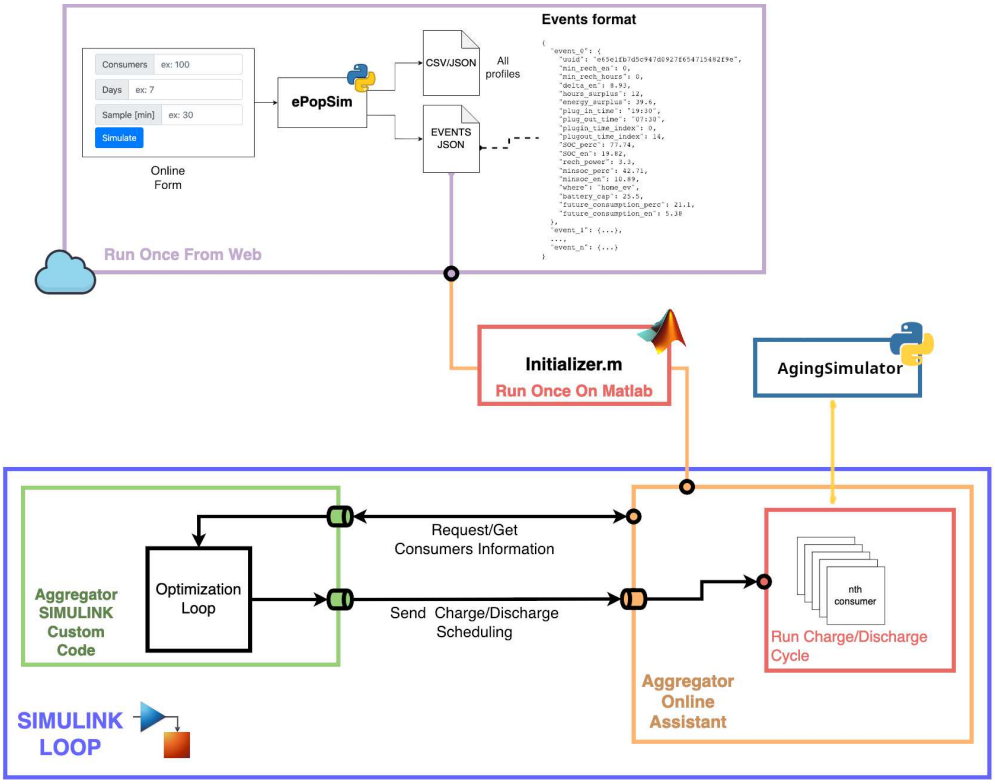

Figure 4.1: Software architecture scheme. The cloud-based frame is shown on the top. The bottom frame represents the customisable offline Simulink-based simulator composed of the AOA, which manage the recharging procedures controlled by the custom aggregator. The aging simulator the SOH of all the EVs batteries simulated.

In the following subsections, the detailed description of the model as well as its usage

guide will be covered.

4.3.1 Cloud-Based Tool

As stated above, the web-based tool consists of a standalone simulator that can be configured to simulate the behavior and relative power load of a EVs district consumers. The main simulation parameters, i.e., the number of consumers to be simulated, the number of days and the sampling time of the simulator engine can be set through the form shown in figure 4.2, while a set of `Advanced Options` will be explained in the following section.

Configuration

Figure 4.2: Main configuration form of the web-based tool. The `Advanced` button allows the user to access to more specific configurations.

The proposed model is structured in a bottom-up approach: it's based on the definition of the single consumer through the `Consumer` class and then the aggregated output is computed. Each consumer is modeled by the means of the following class arguments:

- Commuting distance (km)
- Electric vehicle
  - Car model
  - Battery capacity (kWh)
  - Declared vehicle autonomy (km)
  - Average vehicle fuel consumption (kWh/km)
  - Domestic charging point capacity (kW)

Commuting distances for a specific consumer population can be assumed from statistical distribution or computed through available data or surveys. The default value used by the

simulator, as shown in figure 4.3 (blue bars), is obtained from an Italian Statistic Institute survey, while users can vary the commuting values in the `Advanced Options` form (see figure 4.4) as shown by red bars. Figures 4.3a and 4.3c, corresponding to commuting distances and car prices respectively, represent the consumers population parameters used by default (blue bars) or defined by user (red bars). In figures 4.3b and 4.3d the distributions are generated according to parameters set for 1000 consumers. Thus, an EVs district can be described by means of on geographical and economical characteristics.

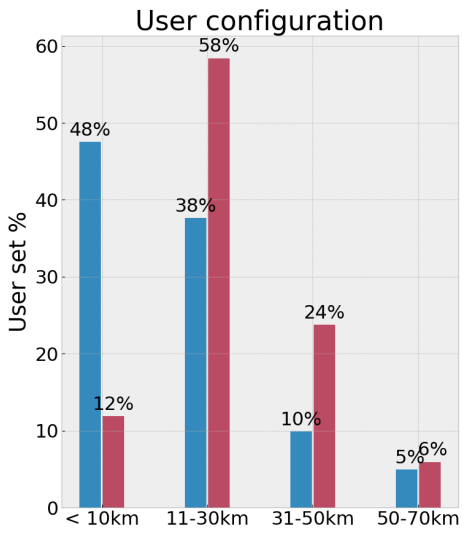

(a) Commuting distance configuration

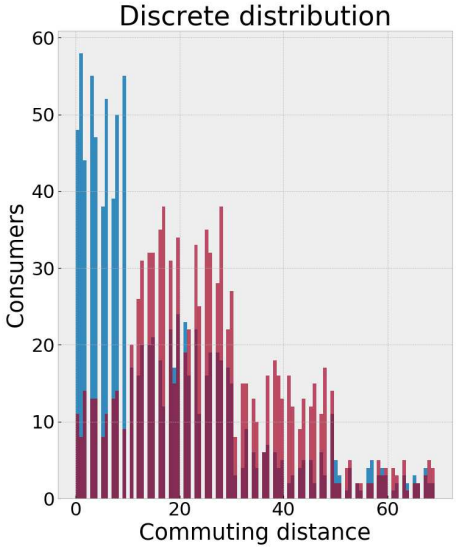

(b) Commuting distance distribution

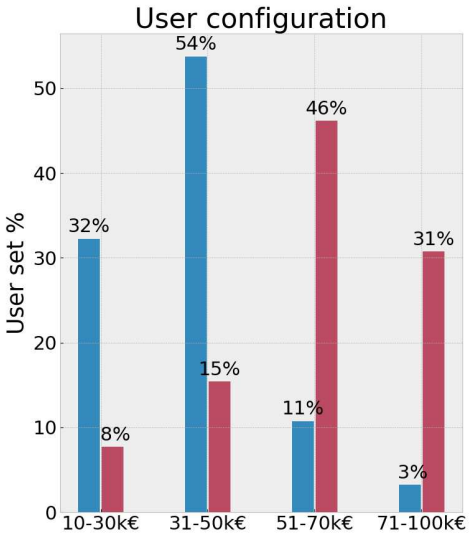

(c) Car prices configuration

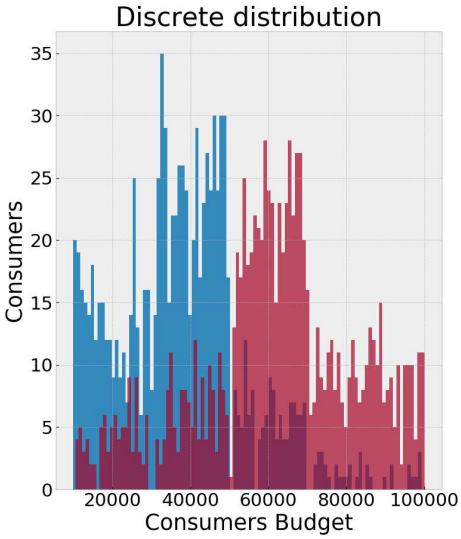

(d) Car prices distribution

Figure 4.3: Different consumer population based on commuting distances and budget distributions. Blue bars represent simulator default values while red bars indicate a population with arbitrarily defined characteristics.

The EVs population is determined combining the distribution of prices paid by consumers for EVs (customisable in `Advanced Options`) and a matching between specific EV model

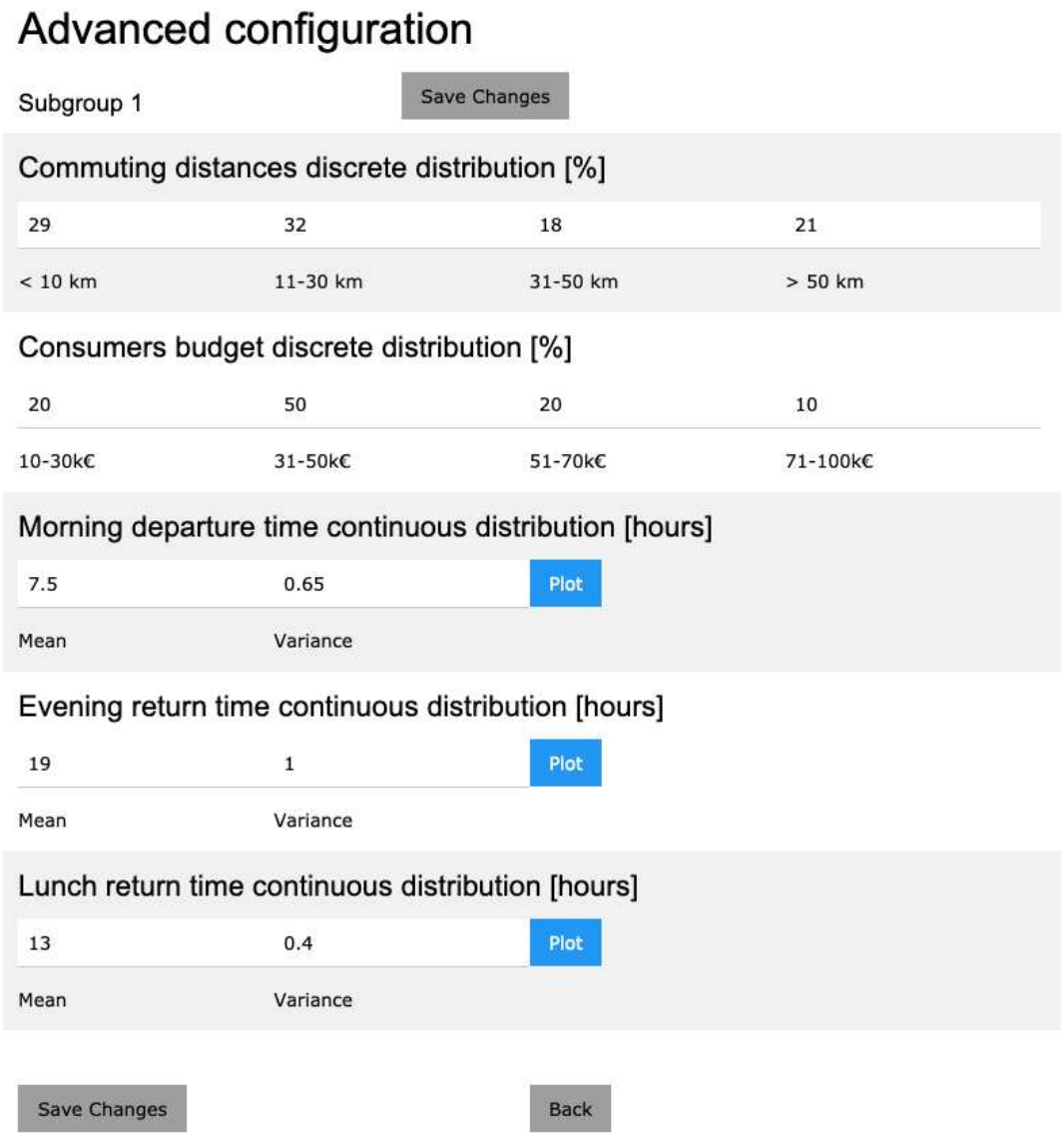

Figure 4.4: Several parameters can be set for each subgroup, including commuting distance distribution and budget distribution, as well as morning, lunch and evening plugin/plugout time continuous distributions.

and single consumer' commuting distances. The default price ranges are shown in figure 4.3. EVs characteristics and technical specification (model, price, battery capacity, autonomy and average fuel consumption) are obtained from the manufacturers web pages and automatically updated quarterly. Each home charging point available power can be randomly assigned or defined by a custom distribution among 3, 4.5 and 6 kW. The simulator core logic is an event-based process where each event is determined by each consumer's daily routine, i.e., charge/discharge cycles, considering the overall configuration. These events are simulated based on probability plugin/plugout functions, so that real variability of charge and discharge cycles is efficaciously replicated. For example, evening plugin and morning plugout probability density and cumulative distribution functions are reported in figure 4.5. Figure 4.5a depicts plug-out distribution at morning, whereas evening plug-in events are modeled as shown in figure 4.5b. The different curve colors indicate default values used by simulator (blue distributions), while the red distributions reflect an example of user defined parameters. The user can customize these distributions in the `Advanced Options` form. Red bars represent population defined arbitrarily using the `Advanced Options` window.

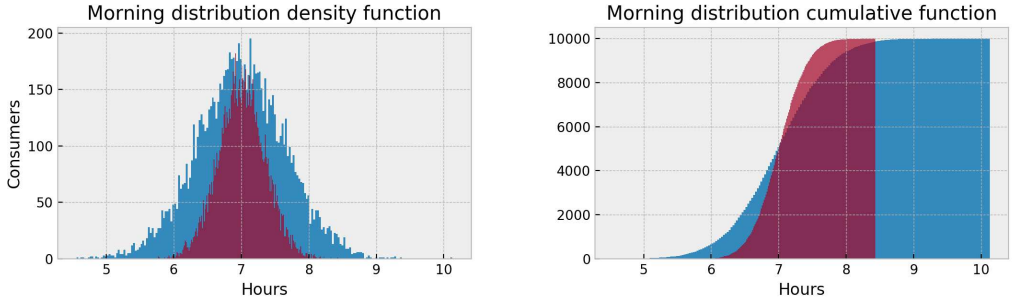

(a) Plug-out generated distribution

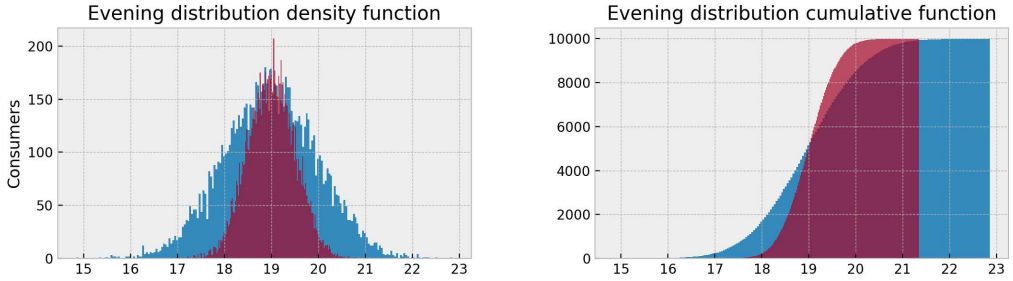

(b) Plug-in generated distribution

Figure 4.5: Morning and evening distribution density and cumulative functions relative to plugin events and plugout events.

Furthermore, these configuration settings can be applied to four different subgroups of consumers. Each subgroup is composed, as defined in the card of figure 4.6, of a percentage of total consumers previously set in the form of figure 4.2. This additional feature allows the user to simulate a more heterogeneous array of consumers with different habits, incomes and commuting distances.

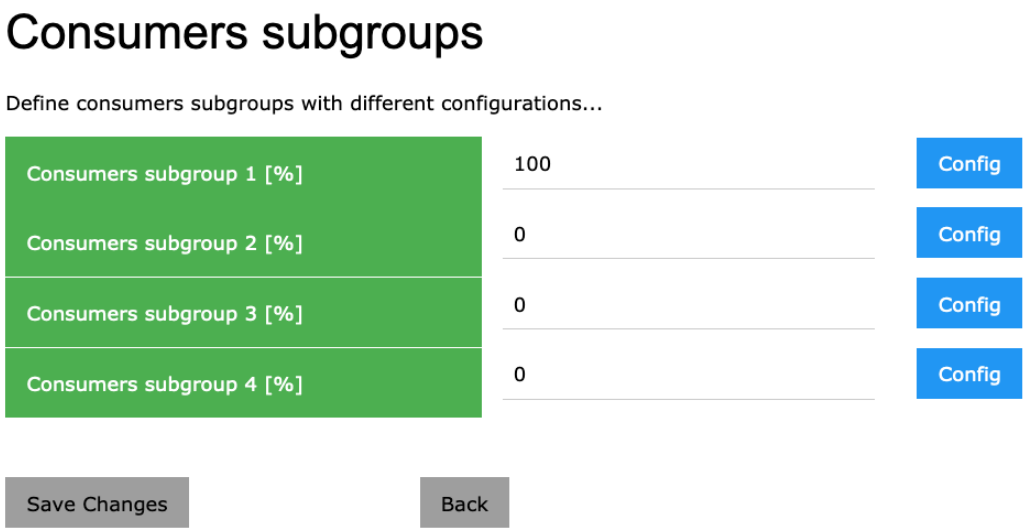

Figure 4.6: All the configuration options described in the *Configuration* section, can be applied to four different subgroups, expressed as percent values of the total number of consumers to be simulated.

Simulation Engine

A typical simulation run can be visualized in figure 4.7. Based on configuration parameters set by the user, the simulator initialises consumers population and generates each daily routine for the whole simulation execution time. Also statistical distributions fitting functions and pseudo-random variables behavior can be customised before the simulation run.

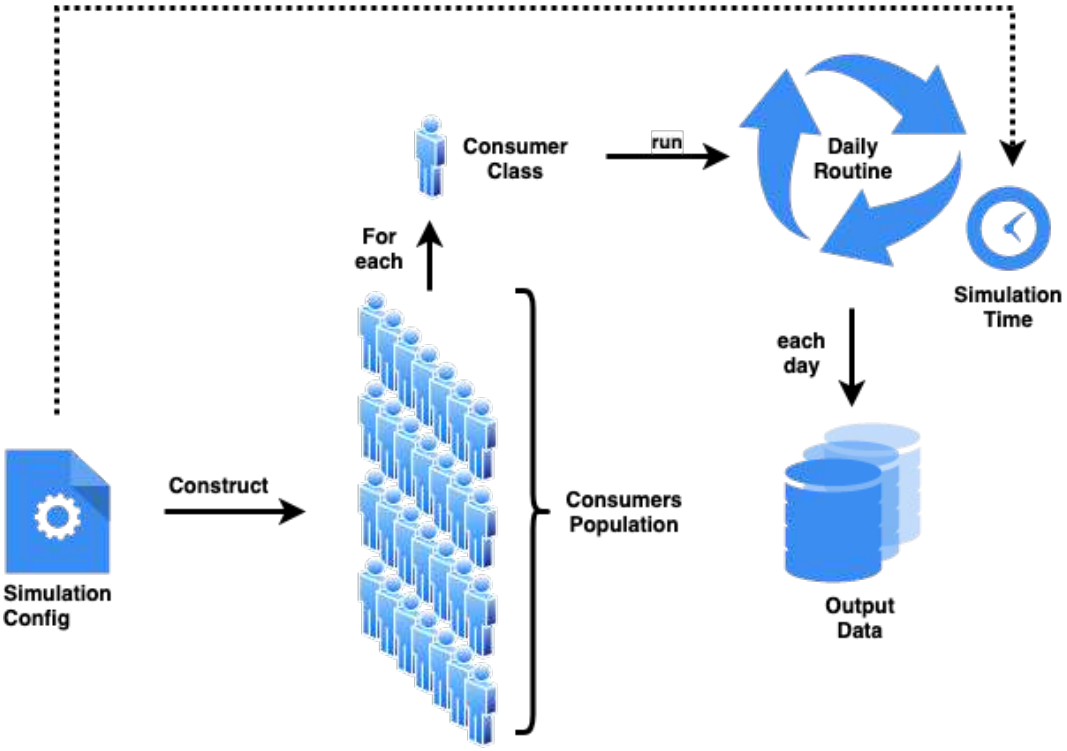

Figure 4.7: Graphical representation of the simulation engine.

Firstly, a daily routing is simulated for each consumer as depicted in figure 4.8. Each simulation day cycle is composed of five main events:

1. *Night*:
   A consumer charges his/her EV until it reaches a SOC of 100% or until plugout time. The domestic recharging device optimises, based on commuting distance and taking in account a margin, the quantity of charge that would allow the consumer to afford the expected driving route for the next day.

2. *Morning*:
   The consumer travels from his/her dwelling to the workplace. The plugout time is computed from the morning plugout probability distribution. Furthermore, traffic conditions are considered to positively or negatively affect the actual energy consumption as shown in (4.1) and (4.2):

$$d_{eff} = d + k \cdot \|\mathbf{v}\|; \text{ with } k \in \{-1, 0, 1\} \tag{4.1}$$

   Where d is the commuting distance traveled by the consumer, d_{eff} models how much the traffic conditions affect the actual distance and time, $\mathbf{v} \sim N(0, \sigma^2)$ is a normal

distribution with σ as the traffic variance parameter (expressed in km), and k is a control parameter (σ and k can be changed in the `Advanced Options` form). When $k = 1$, then $d_{eff} \geq d$, and traffic conditions are set as adverse. When $k = -1$ then $d_{eff} \leq d$, hence traffic conditions are established to be favorable. When $k = 0$ then $d_{eff} = d$ and no variability is applied. When a user does not set the parameter k, the formula becomes:

$$d_{eff} = d + \mathbf{v} \tag{4.2}$$

3. *Lunchtime*:
   This event is randomly triggered if a consumer has a low commuting distance. In such case, the model will compute a brief EV recharge during lunchtime, with an operation analogous to the *Night* phase. After this time lapse, the consumer will return to the workplace as in the *Morning* phase. At this point, a further computation of d_{eff} is performed, since the consumer actively travels toward home and back again to the workplace for the lunch break.

4. *Afternoon*: Even this phase is triggered pseudo-randomly; the consumer may decide to recharge his/her EV in a public charging station for a variable time lapse before returning to home from the workplace. This could affect the SOC of the vehicle for the evening plugin.

5. *Evening*: The consumer travels home a distance equal to d_{eff} and plugs the vehicle into the home charging station according to the evening plugin probability distribution.

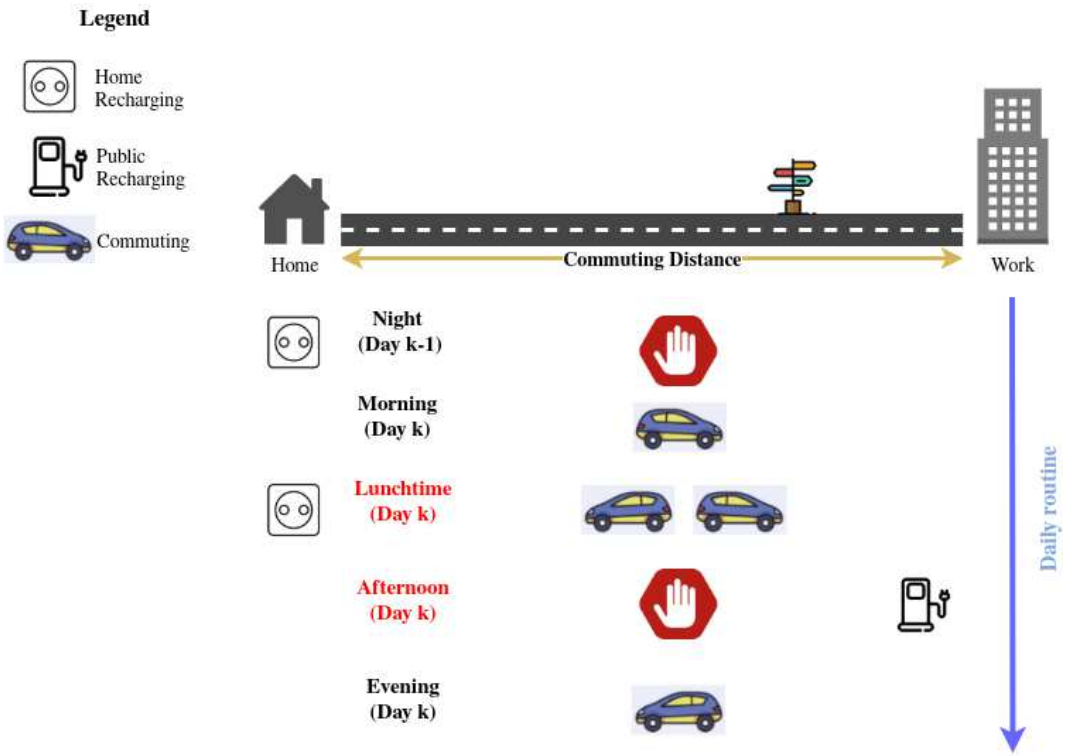

Figure 4.8: Consumer's daily routine.

In this version, a differentiation between weekdays and weekends is not implemented. This behaviour should be further introduced in order to improve simulation effectiveness.

Output Graphs

The software produces interactive plot for both single consumer's (see figure 4.9) and aggregate (figure 4.10) behaviour for power demand and energy consumption. In figure 4.9, power and energy supplied to the EV by the grid are represented by the blue and light-blue curves for each time sample. The dotted curves represent the SOC and MINSOC (i.e., minimum amount of energy to be charged in the EV) values of the EV for each time sample. The light-blue frames represent the time epochs in which the EV is actually connected to the grid.

Single consumer chart depicts for each time step the main variables simulated while the EV is being recharged:

- energy charged into the EV from plug-in events (kWh, light blue line)
- charging power (kW, blue line)
- actual SOC of the EV (%, light green dotted line)
- MINSOC, which is the minimum amount of energy to be charged in the EV to travel the expected mileage after plug-out (%, green dotted line)

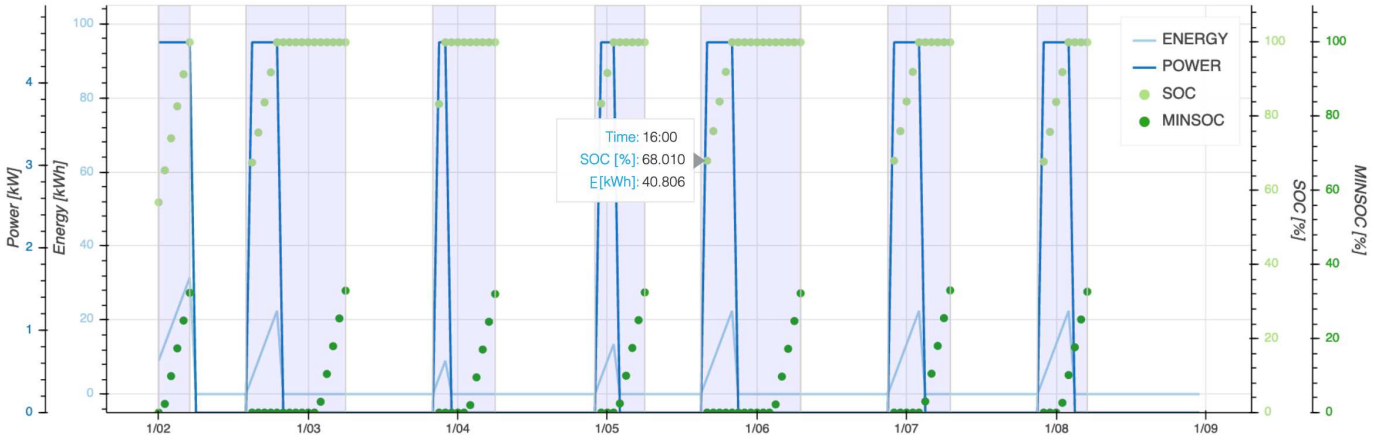

Figure 4.9: Plot of a single consumer's simulation for a week of charge/discharge cycles.

Figure 4.10 presents the flexibility available for the grid from an aggregator of the EVs charging stations. The first panel presents the supplied power and energy from the grid to the EVs. The second panel shows the EVs fleet SOC and MINSOC in terms of energy contained in the battery. The third panel depicts the energy available to the grid from the EVs fleet (pink curve) and the energy that could be supplied to the EV fleet (red curve) for each time sample. More specifically, the beginning of the red curve corresponds to the total residual energy of the whole fleet at the moment in which they plug-in. Consequently, the availability to purchase electricity from the grid drops when the recharge is in-progress and it becomes nil when the entire fleet is fully charged.

The overall charging events for each consumers' home recharging process, including plugin and plugout time instants and car model/recharging device-related information, are available in downloadable `json` or `csv` files.

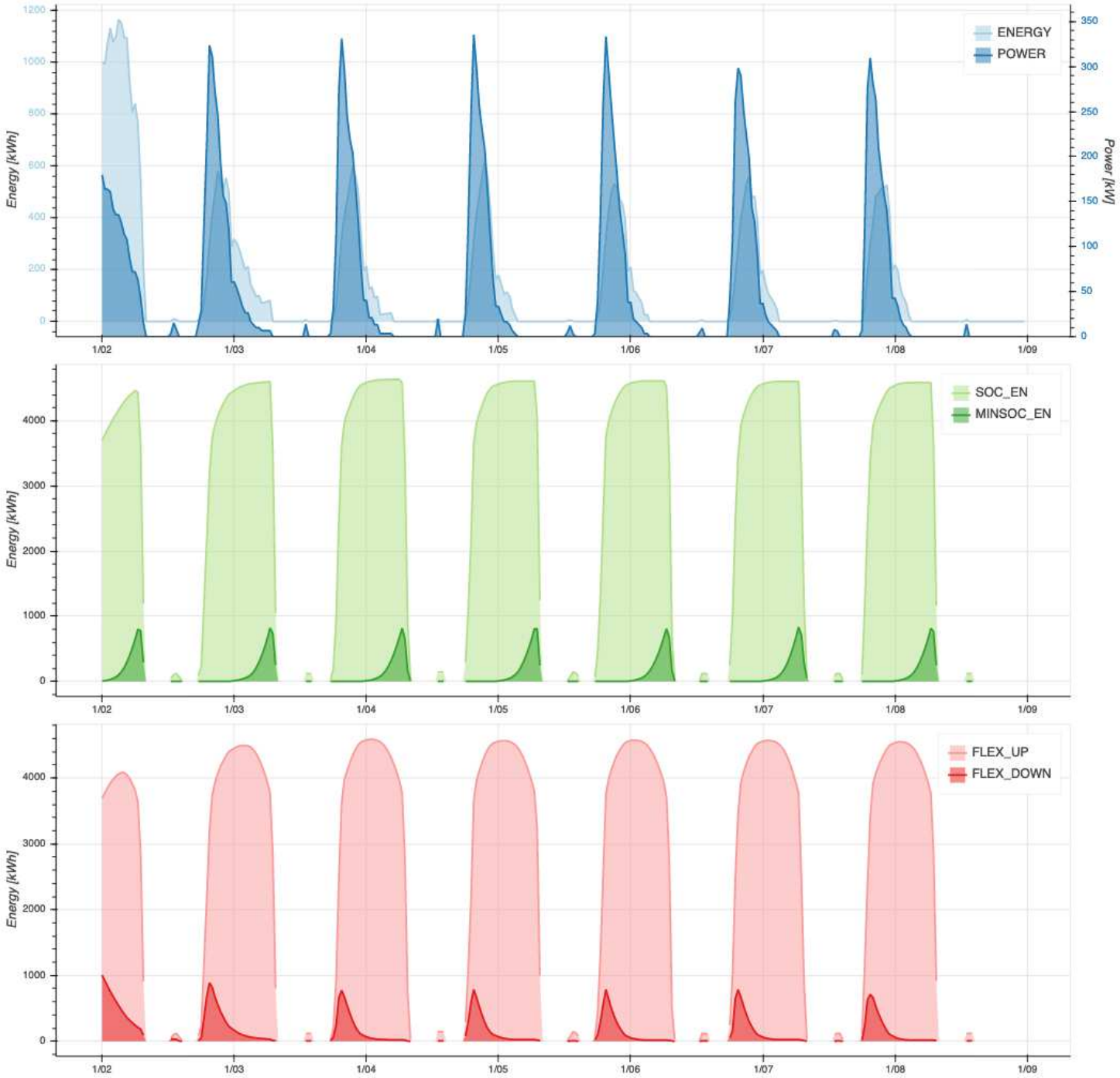

Figure 4.10: Aggregate output for 100 consumers, 7 days and a sampling time of 30 minutes. Definition of flexibility available for the grid from an aggregator of the EVs charging stations in terms of both energy to be supplied to the grid (V2G strategy, pink curve) and energy that the grid could provide (G2V strategy, red curve).

Output Files

The user can download the online simulation outcomes by means of `json` or `csv` files. All downloadable data are available both for each single EV (figure 4.9) and as aggregated results (figure 4.10). Here follows a detailed list of the data arrays available from the simulator:

- *Power*: Power supplied to the EV (or fleet of EVs) expressed in kW
- *Energy*: Energy supplied to the EV (or fleet of EVs) expressed in kWh
- *SOC*: State of charge of the EV (or fleet of EVs) expressed in kWh
- *MINSOC*: Represents the minimal amount of SOC that should be present in the EV battery (or fleet of EV batteries) for each time instant, in order to ensure the user required minimal SOC by the time of plugout. Expressed in kWh
- *FLEXIBILITY UP*: Amount of energy of the EV (or fleet of EVs) potentially available to the grid for each time instant, expressed in kWh
- *FLEXIBILITY DOWN*: Amount of energy the grid can potentially supply to the EV (or fleet of EVs) for each time instant, expressed in kWh
- *PLUGIN/PLUGOUT*: Plugin and plugout events for each EV in the fleet expressed in simulator time index and date-time format

4.3.2 Simulink Online Block

This section describes the configuration step of the Simulink block, its inputs, outputs and how to interact with it. Considered figure 4.1 presented previously, in the following the overview of the `Initializer.m` and `Aggregator Online Assistant` will be provided.

Configuration

The `Initializer.m` block handles the dependency of the Simulink block from the cloud-based tool described in the previous section. The initialization of the Simulink tool requires the following steps:

1. Run a batch simulation on the cloud-based tool with the chosen parameters, sampling time, number of vehicles and number of days and download the resulting `json` files.
2. Run `Initializer.m` on `MATLAB` to populate the workspace with the `Simulink` dependencies and variables.

Aggregator Online Assistant Core Logic

The Aggregator Online Assistant (AOA) comprises one input and two outputs. If the input is not provided it can work as a standalone block and its core logic is the same as that of the cloud-based simulator, leading each vehicle, when plugged in, to charge the battery until SOC reaches 100% or until the plugout time is reached. The information about the EV model, plugin/plugout instants, energy consumption and actual commuted distances is retained from the cloud-based simulation, while the power setpoint for each EV charging phase can be manually set. This implies that an external block (e.g., an aggregator, the owner of the charging stations, a grid operator or a scheduler etc.) can simulate and manage

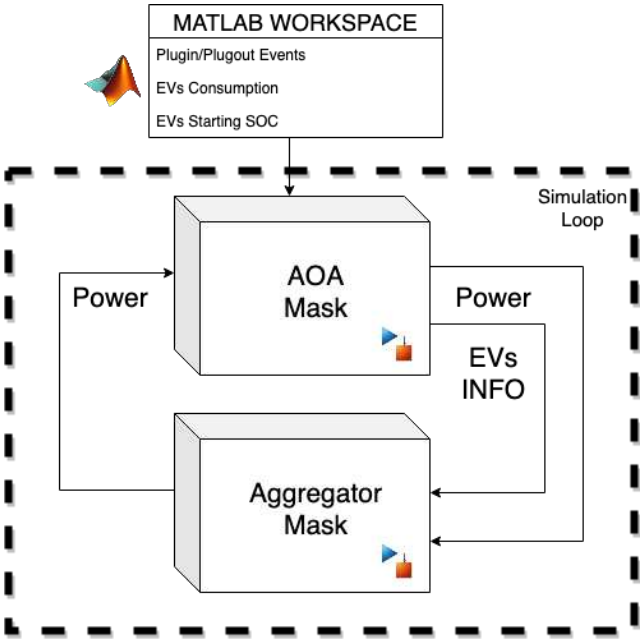

Figure 4.11: Schematic of the offline simulator architecture. See figure 4.1 for a more detailed representation.

real-time the charging and discharging power for each EV, while at the same time monitoring their status (see figure 4.11).

The I/Os of the AOA block in figure 4.11 are explained in the section below.

AOA Inputs

- *Power*:
  power values (kW) used as charging/discharging setpoints of the charging stations. Each array element represents a particular EV.
  - To positive power values corresponds a charging action for the given time instant in a G2V strategy. It's saturated to its maximum if the power overcomes the capability of the given consumer's station.
  - Negative values are treated as a discharge action for the given time instant in a V2G strategy.
  - Zeroes are treated as an "hold on" command, thus the specific EV will neither discharge nor recharge for that time instant.
  - `NaNs` (Not a Number) are treated as a "maximum power" instruction. The given EV will recharge at the maximum power allowed as well as in the cloud-based tool.

AOA Outputs

- *Power*: As for the input, this is an array containing the actual charged/discharged power for each EV at the given time instant.
- *SOC*: Ordered array of each EV's actual state of charge expressed in % value with respect to the maximum available `Battery Capacity`.

- *Time Until Plugout*: Ordered array where each value represents the remaining time instants until the given EV will be plugged out. A value equal to zero means that the corresponding EV is not plugged.
- *Minimal SOC*: Ordered array representing the minimum amount of SOC required by each EV at the given time instant in order to satisfy the user's requirements at the plugout time (`Time Until Plugout`). Zero values are returned if the EV is not plugged at that time instant.
- *Battery Capacity*: Ordered array containing the actual maximum battery capacity for each EV in terms of kWh. It considers aging models provided by `AgingSimulator` for each EV in order to estimate the battery state of health degradation.
- *Home Recharging Capability*: Ordered array containing the maximum home charging station power (kW). This array contains constant values for the whole simulation time.

AgingSimulator module

The AgingSimulator block acts as an external services and it is responsible to compute aging effect due to both cycle and calendar aging, as described in section 2.1.3. This software module can contains several aging model that could be related to specific consumer or EVs group, allowing to differentiate aging effect according to different vehicle or car manufacturer and specific battery characteristics obtainable from datasheet, such as battery size, chemistry, maximum power deliverable and so on.

As input, the AgingSimulator block takes both cycling and rest consumers' data profiles. It interfaces with the AOA that simulates how each vehicle discharges, is recharged and the time it is maintained at rest. Then, based on usage profiles simulated, the resulting degradation is modeled and aging effects, in terms of state of health and residual capacity, are returned for each EV. The process is presented in figure 4.12

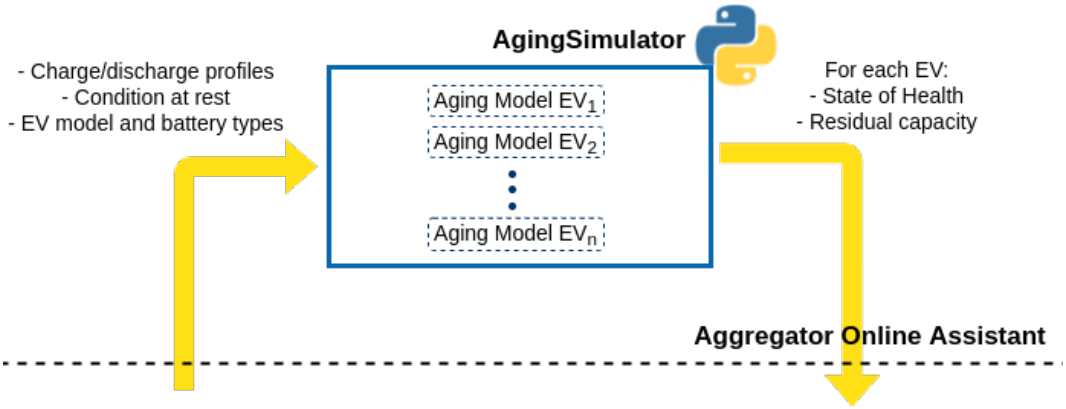

Figure 4.12: Aging Simulator Block

Aging block, thus, ensures the evaluation aging effect in e-mobility enriching information about BESS behaviour among the operating time and opens the way to tackle costs issue related to battery substitution due to degradation phenomena and, by a planning management point of view, to optimise maintenance costs. This simulator module can be furthermore easily integrated with geographical information about route and consumption related to type of route, such as if a highway, a hilly road or an urban path is traveled. Moreover, population

of batteries at different SOH value can be simulated, thus increasing the accuracy by which a district can be represented and improving the assistance that this tool provides to planning strategies.

4.4 Case Study

A real application is studied in order to evaluate the effectiveness of simulation software proposed and to demonstrate its real feasibility in case of V2G approaches. Indeed, although the simulator deals with both G2V and V2G strategies for an aggregate of EVs district, in this section a real peak shaving case study is presented. Specifically, an upper threshold is set for the global charging power absorbed from the grid whereas constraints related to the commuting distances and minimum SOC for all the EVs are still effective. These restrains require the design of a supervisor able to manage the charging scheduling of whole district.

A population of 100 EVs is created via the online tool and their charging/commuting constraints are generated for the period of one month. The options used to run the simulation can be found in figures 4.2 and 4.6. A fuzzy inference system is integrated in the Simulink environment to implement a custom power regulator, detailed in the following, able to provide a charging priority rank based on the following inputs:

- ChargeRequisite
- RechAvailability
- SOC

where ChargeRequisite and RechAvailability are computed as described in following equations:

$$\text{ChargeRequisite} = MINSOC - SOC$$
$$\text{RechAvailability} = \frac{t_{plugout} \cdot home_{pw}}{batt_{cap}}$$

The priority rank is then used to pick the vehicles based on a deterministic descending order until the power cap is reached.

4.4.1 Fuzzy Inference

A zero-order TS-FIS is implemented to obtain priorities from the input features. Trapezoidal function are considered as membership functions. A brief description of FIS and its input and output fuzzy set is presented in section 2.4.1.

The fuzzy system proposed is composed of three inputs and one crisp output (the priority level) and a weighted average is used as the defuzzification method. The values of the fuzzy sets are reported in Table 4.2.

4.4.2 Results

Different scenarios varying the power maximum limit are considered. In particular the cap is set to 70, 50, 23, 18, 14 and 10% of the maximum power required when all vehicles are charging at the same time (equal to $450kW$ in our scenario). Performance indicators are computed for each test set to assess the methodology effectiveness evaluating the difference between the minimum SOC required to afford the distance that should be traveled after the plugout and the SOC when it occurs.

$$\text{buff} = \text{SOC} - \text{MINSOC} \tag{4.3}$$

Table 4.2: Fuzzy sets of the input and output variables: linguistic terms and their corresponding trapezoidal fuzzy set parameters.

Input Variables	**Linguistic Terms**	**Fuzzy Sets (a, b, c, d)**
ChargeRequisite [%]	Negative	-100, -100, -20, 0
	Zero	-20, 0, 0, 10
	Lightly positive	0, 10, 20, 30
	Positive	10, 30, 100, 100
RechAvailability [%]	Low	0, 0, 30, 45
	Medium	30, 45, 60, 75
	High	60, 75, 100, 100
SOC [%]	Low	0, 0, 30, 40
	Medium	30, 40, 60, 70
	High	60, 70, 100, 100
Output Variable	**Linguistic Terms**	**Fuzzy Sets (Value)**
Priority	Null	0
	Low	0.4
	Medium	0.6
	High	0.8
	Absolute	1

Mean, median, standard deviation, minimum value and maximum value charging buffer values, computed as in Equation (4.3), over the whole number of charge cycles and EVs are reported in Table 4.3. Moreover, the buff-perc term indicates the percentage of EVs that are above the MINSOC value at the end of each charge cycle. The last column of the table indicates the maximum instant power provided by the grid supervisor. A one week plot depicting the global instant power provided by the grid in the different power limit scenarios is shown in figure 4.13.

Table 4.3: Descriptive statistics related to charging buffer values. Buff-perc term indicates the portion of EVs which are above the MINSOC value.

%	**buff-mean (%)**	**buff-median (%)**	**buff-min (%)**	**buff-max (%)**	**buff-perc (%)**	**PW-max (kW)**
test						
nolimit	66.8	66.2	9.8	97.9	100.0	435
limit70	66.8	66.2	5.2	97.9	100.0	297
limit50	61.4	54.3	4.9	97.9	100.0	198
limit23	30.2	17.8	-13.3	97.9	80.3	99
limit18	11.4	-4.9	-37.8	97.9	32.2	78
limit14	2.9	-9.3	-60.8	97.9	24.7	60
limit10	-9.2	-26.5	-85.2	97.9	23.4	33

The fuzzy-based system to determine charging priority ensures a positive mean buffer down to a 14% of power limit. For limit values lower than 10% the mean buffer results are negative, implying requirements are not satisfied for a certain number of EVs at a specific plugout time (morning or post-lunch departure).

The `buff-perc` column shows the percentage of plugout events (among all EVs in the entire simulation process) where the EV requirements are completely fulfilled. Below the 23

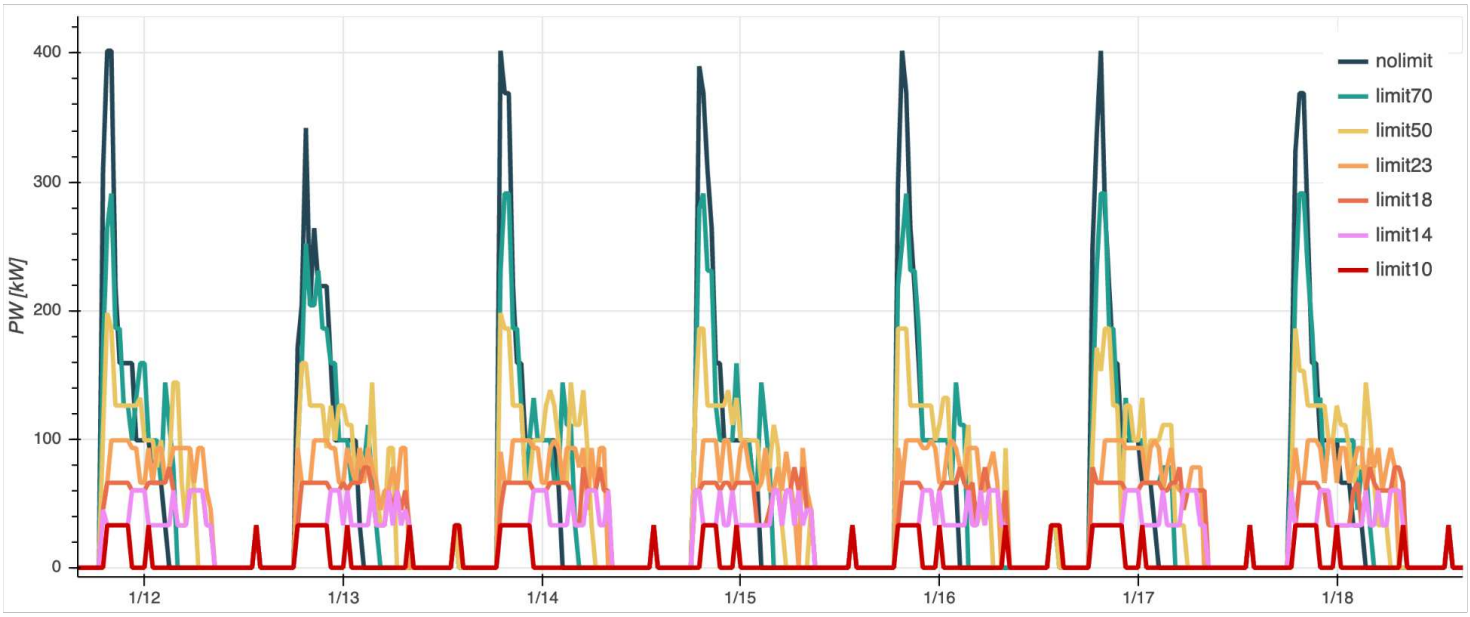

Figure 4.13: One week of global charging profiles. The power limits depicted are 100% (i.e., no limit, blue line), 70% (cyan line), 50% (green line), 23% (yellow line), 18% (yellow orange line), 14% (orange line) and 10% (red line).

% of power limit indeed, plugout events start to occur when the minimum SOC requirements are not completely satisfied for some EVs of the entire population. This means that for some consumers the value computed by Equation (4.3) is negative in spite of the positive buffer mean value. This determines a drop in the `buff-perc` column while maintaining positive `buff-mean` values.

Finally, implemented logic working during a nighttime recharging session is shown in figure 4.14 for a group of electric vehicles. The power maximum threshold is 10% and the height of the SOC step varies depending on the capacity of the domestic charging station. Four different heights of the steps are evident, corresponding with 3.3, 4.5, 6 and 11 kW of available power respectively. Each curve begins at the plugin time of the EV; the end of the series corresponds to the plugout. A 30 minutes sampling is used. When the SOC level shows a plateau, the relative EV has reached a lower priority level than other vehicles, thus recharging is temporarily stopped. From the individual recharging profile of each EV, it's possible to underline some aspects:

- EV1: at the plugin time, the battery has an enough charge quantity level to afford the next day route, implying as an output a very low priority. Thus, the vehicle starts to charge later than the others.
- EV2: at the time of connection to the charging station, the SOC is quite low (20%) but other EVs have higher priority because its MINSOC is lower than others and the maximum power supply of the charging station is at 6 kW, higher than others.
- EV3: starts from a very low SOC although it has low priority due to its connection to a charging station with high capacity (11 kW); furthermore, its recharge process begins later because other vehicles have higher priority since it does not have to reach a high SOC level and the estimated plugout time is sufficient to achieve the desired autonomy.

- EV4: it's one of the first to be recharged among the others due to its low SOC level and keeps a high priority for a long time; when its SOC level approaches own MINSOC, it loses priority over other vehicles.
- EV5: it's recharged before entering the house and connects it despite of its charge at 100%; this EV may provide flexibility to the domestic microgrid or to the national electricity grid in both V2B or V2G scenarios.
- EV6: this behaves like EV3 with a higher priority even if it has a lower MINSOC due to its inferior SOC level at the plugin time.
- EV7: at the plugin time, the SOC of the battery is high enough, thus it has a lower priority than the other EVs, even connected in subsequent instants; the power of its charging station is low (3.3 kW).
- EV8: at the time of connection to the charging station, the SOC of the battery is the lowest and it has a high MINSOC. At the first available instant the charge begins with a very high priority compared to the other EVs; the priority decreases as the SOC approaches the MINSOC.
- EV9: it behaves similarly to EV3 but it's characterised by a lower capacity charging station (6 kW).
- EV10: has the same behavior as EV8.

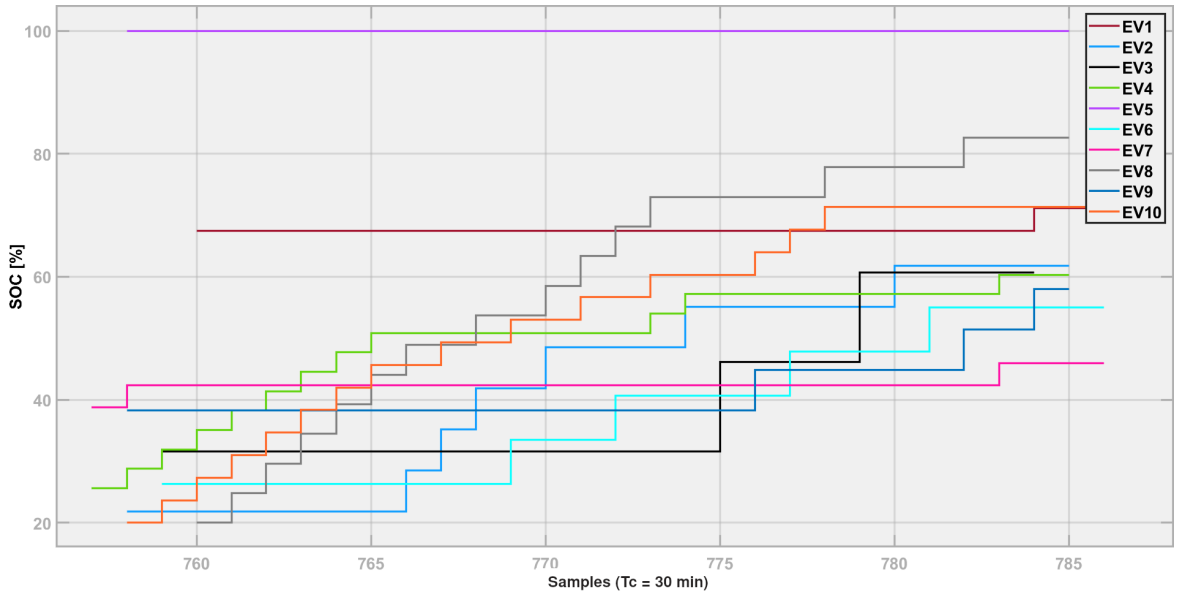

Figure 4.14: Extract from a simulation depicting the behavior of EV1, EV2 and EV3 as they are stopped until more urgent minimum requirements are met by other vehicles, such as EV7.

Aging effect

For this case study, Baghdadi model, as described in 2.3.2, is trained and implemented. Two dataset of the same battery typology are used for training phase describing the aging effect in a 50 kWh BESS at two different operating temperature profiles, 20°C and 40°C as depicted in figure 4.15. Green and blue lines represent the real curve used at two different temperature, 20°C and 40°C respectively. The yellow and the red curves show the respective model fitting. For this study, a single aging model is used for the whole EVs fleet. Optimum parameters obtained are shown in table 4.4.

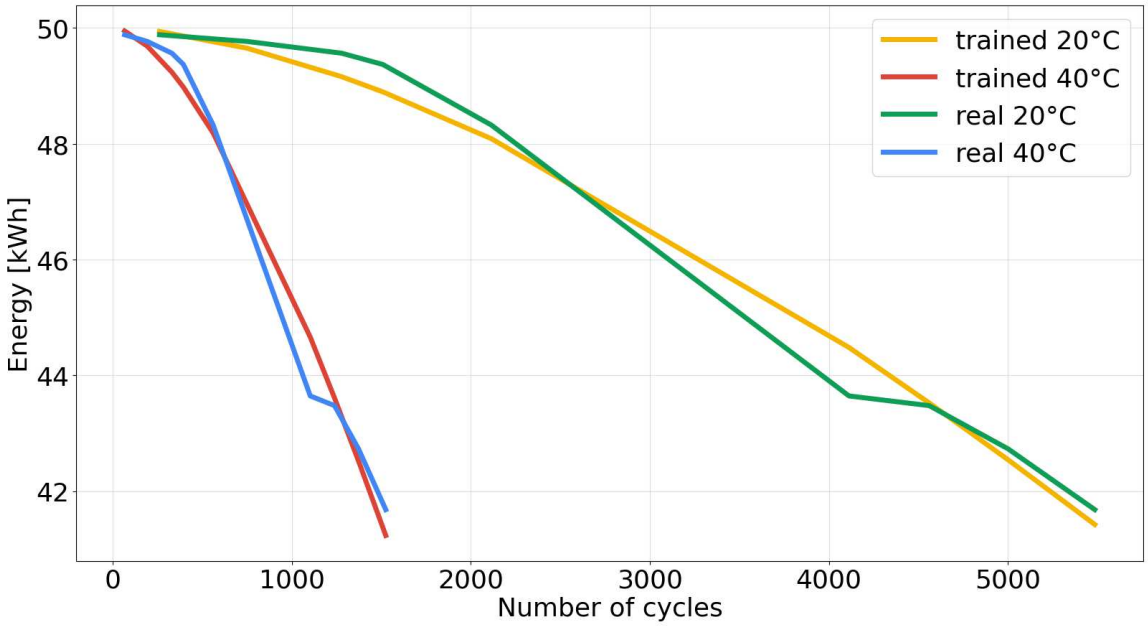

Figure 4.15: Results of model training on curves obtained from a 50 kWh battery size. Green and blue lines are the real curve whereas model fitting is represented by the yellow and the red ones.

Table 4.4: Parameters of trained model

k_1	k_2	k_3	k_4	k_5	k_6
-31.47	-55.1	52.12	1.65	-110.65	2.47

Temperature used as input for aging model is set based on the geographical region of interest, ranging from 15°C to 30°C. As future perspective, Geographical Information System (GIS) can be included to integrate real information about weather conditions and travelling route, which both affect aging dynamics. Then simulation conducted takes in account aging effect for each EVs: figures 4.16 and 4.17 depict the energy degradation of a single EV after 5 years of usage, resulting in an energy drop from 25.5 kWh to 23 kWh. A 10% of SOH loss is indeed simulated at the same SOC level (i.e. 100%) at different time instant, thus indicating a reduced amount of storable energy due to degradation phenomena related to aging.

These evaluations of aging dynamics along the entire EVs fleet are crucial for energy planning scenario, since it allows the prediction of maintenance and eventually substitution scheduling, possible management of second life and optimise charging/discharging load profiles according to aging dynamics, in order to reduce technological costs and increase the grid efficiency.

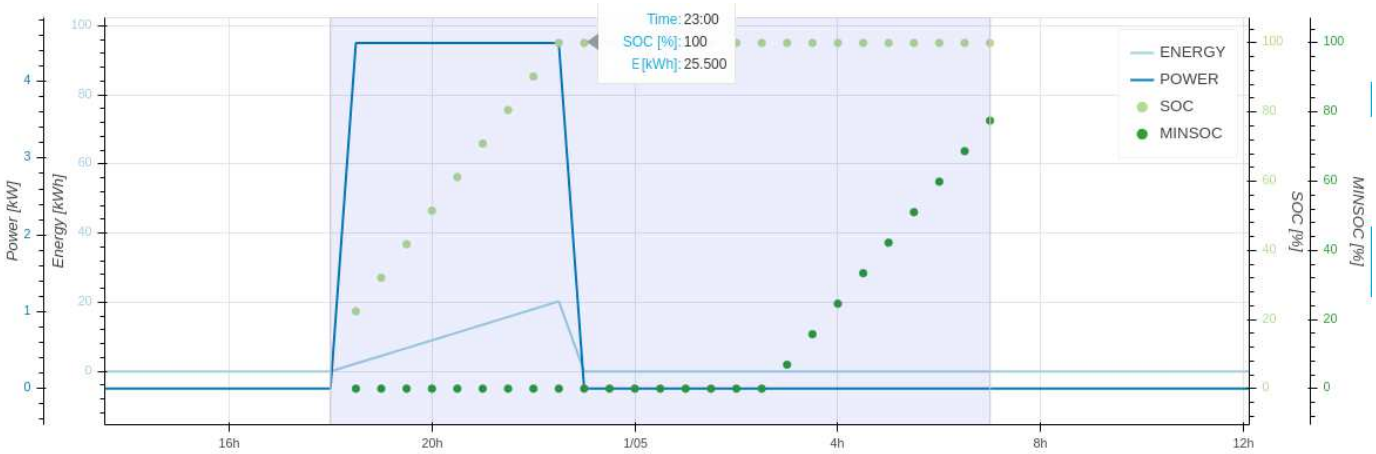

Figure 4.16: Simulation at beginning of life, nominal energy is 25.5 kWh at 100% SOC.

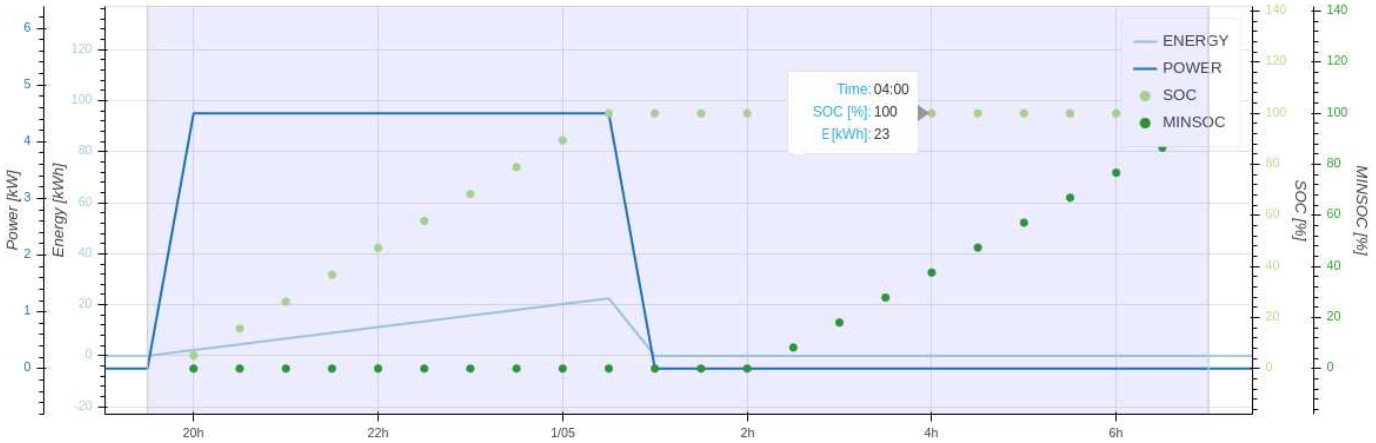

Figure 4.17: Simulation after five years of usage. Energy has dropped to 23kWh at 100% SOC.

Chapter 5

Conclusion

The climate crisis have oriented scientific community and companies toward green energy transition and technological progress in order to reduce greenhouse gas emission and phase out coal. On the other hand, electricity is increasingly holding a fundamental role for consumers well-being and benefits. Technological development in renewable systems requires the integration of BESS, those can decouple load demand and energy generation, assisting to solve intermittence problem and contributing to improve grid flexibility. In this thesis, BESSs are investigated and modeled in terms of aging and state of health and BESS-based application are analysed and developed.

SOH modeling remains a challenging task although scientific literature has widely investigated it. Unfortunately, the most of the studies do not present dataset acquired in real application but in experimental and controlled laboratory setup. In chapter 2, aging modeling is addressed and two contribution are proposed. Firstly, a sensitivity analysis is conducted among several aging models presented in literature to assess robustness to variation of input quantities, evaluating their capability to deal with unexpected variables as usually occurs in real application. Three models are selected and sensitivity is analysed with respect to change in current and temperature. Results report that models proposed by Baghdadi [89] and by Wang [64] represent the most robust models to variation in temperature and current respectively. Secondly, an algorithm for automatic online SOH estimation is studied and developed for three real case studies. It's based on a data-driven model fusion approach and aims to evaluate BESS aging degradation without a prior knowledge as concerns storage operating modality. Dataset have been acquired in utilities application, where BESS could operate as both energy and power intensive storage. Algorithm developed can be summarised in three main steps: BESS modality usage recognition, similar operating conditions detection throughout battery life and, as last, SOH estimation.

In chapter 3, SOH degradation in EVs is faced, analysing and comparing different methodologies for future torque demand prediction. Forecast of torque requested by driver is used in vehicles EMSs to optimise energy efficiency and adapting thereby battery usage intensity to driver need; thus, SOH is directly affected by the effectiveness of this control strategy. Several machine learning models employed in literature are included in this study, undergoing to an off-line training for an on-line torque time series prediction. Moreover, a LS-SVM based torque predictor with online update is included in the study as additional research contribution. Models are compared in terms of prediction capability and computational cost. Results show that LS-SVM based predictor provide the best forecast performance among the other predictors while tested on well-known driving cycles. In addition, update policy improves algorithm performance leading to a feasible online approach that could contribute to reduce SOH degradation. This should be further investigated.

The increasing growth of EVs penetration into the transportation market and their possible

impact on the electricity grid open a new set of applications at different scales. V2G scenario represents a promising technology that may have significant impact on energy flexibility due to its capability to manage load demand and to accommodate shares of intermittent renewable energy production. In chapter 4, a simulator is proposed to promote BESS integration with national grids and to assist energy planning management in DSF scenario. The proposed tool provides charge, discharge and plug-in/out events data of a statistically-based EVs fleet, considering both home and public charging stations, shifting the perspective from single vehicle to the aggregated population. A case study of real peak shaving is presented and analysed in order to evaluate its real feasibility in case of V2G approaches.

5.1 Future perspectives

Several further analysis and development could be conducted from the advancement achieved in this thesis project.

As regards BESS aging, a more thorough analysis can be conducted to evaluate each model sensitivity to other variations those can occur during real battery operating condition, such as DOD, mixed or alternated variations. A multivariate analysis, i.e. the evaluation of model response to variation in several inputs, should be firstly performed. In this scenario, Omar models [63] cannot be employed, since it computes number of residual life cycles using only one operating characteristic. Furthermore, an exploratory data-driven model study, such as the LS-SVM methodology previously presented in this thesis, should be carried out in order to improve aging modeling. Another crucial sensitivity evaluation related to the multivariate analysis comprises the study of how different operating cycles and how their order affect aging model leading to a significant deviation from real values. Furthermore, calendar model sensitivity should be evaluated, thereby considering how models proposed in literature respond to variation of temperature and SOC at which battery is maintained at rest. A model fusion approach should finally be validated for specific condition or application, combining different aging models according to their robustness to certain operating quantities. For instance, if the application of interest involves different operating temperatures such as working in winter and summer, different models could be integrated to improve aging degradation description. Concerning the developed algorithm for SOH online estimation in real application scenario, some methodologies could be further studied in order to improve, for example, V_{OC} estimation which represent a critical aspect unless the battery is maintained at rest for a certain amount of time, ranging up to some hours [149]. Several effort have been made by scientific community to improve battery characterisation, Kalman filter has been widely employed [150, 151, 152] and its capability to capture BESS dynamics should be evaluated also in the case of sampling time of order of minutes that could occur in real scenario.

An additional analysis to validate the effect of the improved torque prediction algorithm proposed on battery aging should be conducted. A decrease in degradation rate is indeed expected. Moreover, torque forecast could be improved involving additional input information related to vehicle's route. For instance, a further study could include features obtained by vision system or other sensors for obstacle detection or route parameters definition (e.g. traffic lights, traffic congestion) methodologies.

Finally, V2G simulator present several feasible development prospects in order to improve modeling scenario reliability. Firstly, a differentiation between weekdays and weekends should be introduced in simulation. Then, a vehicle model describing powertrain and engine modules

can be included to properly simulate battery operating condition and relative consumption, thus affecting the description of both charge/discharge rate and aging dynamics. EV batteries can be statistically initialised at different SOH level in order to simulate a more realistic scenario. Moreover, geographic information system (GIS) data integration could improve charge and discharging modeling profiles ensuring a more realistic simulation.

Bibliography

[1] Climate Consulting Selectra. *Why Are Energy Prices Going Up?- What Can I Do?*, https://climate.selectra.com/en/news/energy-prices-going-up, 25th January 2022 [Online].

[2] European Commission. *Energy poverty*, https://energy.ec.europa.eu/topics/markets-and-consumers/energy-consumer-rights/energy-poverty_en, European Commission Directorate-General for Energy [Online].

[3] European Cooperation in Science Technology. *80 million European households struggle to stay warm. Rising energy costs will make the problem worse*, https://www.cost.eu/80-million-european-households-struggle-to-stay-warm-rising-energy-costs-will-make-the-p COST, 12 November 2021 [Online].

[4] Internation Energy Agency. *World Energy Outlook 2021*, https://www.iea.org/reports/world-energy-outlook-2021, World Energy Outlook 2021, IEA, Paris.

[5] Organization of the Petroleum Exporting Countries. *World Oil Outlook 2040*, https://www.energy-tomorrow.eu/wp-content/uploads/sites/15/2019/11/world-oil-outlook_executive-summary_2019.pdf,OPEC,26thOctober2019.

[6] State of the Energy Union 2021. *Renewables overtake fossil fuels as the EU's main power source*, https://ec.europa.eu/commission/presscorner/detail/en/IP_21_5554, EU Commission, 26th October 2021.

[7] K.M. Tan, T.S. Babu, V.K.Ramachandaramurthy, P. Kasinathan, S.G. Solanki, and S.K. Raveendran. Empowering smart grid: A comprehensive review of energy storage technology and application with renewable energy integration. *Journal of Energy Storage*, 39:102591, 2021.

[8] M.A. Taghikhani. Renewable resources and storage systems stochastic multi-objective optimal energy scheduling considering load and generation uncertainties. *Journal of Energy Storage*, 43:103293, 2021.

[9] Sam Aflaki and Serguei Netessine. Strategic investment in renewable energy sources: The effect of supply intermittency. *Manufacturing & Service Operations Management*, 19(3):489–507, 2017.

[10] S. A. Bozorgavari, J. Aghaei, S. Pirouzi, V. Vahidinasab, H. Farahmand, and M. Korpås. Two-stage hybrid stochastic/robust optimal coordination of distributed battery storage planning and flexible energy management in smart distribution network. *Journal of Energy Storage*, 26:100970, 2019.

[11] M. De Rosa, O. Afanaseva, A.V. Fedyukhin, and V. Bianco. Prospects and characteristics of thermal and electrochemical energy storage systems. *Journal of Energy Storage*, 44(Part B):103443, 2021.

[12] C.K. Das, T.S. Mahmoud, O. Bass, S.M. Muyeen, G. Kothapalli, A. Baniasadi, and N. Mousavi. Optimal sizing of a utility-scale energy storage system in transmission networks to improve frequency response. *Journal of Energy Storage*, 29:101315, 2020.

[13] A. Ramos, M. Tuovinen, and M. Ala-Juusela. Battery energy storage system (bess) as a service in finland: Business model and regulatory challenges. *Journal of Energy Storage*, 40:102720, 2021.

[14] W.S. Wan Abdullah, M. Osman, M.Z. Abidin Ab Kadir, R. Verayiah, N.F. Ab Aziz, and M. Abdul Rasheed. Techno-economics analysis of battery energy storage system (bess) design for virtual power plant (vpp)a case study in malaysia. *Journal of Energy Storage*, 38:102568, 2021.

[15] P. Saini and L. Gidwani. An investigation for battery energy storage system installation with renewable energy resources in distribution system by considering residential, commercial and industrial load models. *Journal of Energy Storage*, 45:103493, 2022.

[16] M.B. Mustafa, P. Keatley, Y. Huang, O. Agbonaye, O.O. Ademulegun, and N. Hewitt. Evaluation of a battery energy storage system in hospitals for arbitrage and ancillary services. *Journal of Energy Storage*, 43:103183, 2021.

[17] Clean Energy Institute. *Li-ion batteries*, `https://www.cei.washington.edu/education/science-of-solar/battery-technology/` [Online].

[18] Andrea Bartolini, Francesco Carducci, Carlos Boigues Muñoz, and Gabriele Comodi. Energy storage and multi energy systems in local energy communities with high renewable energy penetration. *Renewable Energy*, 159:595–609, 2020.

[19] Md Mustafizur Rahman, Abayomi Olufemi Oni, Eskinder Gemechu, and Amit Kumar. Assessment of energy storage technologies: A review. *Energy Conversion and Management*, 223:113295, 2020.

[20] Wei He, Marcus King, Xing Luo, Mark Dooner, Dacheng Li, and Jihong Wang. Technologies and economics of electric energy storages in power systems: Review and perspective. *Advances in Applied Energy*, 4:100060, 2021.

[21] Omid Palizban and Kimmo Kauhaniemi. Energy storage systems in modern gridsmatrix of technologies and applications. *Journal of Energy Storage*, 6:248–259, 2016.

[22] Jorge Vazquez-Arenas, Leonardo E. Gimenez, Michael Fowler, Taeyoung Han, and Shih ken Chen. A rapid estimation and sensitivity analysis of parameters describing the behavior of commercial li-ion batteries including thermal analysis. *Energy Conversion and Management*, 87:472–482, 2014.

[23] D Andre, M Meiler, K Steiner, H Walz, T Soczka-Guth, and DU Sauer. Characterization of high-power lithium-ion batteries by electrochemical impedance spectroscopy. ii: Modelling. *Journal of Power Sources*, 196(12):5349–5356, 2011.

[24] L.H. Saw, K. Somasundaram, Y. Ye, and A.A.O. Tay. Electro-thermal analysis of lithium iron phosphate battery for electric vehicles. *Journal of Power Sources*, 249:231–238, 2014.

[25] Aden Seaman, Thanh-Son Dao, and John McPhee. A survey of mathematics-based equivalent-circuit and electrochemical battery models for hybrid and electric vehicle simulation. *Journal of Power Sources*, 256:410–423, 2014.

[26] M. Barbieri, M. Ceraolo, G. Lutzemberger, C. Scarpelli, T. Pesso, and M. Giovannucci. Simplified electro-thermal model for lithium cells based on experimental tests. In *2020 AEIT International Conference of Electrical and Electronic Technologies for Automotive (AEIT AUTOMOTIVE)*, pages 1–6, 2020.

[27] Ahmed Zayed AL Shaqsi, Kamaruzzaman Sopian, and Amer Al-Hinai. Review of energy storage services, applications, limitations, and benefits. *Energy Reports*, 6:288–306, 2020. SI:Energy Storage - driving towards a clean energy future.

[28] Ivalin Petkov and Paolo Gabrielli. Power-to-hydrogen as seasonal energy storage: an uncertainty analysis for optimal design of low-carbon multi-energy systems. *Applied Energy*, 274:115197, 2020.

[29] A.H. Zimmerman. Self-discharge losses in lithium-ion cells. *IEEE Aerospace and Electronic Systems Magazine*, 19(2):19–24, 2004.

[30] S. Atalay, M. Sheikh, A. Mariani, Y. Merla, E. Bower, and W. Dhammika Widanage. Theory of battery ageing in a lithium-ion battery: Capacity fade, nonlinear ageing and lifetime prediction. *Journal of Power Sources*, 478:229026, 2020.

[31] Nina Meddings, Marco Heinrich, Frédéric Overney, Jong-Sook Lee, Vanesa Ruiz, Emilio Napolitano, Steffen Seitz, Gareth Hinds, Rinaldo Raccichini, Miran Gaberšček, et al. Application of electrochemical impedance spectroscopy to commercial li-ion cells: A review. *Journal of Power Sources*, 480:228742, 2020.

[32] Eduardo Redondo-Iglesias, Pascal Venet, and Serge Pelissier. Measuring reversible and irreversible capacity losses on lithium-ion batteries. In *2016 IEEE Vehicle Power and Propulsion Conference (VPPC)*, pages 1–5. IEEE, 2016.

[33] M. Jafari, K. Khan, and L. Gauchia. Deterministic models of li-ion battery aging: It is a matter of scale. *Journal of Energy Storage*, 20:67–77, 2018.

[34] ML.C. Casals, B.A. Garcia, F. Aguesse, and A. Iturrondobeitia. Second life of electric vehicle batteries: relation between materials degradation and environmental impact. *The International Journal of Life Cycle Assessment*, 22:82–97, 2017.

[35] G. Rizzoni, L. Guzzella, and B. M. Baumann. Unified modeling of hybrid electric vehicle drivetrains. *IEEE/ASME Transactions on Mechatronics*, 4(3):246–257, 1999.

[36] Lorenzo Serrao, Simona Onori, and Giorgio Rizzoni. Ecms as a realization of pontryagin's minimum principle for hev control. In *2009 American control conference*, pages 3964–3969. IEEE, 2009.

[37] Stefano Di Cairano, Daniele Bernardini, Alberto Bemporad, and Ilya V Kolmanovsky. Stochastic mpc with learning for driver-predictive vehicle control and its application to hev energy management. *IEEE Transactions on Control Systems Technology*, 22(3):1018–1031, 2013.

[38] Luca Cavanini, Pawel Majecki, Mike J Grimble, Hiroshi Uchihori, Mitsuhiko Tasaki, and Ikuo Yamamoto. LPV-MPC path planner for autonomous underwater vehicles. *IFAC-PapersOnLine*, 54(16):301–306, 2021.

[39] Hiroshi Uchihori, Luca Cavanini, Mitsuhiko Tasaki, Pawel Majecki, Yusuke Yashiro, Michael J Grimble, Ikuo Yamamoto, Gerrit M van der Molen, Akihiro Morinaga, and Kazuki Eguchi. Linear parameter-varying model predictive control of auv for docking scenarios. *Applied Sciences*, 11(10):4368, 2021.

[40] Luca Cavanini, Gianluca Ippoliti, and Eduardo F Camacho. Model predictive control for a linear parameter varying model of an uav. *Journal of Intelligent & Robotic Systems*, 101(3):1–18, 2021.

[41] Luca Cavanini, Pawel Majecki, Mike J Grimble, Vladimir Ivanovic, and H Eric Tseng. LPV-MPC path planning for autonomous vehicles in road junction scenarios. In *2021 IEEE International Intelligent Transportation Systems Conference (ITSC)*, pages 386–393. IEEE, 2021.

[42] Lucio Ciabattoni, Gabriele Comodi, Francesco Ferracuti, and Gabriele Foresi. Ai-powered home electrical appliances as enabler of demand-side flexibility. *IEEE Consumer Electronics Magazine*, 9(3):72–78, 2020.

[43] European Smart Grid Task Force. *Final Report: Demand Side Flexibility, Perceived Barriers and Proposed Recommendations*, EU Commission, April 2019.

[44] Internation Energy Agency. *Global ev outlook 2019: Scaling up the transition to electric mobility*, `https://www.iea.org/reports/global-ev-outlook-2019`, Global EV Outlook 2019, IEA, Paris.

[45] Kang Miao Tan, Vigna K Ramachandaramurthy, and Jia Ying Yong. Integration of electric vehicles in smart grid: A review on vehicle to grid technologies and optimization techniques. *Renewable and Sustainable Energy Reviews*, 53:720–732, 2016.

[46] Jesús Rodríguez-Molina, Pedro Castillejo, Victoria Beltran, and Margarita Martínez-Núñez. A model for cost–benefit analysis of privately owned vehicle-to-grid solutions. *Energies*, 13(21):5814, 2020.

[47] Marialaura Di Somma, Lucio Ciabattoni, Gabriele Comodi, and Giorgio Graditi. Managing plug-in electric vehicles in eco-environmental operation optimization of local multi-energy systems. *Sustainable Energy, Grids and Networks*, 23:100376, 2020.

[48] Timo Kern, Patrick Dossow, and Serafin von Roon. Integrating bidirectionally chargeable electric vehicles into the electricity markets. *Energies*, 13(21):5812, 2020.

[49] Asaad Mohammad, Ramon Zamora, and Tek Tjing Lie. Integration of electric vehicles in the distribution network: A review of pv based electric vehicle modelling. *Energies*, 13(17):4541, 2020.

[50] Jin Zhang, Liang Che, Lei Wang, and Udaya K Madawala. Game-theory based v2g coordination strategy for providing ramping flexibility in power systems. *Energies*, 13(19):5008, 2020.

[51] Zachary P Cano, Dustin Banham, Siyu Ye, Andreas Hintennach, Jun Lu, Michael Fowler, and Zhongwei Chen. Batteries and fuel cells for emerging electric vehicle markets. *Nature Energy*, 3(4):279–289, 2018.

[52] Hongcai Zhang, Zechun Hu, Zhiwei Xu, and Yonghua Song. Evaluation of achievable vehicle-to-grid capacity using aggregate pev model. *IEEE Transactions on Power Systems*, 32(1):784–794, 2016.

[53] Jens Groot. *State-of-health estimation of li-ion batteries: Cycle life test methods*. Chalmers Tekniska Hogskola (Sweden), 2012.

[54] Amit Mishra, Akansha Mehta, Soumen Basu, Shweta J Malode, Nagaraj P Shetti, Shyam S Shukla, Mallikarjuna N Nadagouda, and Tejraj M Aminabhavi. Electrode materials for lithium-ion batteries. *Materials Science for Energy Technologies*, 1(2):182–187, 2018.

[55] Nourhan Mohamed and Nageh K Allam. Recent advances in the design of cathode materials for li-ion batteries. *RSC Advances*, 10(37):21662–21685, 2020.

[56] Arumugam Manthiram, Xingwen Yu, and Shaofei Wang. Lithium battery chemistries enabled by solid-state electrolytes. *Nature Reviews Materials*, 2(4):1–16, 2017.

[57] Cheng Lin, Aihua Tang, Hao Mu, Wenwei Wang, and Chun Wang. Aging mechanisms of electrode materials in lithium-ion batteries for electric vehicles. *Journal of Chemistry*, 2015, 2015.

[58] M. Ecker, N. Nieto, S. Käbitz, J. Schmalstieg, H. Blanke, A. Warnecke, and D. UweSauer. Calendar and cycle life study of li(nimnco)o2-based 18650 lithium-ion batteries. *Journal of Power Sources*, 248:839–851, 2014.

[59] S.F.Schuster, T. Bach, E. Fleder, J. Müller, M. Brand, G. Sextl, and A.Jossen. Nonlinear aging characteristics of lithium-ion cells under different operational conditions. *Journal of Energy Storage*, 1:44–53, 2015.

[60] Christoph R Birkl, Matthew R Roberts, Euan McTurk, Peter G Bruce, and David A Howey. Degradation diagnostics for lithium ion cells. *Journal of Power Sources*, 341:373–386, 2017.

[61] Mehdi Jafari, Khalid Khan, and Lucia Gauchia. Deterministic models of li-ion battery aging: It is a matter of scale. *Journal of Energy Storage*, 20:67–77, 2018.

[62] Noshin Omar, Yousef Firouz, H Gualous, Justin Salminen, T Kallio, JM Timmermans, Th Coosemans, P Van den Bossche, and J Van Mierlo. Aging and degradation of lithium-ion batteries. In *Rechargeable Lithium Batteries*, pages 263–279. Elsevier, 2015.

[63] Noshin Omar, Mohamed Abdel Monem, Yousef Firouz, Justin Salminen, Jelle Smekens, Omar Hegazy, Hamid Gaulous, Grietus Mulder, Peter Van den Bossche, Thierry Coosemans, et al. Lithium iron phosphate based battery–assessment of the aging parameters and development of cycle life model. *Applied Energy*, 113:1575–1585, 2014.

[64] John Wang, Ping Liu, Jocelyn Hicks-Garner, Elena Sherman, Souren Soukiazian, Mark Verbrugge, Harshad Tataria, James Musser, and Peter Finamore. Cycle-life model for graphite-lifepo4 cells. *Journal of power sources*, 196(8):3942–3948, 2011.

[65] Michel Broussely, Ph Biensan, F Bonhomme, Ph Blanchard, S Herreyre, K Nechev, and RJ Staniewicz. Main aging mechanisms in li ion batteries. *Journal of power sources*, 146(1-2):90–96, 2005.

[66] Andrzej Łebkowski. Temperature, overcharge and short-circuit studies of batteries used in electric vehicles. *Przegląd Elektrotechniczny*, 1(5):69–75, 2017.

[67] Yun Bao, Wenbin Dong, and Dian Wang. Online internal resistance measurement application in lithium ion battery capacity and state of charge estimation. *Energies*, 11(5):1073, 2018.

[68] Shuai Ma, Modi Jiang, Peng Tao, Chengyi Song, Jianbo Wu, Jun Wang, Tao Deng, and Wen Shang. Temperature effect and thermal impact in lithium-ion batteries: A review. *Progress in Natural Science: Materials International*, 28(6):653–666, 2018.

[69] MikroElektronika. *Li-Polymer battery datasheet*, `https://www.batteryspace.com/prod-specs/3.7V9059156.pdf`, SR674361P, 2013 [Online].

[70] Seongjun Lee, Jonghoon Kim, Jaemoon Lee, and Bo H Cho. State-of-charge and capacity estimation of lithium-ion battery using a new open-circuit voltage versus state-of-charge. *Journal of power sources*, 185(2):1367–1373, 2008.

[71] Mark Verbrugge and Edward Tate. Adaptive state of charge algorithm for nickel metal hydride batteries including hysteresis phenomena. *Journal of Power Sources*, 126(1-2):236–249, 2004.

[72] Mark Verbrugge. Adaptive, multi-parameter battery state estimator with optimized time-weighting factors. *Journal of applied electrochemistry*, 37(5):605–616, 2007.

[73] Frédéric Claude, Mohamed Becherif, and HS Ramadan. Experimental validation for li-ion battery modeling using extended kalman filters. *International Journal of Hydrogen Energy*, 42(40):25509–25517, 2017.

[74] Muhammad U Tahir, Muhammad Anees, Hassan A Khan, Irfan Khan, Nauman Zaffar, and Taha Moaz. Modeling and evaluation of nickel manganese cobalt based li-ion storage for stationary applications. *Journal of Energy Storage*, 36:102346, 2021.

[75] Giuliano Rancilio, Alexandre Lucas, Evangelos Kotsakis, Gianluca Fulli, Marco Merlo, Maurizio Delfanti, and Marcelo Masera. Modeling a large-scale battery energy storage system for power grid application analysis. *Energies*, 12(17), 2019.

[76] Olivier Tremblay and Louis-A. Dessaint. Experimental validation of a battery dynamic model for ev applications. *World Electric Vehicle Journal*, 3(2):289–298, 2009.

[77] Tarun Huria, Massimo Ceraolo, Javier Gazzarri, and Robyn Jackey. High fidelity electrical model with thermal dependence for characterization and simulation of high power lithium battery cells. In *2012 IEEE International Electric Vehicle Conference*, pages 1–8, 2012.

[78] Jorge Varela Barreras, Erik Schaltz, Søren Juhl Andreasen, and Tomasz Minko. Datasheet-based modeling of li-ion batteries. In *2012 IEEE Vehicle Power and Propulsion Conference*, pages 830–835, 2012.

[79] Clemens Guenther, Benjamin Schott, Wilfried Hennings, Paul Waldowski, and Michael A. Danzer. Model-based investigation of electric vehicle battery aging by means ofăvehicle-to-grid scenario simulations. *Journal of Power Sources*, 239:604–610, 2013.

[80] Scott J. Moura, Nalin A. Chaturvedi, and Miroslav Krsti. Adaptive Partial Differential Equation Observer for Battery State-of-Charge/State-of-Health Estimation Via an Electrochemical Model. *Journal of Dynamic Systems, Measurement, and Control*, 136(1), 10 2013. 011015.

[81] N. Omar, Y. Firouz, H. Gualous, J. Salminen, T. Kallio, J.M. Timmermans, Th. Coosemans, P. Van den Bossche, and J. Van Mierlo. 9 - aging and degradation of lithium-ion batteries. In Alejandro A. Franco, editor, *Rechargeable Lithium Batteries*, Woodhead Publishing Series in Energy, pages 263–279. Woodhead Publishing, 2015.

[82] Alexander Farmann, Wladislaw Waag, Andrea Marongiu, and Dirk Uwe Sauer. Critical review of on-board capacity estimation techniques for lithium-ion batteries in electric and hybrid electric vehicles. *Journal of Power Sources*, 281:114–130, 2015.

[83] M. Berecibar, I. Gandiaga, I. Villarreal, N. Omar, J. Van Mierlo, and P. Van den Bossche. Critical review of state of health estimation methods of li-ion batteries for real applications. *Renewable and Sustainable Energy Reviews*, 56:572–587, 2016.

[84] Simone Barcellona and Luigi Piegari. Lithium ion battery models and parameter identification techniques. *Energies*, 10(12), 2017.

[85] Daniel-Ioan Stroe, Maciej Swierczynski, Søren Knudsen Kær, and Remus Teodorescu. Degradation behavior of lithium-ion batteries during calendar ageingthe case of the internal resistance increase. *IEEE Transactions on Industry Applications*, 54(1):517–525, 2018.

[86] Tugce Yuksel, Shawn Litster, Venkatasubramanian Viswanathan, and Jeremy J. Michalek. Plug-in hybrid electric vehicle lifepo4 battery life implications of thermal management, driving conditions, and regional climate. *Journal of Power Sources*, 338:49–64, 2017.

[87] Shuangqi Li, Hongwen He, Chang Su, and Pengfei Zhao. Data driven battery modeling and management method with aging phenomenon considered. *Applied Energy*, 275:115340, 2020.

[88] E. Sarasketa-Zabala, E. Martinez-Laserna, M. Berecibar, I. Gandiaga, L.M. Rodriguez-Martinez, and I. Villarreal. Realistic lifetime prediction approach for li-ion batteries. *Applied Energy*, 162:839–852, 2016.

[89] Issam Baghdadi, Olivier Briat, Jean-Yves Delétage, Philippe Gyan, and Jean-Michel Vinassa. Lithium battery aging model based on dakins degradation approach. *Journal of Power Sources*, 325:273–285, 2016.

[90] Nina Harting, René Schenkendorf, Nicolas Wolff, and Ulrike Krewer. State-of-health identification of lithium-ion batteries based on nonlinear frequency response analysis: First steps with machine learning. *Applied Sciences*, 8(5), 2018.

[91] Haihong Pan, Zhiqiang Lü, Huimin Wang, Haiyan Wei, and Lin Chen. Novel battery state-of-health online estimation method using multiple health indicators and an extreme learning machine. *Energy*, 160:466–477, 2018.

[92] Linlin Fang, Junqiu Li, and Bo Peng. Online estimation and error analysis of both soc and soh of lithium-ion battery based on dekf method. *Energy Procedia*, 158:3008–3013, 2019.

[93] Dave Andre, Christian Appel, Thomas Soczka-Guth, and Dirk Uwe Sauer. Advanced mathematical methods of soc and soh estimation for lithium-ion batteries. *Journal of power sources*, 224:20–27, 2013.

[94] Sahar Khaleghi, Yousef Firouz, Maitane Berecibar, Joeri Van Mierlo, and Peter Van Den Bossche. Ensemble gradient boosted tree for soh estimation based on diagnostic features. *Energies*, 13(5), 2020.

[95] Jinhao Meng, Lei Cai, Daniel-Ioan Stroe, Junpeng Ma, Guangzhao Luo, and Remus Teodorescu. An optimized ensemble learning framework for lithium-ion battery state of health estimation in energy storage system. *Energy*, 206:118140, 2020.

[96] Shuxiang Song, Chen Fei, and Haiying Xia. Lithium-ion battery soh estimation based on xgboost algorithm with accuracy correction. *Energies*, 13(4):812, 2020.

[97] Carlos Vidal, Pawel Malysz, Phillip Kollmeyer, and Ali Emadi. Machine learning applied to electrified vehicle battery state of charge and state of health estimation: State-of-the-art. *IEEE Access*, 8:52796–52814, 2020.

[98] Marco Ragone, Vitaliy Yurkiv, Ajaykrishna Ramasubramanian, Babak Kashir, and Farzad Mashayek. Data driven estimation of electric vehicle battery state-of-charge informed by automotive simulations and multi-physics modeling. *Journal of Power Sources*, 483:229108, 2021.

[99] Nagi Gebraeel. Sensory-updated residual life distributions for components with exponential degradation patterns. *IEEE Transactions on Automation Science and Engineering*, 3(4):382–393, 2006.

[100] Jia Guo, Yaqi Li, Kjeld Pedersen, and Daniel-Ioan Stroe. Lithium-ion battery operation, degradation, and aging mechanism in electric vehicles: An overview. *Energies*, 14(17):5220, 2021.

[101] Riccardo Poli, James Kennedy, and Tim Blackwell. Particle swarm optimization. *Swarm intelligence*, 1(1):33–57, 2007.

[102] Det Norske Veritas group. *New Storage Capacity: Key Element for the Energy Transition in Italy* , `https://www.dnv.com/article/new-storage-capacity-key-element-for-the-energy-transition-in-italy-186083`, DNV [Online].

[103] Tomohiro Takagi and Michio Sugeno. Fuzzy identification of systems and its applications to modeling and control. *IEEE transactions on systems, man, and cybernetics*, (1):116–132, 1985.

[104] Prashant Shrivastava, Tey Kok Soon, Mohd Yamani Idna Bin Idris, and Saad Mekhilef. Overview of model-based online state-of-charge estimation using kalman filter family for lithium-ion batteries. *Renewable and Sustainable Energy Reviews*, 113:109233, 2019.

[105] Donald J Berndt and James Clifford. Using dynamic time warping to find patterns in time series. In *KDD workshop*, volume 10, pages 359–370. Seattle, WA, USA:, 1994.

[106] Zheng Chen, Chao Yang, and Shengnan Fang. A convolutional neural network-based driving cycle prediction method for plug-in hybrid electric vehicles with bus route. *IEEE Access*, 8:3255–3264, 2019.

[107] Limin Niu et al. Intelligent HEV fuzzy logic control strategy based on identification and prediction of drive cycle and driving trend. *World Journal of Engineering and Technology*, 3(03):215, 2015.

[108] Xinyou Lin, Guangji Zhang, and Shenshen Wei. Velocity prediction using Markov Chain combined with driving pattern recognition and applied to Dual-Motor Electric Vehicle energy consumption evaluation. *Applied Soft Computing*, 101:106998, 2021.

[109] Shuwei Zhang, Donghao Zhang, Yugong Luo, Junmin Wang, and Keqiang Li. Predictive energy management strategy for electric vehicles based on estimation of preceding vehicle future movements. In *2016 IEEE international conference on advanced intelligent mechatronics (AIM)*, pages 1436–1441. IEEE, 2016.

[110] Yuecheng Li, Hongwen He, and Jiankun Peng. An adaptive online prediction method with variable prediction horizon for future driving cycle of the vehicle. *IEEE Access*, 6:33062–33075, 2018.

[111] LiPeng Zhang, Wei Liu, and BingNan Qi. Energy optimization of multi-mode coupling drive plug-in hybrid electric vehicles based on speed prediction. *Energy*, 206:118126, 2020.

[112] Chao Sun, Xiaosong Hu, Scott J Moura, and Fengchun Sun. Velocity predictors for predictive energy management in hybrid electric vehicles. *IEEE Transactions on Control Systems Technology*, 23(3):1197–1204, 2015.

[113] Amir Rezaei and Jeffrey B Burl. Prediction of vehicle velocity for model predictive control. *IFAC-PapersOnLine*, 48(15):257–262, 2015.

[114] Xun Shen and Tielong Shen. Neural-network-based vehicle torque demand forecasting. In *2017 17th International Conference on Control, Automation and Systems (ICCAS)*, pages 21–26. IEEE, 2017.

[115] Weiying Zeng, Mohammed AS Khalid, Xiaoye Han, and Jimi Tjong. A study on extreme learning machine for gasoline engine torque prediction. *IEEE Access*, 8:104762–104774, 2020.

[116] Dehua Shi, Shaohua Wang, Yingfeng Cai, and Long Chen. Stochastic predictive energy management of power split hybrid electric bus for real-world driving cycles. *IEEE Access*, 6:61700–61713, 2018.

[117] Yulong Zhao, Wenjun Chen, Weida Wang, Changle Xiang, and Kun Huang. Research on optimal power allocation strategy based on power demand prediction for electro-mechanical transmission. In *2016 35th Chinese Control Conference (CCC)*, pages 8638–8643. IEEE, 2016.

[118] Weihang Meng, Jiangyan Zhang, and Rubo Zhang. A real-time prediction algorithm for driver torque demand based on vehicle-vehicle communication. In *2019 Chinese Automation Congress (CAC)*, pages 3435–3440. IEEE, 2019.

[119] Arpita Bhattacharjee, S Saranya, and Purushottam Kuntumalla. Estimation of driver demand torque using parametric and nonparametric data-driven model. In *2021 IEEE Second International Conference on Control, Measurement and Instrumentation (CMI)*, pages 87–92. IEEE, 2021.

[120] Chi-Man Vong, Pak-Kin Wong, and Yi-Ping Li. Prediction of automotive engine power and torque using least squares support vector machines and bayesian inference. *Engineering Applications of Artificial Intelligence*, 19(3):277–287, 2006.

[121] Luca Cavanini, Francesco Ferracuti, Sauro Longhi, and Andrea Monteriù. Ls-svm for lpv-arx identification: Efficient online update by low-rank matrix approximation. In *2020 International conference on unmanned aircraft systems (ICUAS)*, pages 1590–1595. IEEE, 2020.

[122] Luca Cavanini, Francesco Ferracuti, Sauro Longhi, Enrico Marchegiani, and Andrea Monteriù. Sparse approximation of ls-svm for lpv-arx model identification: Application to a powertrain subsystem. In *2020 AEIT International Conference of Electrical and Electronic Technologies for Automotive (AEIT AUTOMOTIVE)*, pages 1–6. IEEE, 2020.

[123] Nguyen Hoang An and Duong Tuan Anh. Comparison of Strategies for Multi-step-Ahead Prediction of Time Series Using Neural Network. In *2015 International Conference on Advanced Computing and Applications (ACOMP)*, pages 142–149, 2015.

[124] Xiao-Li Meng and Donald B Rubin. Maximum likelihood estimation via the ECM algorithm: A general framework. *Biometrika*, 80(2):267–278, 1993.

[125] Lennart Ljung, Carl Andersson, Koen Tiels, and Thomas B Schön. Deep learning and system identification. *IFAC-PapersOnLine*, 53(2):1175–1181, 2020.

[126] Johan Schoukens, Mark Vaes, and Rik Pintelon. Linear system identification in a nonlinear setting: Nonparametric analysis of the nonlinear distortions and their impact on the best linear approximation. *IEEE Control Systems Magazine*, 36(3):38–69, 2016.

[127] Johan Schoukens and Lennart Ljung. Nonlinear system identification: A user-oriented road map. *IEEE Control Systems Magazine*, 39(6):28–99, 2019.

[128] Seong Hyeon Park, ByeongDo Kim, Chang Mook Kang, Chung Choo Chung, and Jun Won Choi. Sequence-to-sequence prediction of vehicle trajectory via lstm encoder-decoder architecture. In *2018 IEEE Intelligent Vehicles Symposium (IV)*, pages 1672–1678, 2018.

[129] J.A.K. Suykens, T. Van Gestel, J. De Brabanter, B. De Moor, and J. Vandewalle. *Least Squares Support Vector Machines*. World Scientific, 2002.

[130] K. De Brabanter, Ph. Dreesen, P. Karsmakers, K. Pelckmans, J. De Brabanter, J.A.K. Suykens, and B. De Moor. Fixed-size ls-svm applied to the wiener-hammerstein benchmark. *IFAC Proceedings Volumes*, 42(10):826–831, 2009. 15th IFAC Symposium on System Identification.

[131] Christopher Williams and Matthias Seeger. Using the nyström method to speed up kernel machines. In *Advances in Neural Information Processing Systems 13*, pages 682–688. MIT Press, 2001.

[132] Islam El-Nabarawy, Ashraf M Abdelbar, and Donald C Wunsch. Levenberg-marquardt and conjugate gradient methods applied to a high-order neural network. In *The 2013 International joint conference on neural networks (IJCNN)*, pages 1–7. IEEE, 2013.

[133] He-Sheng Tang, Song-Tao Xue, Rong Chen, and Tadanobu Sato. Online weighted LS-SVM for hysteretic structural system identification. *Engineering Structures*, 28(12):1728–1735, 2006.

[134] Pak-kin Wong, Chi-man Vong, and Weng-fai Ip. Modelling of Petrol Engine Power Using Incremental Least-Square Support Vector Machines for ECU Calibration. In *2010 International Conference on Optoelectronics and Image Processing*, volume 2, pages 12–15, 2010.

[135] Pak Kin Wong, Hang Cheong Wong, Chi Man Vong, and Ka In Wong. Online wavelet least-squares support vector machine fuzzy predictive control for engine lambda regulation. *International Journal of Engine Research*, 17(8):866–885, 2016.

[136] Zhifeng Hao, Shu Yu, Xiaowei Yang, Feng Zhao, Rong Hu, and Yanchun Liang. Online LS-SVM learning for classification problems based on incremental chunk. In *International Symposium on Neural Networks*, pages 558–564. Springer, 2004.

[137] Lars Johannesson, Nikolce Murgovski, Soren Ebbesen, Bo Egardt, Esteban Gelso, and Jonas Hellgren. Including a battery state of health model in the hev component sizing and optimal control problem. *IFAC Proceedings Volumes*, 46(21):398–403, 2013.

[138] Soren Ebbesen, Philipp Elbert, and Lino Guzzella. Battery state-of-health perceptive energy management for hybrid electric vehicles. *IEEE Transactions on Vehicular technology*, 61(7):2893–2900, 2012.

[139] Stamatis Karnouskos and Thiago Nass De Holanda. Simulation of a smart grid city with software agents. In *2009 Third UKSim European Symposium on Computer Modeling and Simulation*, pages 424–429. IEEE, 2009.

[140] Jayakrishnan R Pillai and Birgitte Bak-Jensen. Impacts of electric vehicle loads on power distribution systems. In *2010 IEEE Vehicle Power and Propulsion Conference*, pages 1–6. IEEE, 2010.

[141] Cui Shumei, Liu Xiaofei, Tian Dewen, Zhang Qianfan, and Song Liwei. The construction and simulation of v2g system in micro-grid. In *2011 International Conference on Electrical Machines and Systems*, pages 1–4. IEEE, 2011.

[142] Arnaldo Arancibia and Kai Strunz. Modeling of an electric vehicle charging station for fast dc charging. In *2012 IEEE International Electric Vehicle Conference*, pages 1–6. IEEE, 2012.

[143] Goncalo Cardoso, Michael Stadler, Mohammed C Bozchalui, Ratnesh Sharma, Chris Marnay, Ana Barbosa-Póvoa, and Paulo Ferrão. Optimal investment and scheduling of distributed energy resources with uncertainty in electric vehicle driving schedules. *Energy*, 64:17–30, 2014.

[144] Tomislav Novosel, Luka Perković, Marko Ban, Hrvoje Keko, Tomislav Pukšec, Goran Krajačić, and Neven Duić. Agent based modelling and energy planning–utilization of matsim for transport energy demand modelling. *Energy*, 92:466–475, 2015.

[145] Luca Bedogni, Luciano Bononi, Marco Di Felice, Alfredo D'Elia, Randolf Mock, Francesco Morandi, Simone Rondelli, Tullio Salmon Cinotti, and Fabio Vergari. An integrated simulation framework to model electric vehicle operations and services. *IEEE Transactions on vehicular Technology*, 65(8):5900–5917, 2015.

[146] Susana Alegre, Juan V Míguez, and José Carpio. Modelling of electric and parallel-hybrid electric vehicle using matlab/simulink environment and planning of charging stations through a geographic information system and genetic algorithms. *Renewable and Sustainable Energy Reviews*, 74:1020–1027, 2017.

[147] Emmanouil S Rigas, Sotiris Karapostolakis, Nick Bassiliades, and Sarvapali D Ramchurn. Evlibsim: A tool for the simulation of electric vehicles charging stations using the evlib library. *Simulation Modelling Practice and Theory*, 87:99–119, 2018.

[148] Bruno Canizes, João Soares, Angelo Costa, Tiago Pinto, Fernando Lezama, Paulo Novais, and Zita Vale. Electric vehicles user charging behaviour simulator for a smart city. *Energies*, 12(8):1470, 2019.

[149] Michael A Roscher and Dirk Uwe Sauer. Dynamic electric behavior and open-circuit-voltage modeling of lifepo4-based lithium ion secondary batteries. *Journal of Power Sources*, 196(1):331–336, 2011.

[150] Christian Campestrini, Thomas Heil, Stephan Kosch, and Andreas Jossen. A comparative study and review of different kalman filters by applying an enhanced validation method. *Journal of Energy Storage*, 8:142–159, 2016.

[151] Haifeng Dai, Xuezhe Wei, and Zechang Sun. State and parameter estimation of a hev li-ion battery pack using adaptive kalman filter with a new soc-ocv concept. In *2009 International Conference on Measuring Technology and Mechatronics Automation*, volume 2, pages 375–380. IEEE, 2009.

[152] Haihong Pan, Zhiqiang Lü, Weilong Lin, Junzi Li, and Lin Chen. State of charge estimation of lithium-ion batteries using a grey extended kalman filter and a novel open-circuit voltage model. *Energy*, 138:764–775, 2017.